UNIVERSITEIT VAN PRETORIA
UNIVERSITY OF PRETORIA
YUNIBESITHI YA PRETORIA

Modelling and spectroscopic studies of 1-hydroxyethylidene-1,1-diphosphonic acid and its interaction with hydroxyapatite as a model of bone

by

Werner Barnard

Submitted in partial fulfilment of the requirements for the degree

Philosophiae Doctor

in the Faculty of Natural and Agricultural Sciences,
University of Pretoria

September 2009

Acknowledgements

I would like to thank the following people who have supported and assisted me during the completion of this degree:

- My supervisors, Prof. Ignacy Cukrowski and Prof. Petrus H van Rooyen for their guidance, input and support during this project.
- Prof. Sylvia O Paul, our collaborator at UNISA, for use and recording of Raman spectra on the spectrometer, as well as generating chemometric data.
- Dr Ljiljana Popović for the recording of certain Raman spectra and assistance with the analysis thereof.
- My parents, who dealt with moods, scoldings and tantrums, and who have been there through absolute brimstone and fire stuff, thank you.
- Sasol, the company that started my tertiary education, finished it and now have my training at their disposal for research.
- Daniela Bezuidenhout: what can I say – sounding board, agony aunt, verbal abuse taker, social support and everything else. See you in the publication lists!
- Marilé Landman for talks, chats, eats, drinks, another ear and being a collaborator. Truly a multi-tasking woman professionally and most important socially!
- Eric Palmer and Dave Liles, be it He, N_2, X-ray or stomach filling, lots has been discussed and many a life lesson learnt.
- Helga Nordhoff, my 'exposure' partner to scientific community engagement and novel photographic methods.
- My dearest friend Riaan du Plessis – one day we may yet both be citizens of the true First World.
- The Bruker Museum Appreciation Club members – you know who you are!

This whole thesis is dedicated to my grandmother,

Beatrix Jeanetta Rademeyer

1918 – 2009

"And crawling on the planet's face
Some insects called 'The Human Race'
Lost in time, lost in space
and meaning…"

from the musical,
The Rocky Horror Picture Show, 1976

Abstract

Modelling and spectroscopic studies of 1-hydroxyethylidene-1,1-diphosphonic acid and its interaction with hydroxyapatite as a model of bone

by

Werner Barnard

Supervisor: Prof. I. Cukrowski
Co-supervisor: Prof. P.H. van Rooyen

Submitted in partial fulfilment of the requirements for the degree Philosophiae Doctor
Department of Chemistry, University of Pretoria, Pretoria

The behaviour of 1-hydroxyethylidene-1,1-diphosphonic acid (HEDP, H_4L) was studied in the aqueous medium and at the hydroxyapatite interface as a model of bone. In solution, the pH-dependency of the various protonated forms of HEDP was studied using nuclear magnetic resonance (NMR) spectroscopy of various nuclei and from this comparable pK_a values could be obtained from the ^{31}P chemical shift curve. The Raman spectra of the aqueous samples were measured and each protonated form was identified by unique vibrational bands. Multivariate curve resolution analysis was used to redetermine the species distribution diagram, as well as pure component spectra of each protonated form. Molecular modelling was employed to determine the most probable conformer present in solution and also to calculate the theoretical vibrational spectrum of each conformer. Comparison of the theoretical and experimental data allowed the assignment of the different Raman bands observed. The species present at low pH were the most problematic to analyse due to the strong inter- and intramolecular hydrogen bonding indirectly observed in the data.

The interaction of HEDP at low and high concentrations with hydroxyapatite, bovine bone and $CaHPO_4$ was investigated *in situ* by means of Raman spectroscopy and it was found that two Ca-HEDP complexes are sequentially

formed at both concentrations, and that the order of formation of these two complexes can be explained from the species distribution diagrams of Ca-HEDP complexes. One complex, $CaHEDP{\cdot}2H_2O$, was successfully isolated and characterised by means of single-crystal X-ray Diffraction (XRD) methods and Raman spectroscopy. Theoretically generated Raman spectra were used to assist in the assignment of the solid-state Raman spectrum of $CaHEDP{\cdot}2H_2O$. It is postulated that the unknown complex is the monoprotonated Ca-HEDP complex. Using the Raman spectra of the complexes and HEDP as references, it was determined that HEDP(aq) interacts similarly with hydroxyapatite, bovine bone and $CaHPO_4$ and thus hydroxyapatite can be substituted for bone in the Raman spectroscopic study of HEDP with bone. HEDP interaction was also studied at pH values of 5.0 and 7.4 to understand the nature of the interaction at the pH values at which the diprotonated (H_2L^{2-}) form is predominantly present, as well as at the pH of human blood plasma, which is slightly basic.

HEDP exists as a monohydrate at room temperature and the single-crystal structure was redetermined, during which the hydrogen positions were experimentally obtained for the first time by means of X-ray diffraction methods. The anhydrous form of HEDP exists above 70 °C and Rietveld refinement of the powder X-ray pattern of anhydrous HEDP was used to solve its crystal structure. The complexity of contributory factors allowed only for the non-hydrogen atom positions to be determined. Fourier-transform infrared (FTIR) and Raman spectroscopy were performed on both phases and there is evidence in the Raman spectrum that hydrogen bonding still plays a predominant role in the anhydrous solid state.

All these studies led to a better understanding of the nature of bisphosphonate interaction with bone and the results can therefore be applied in future medical studies for drug screening regarding bone cancer research.

TABLE OF CONTENTS

List of Figures

List of Tables

List of Related Publication/Conference Outputs

Publications

1. "Modelling and spectroscopic studies of bisphosphonate-bone interactions. The Raman, NMR and crystallographic investigations of Ca-HEDP complexes" Cukrowski I, Popović L, Barnard W, Paul SO, Van Rooyen PH, Liles DC. *Bone*, **2007**, *41*, 668.

2. "The analysis of pH dependent protonated conformers of 1-hydroxyethylidene-1,1-diphosphonic acid by means of FT-Raman Spectroscopy, multivariate curve resolution and DFT modelling" Barnard W, Paul SO, Van Rooyen PH, Cukrowski I. *Journal of Raman Spectroscopy*, **2008**, ACCEPTED, DOI 10.1002/jrs.2343.

Oral Presentations

1. "A spectroscopic comparison of the anhydrous and monohydrate form of HEDP, a bone cancer pain palliation agent" *SACI Young Chemist Symposium – Gauteng Branch*, University of Johannesburg, 27 October 2006.

2. "The investigation of 1-hydroxyethylidene-1,1-diphosphonic acid and its complexes by Raman and NMR spectroscopy" W Barnard, L Popović, I Cukrowski, PH Van Rooyen, DC Liles and SO Paul, *SACI 2007 Inorganic Conference*, Langebaan, South Africa, 8–12 July 2007.

3. "Die bestudering van 1-hidroksietilideen-1,1-difosfoniese suur en sy komplekse met behulp van Raman en KMR Spektroskopie" *SAAWK Studente Simposium*, Tshwane University of Technology, 2 October 2007.

Poster Presentations

1. “The multivariate analysis and DFT study of various protonated HEDP conformers over the pH range 1.00–13.00” W Barnard, SO Paul, PH van Rooyen and I Cukrowski, *XXI International Conference on Raman Spectroscopy*, London, UK, 17–22 August 2008.

1 Introduction

Bisphosphonic acids are widely used in the pharmaceutical industry as drugs for degenerative bone disease or as ligand/chelating components thereof. It has been found that different functionalities in the bisphosphonate result in different potencies and this is a direct result of the conformational interaction of the bisphosphonate with the surface of the bone. The study focused on using various theoretical and spectroscopic methods to investigate the nature of the conformations in the aqueous medium, as well as at the bone mineral surface/liquid interface, for the reference bisphosphonate, 1-hydroxyethylidene-1,1-diphosphonic acid. This chapter provides an introduction to the system investigated, the techniques used to study the various conformers and bone mineral surface interaction.

1.1 Bisphosphonates

Bisphosphonates are compounds analogous to the naturally occurring pyrophosphate class of compounds and contain a P-C-P linkage, instead of a P-O-P linkage, as can be seen in Figure 1-1. The first use of bisphosphonates was mainly of an industrial nature and, most importantly, as 'water softeners' in domestic and industrial water systems due to their ability to inhibit the formation of insoluble calcium carbonate [1]. Pyrophosphates were determined to be calcification inhibitors [2] but efforts to utilise this property in the treatment of certain human conditions were unsuccessful due to pyrophosphates being hydrolysed under such physiological circumstances [1]. Attempts were made to find other compounds with similar inhibitory properties. Since bisphosphonates are resistant to hydrolysis and also have a high affinity for bone mineral, they proved to be the most successful alternative. These compounds were especially desirable because they were active when orally administered to rats [1, 3].

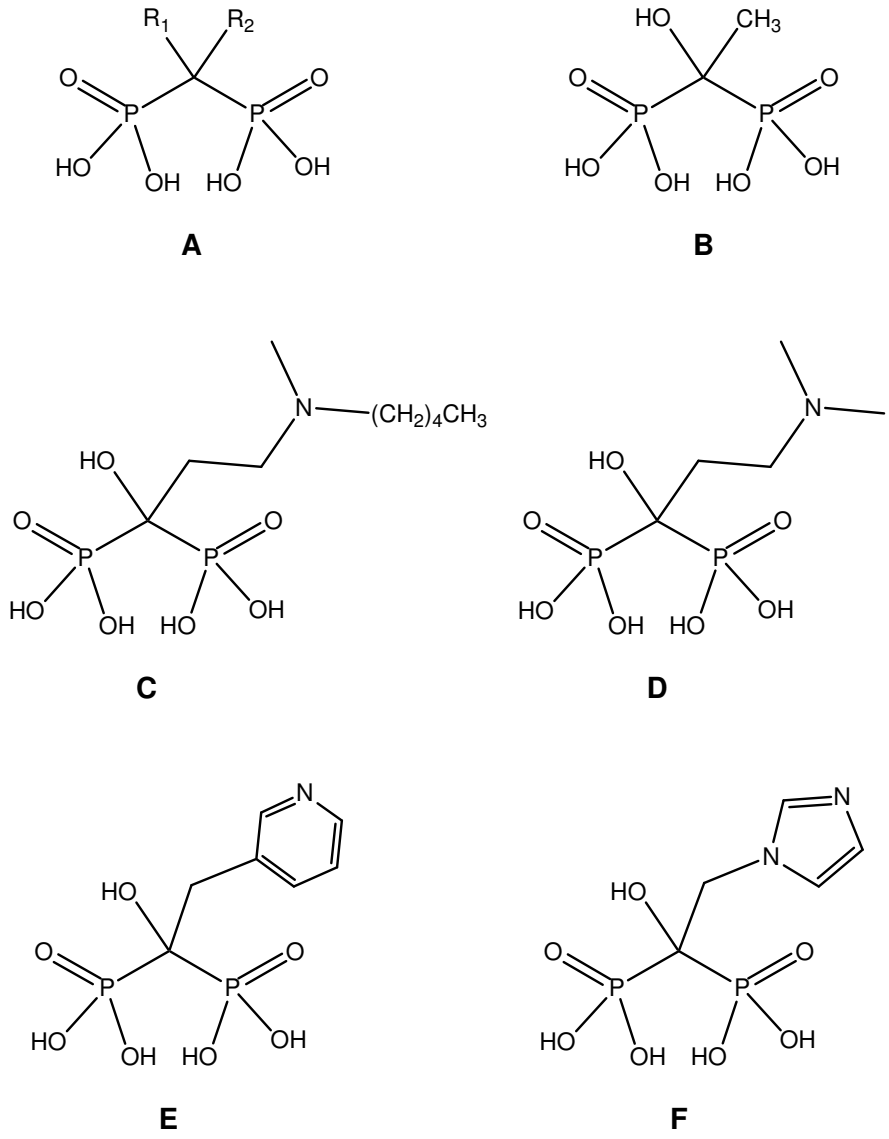

Figure 1-1. A. The generalised structure of the bisphosphonates and that of B. HEDP, C. ibandronic acid, D. olpadronic acid, E. risedronic acid and F. zoledronic acid

As the value of bisphosphonates with potential medical applications grew, the need to understand the relationships between structure and activity became more important, and various modifications to the bisphosphonate motif were investigated by varying the substituents R_1 and R_2 (Figure 1-1A). It was determined in early studies that the P-C-P moiety is integral to the high affinity of bisphosphonates for bone [1] and this high affinity was found to be significantly enhanced when R_1 = OH. The oldest, best known and benchmark bisphosphonate is 1-hydroxyethylidene-1,1-diphosphonic acid, in which R_1 = OH

and R_2 = CH_3 (Figure 1-1B). It is commonly abbreviated as HEDP and is commercially known as etidronic acid.

The high affinity of the bisphosphonates for bone mineral is not necessarily the only reason why they are potent antiresorption agents. Varying the R_2 side chain with R_1 = OH (Figure 1-1) showed that R_2 groups containing especially tertiary nitrogen atoms, such as ibandronic and olpadronic acid (Figures 1-1C and 1-1D), were much more potent than HEDP. The most potent of these groups were those in which the nitrogen was included in a heterocyclic ring, such as in risedronic and zoledronic acid (Figures 1-1E and 1-1F), being more than 10 000 times more potent than HEDP [1]. The presence of the two phosphonic acid groups is very important for the biological activity of the bisphosphonates and studies show that replacement of one or two of the phosphonic hydroxyl groups dramatically reduces both bone affinity and antiresorptivity in the molecule [1].

Thus, in summary, the presence of the two phosphonic groups as well as a hydroxyl group at R_1 is responsible for the high affinity for bone mineral and the targeting thereof. The antiresorptivity is mostly a function of the R_2 side chain and the three-dimensional conformation of the bisphosphonate at the bone mineral surface [1]. Comparisons of the activity of stereoisomers of certain bisphosphonates show a tenfold preference for one over the other, indicating the stereochemical preference of a possible receptor site [4]. This underlines the importance of understanding the structural aspects of these bisphosphonates on a more fundamental level, both that of the free molecule and that of the molecule at the bone mineral surface.

It would be meaningful, therefore, to begin such a study by focusing first on the benchmark bisphosphonate HEDP.

1.2 Radiopharmaceutical uses of bisphosphonates

The high affinity of bisphosphonates for bone mineral also suggests that these compounds should be ideal ligands for complexation with radionuclides for the

purpose of specifically targeting pain-palliative, imaging and chemotherapeutic treatments for bone cancer and its symptoms [1, 5, 6]. The radionuclide to be used should be a medium-energy β-emitter with prolonged, selective uptake and retention at the sites of infection [5]. Due to different radionuclides having different physiological behaviours in the body, this selectivity can be tuned by choosing an appropriate complexing ligand. Changed ligands with the same radionuclide can make them selective to different organs in the body [7].

The most commonly used radionuclides ^{186}Re and ^{99m}Tc and, recently, ^{177}Lu have been evaluated with promising results [6]. Other radionuclides, such as ^{153}Sm, ^{166}Ho and ^{117m}Sn, are also commonly used for various applications, but they are complexed with ligands containing different phosphorous based groups [5,6].

1.3 HEDP properties

HEDP, like most other bisphosphonates, is a tetraprotic acid and therefore has various forms having different degrees of protonation, such as H_4L, H_3L^-, H_2L^{2-}, HL^{3-}, L^{4-} where L = $[CH_3C(OH)(PO_3)_2]^{4-}$, that are pH-dependent and whose dissociation constants, pK_a, have been experimentally determined [8] (Table 1-1).

Table 1-1. The dissociation constants of HEDP [8].

Equilibrium reaction	Dissociation constant, pK_a
$H_4L \leftrightarrows H_3L^- + H^+$	2.43
$H_3L^- \leftrightarrows H_2L^{2-} + H^+$	2.97
$H_2L^{2-} \leftrightarrows HL^{3-} + H^+$	6.81
$HL^{3-} \leftrightarrows L^{4-} + H^+$	10.11

HEDP has a high affinity for complexation with metal ions and especially divalent ions, as evidenced from the approximately 23 single-crystal structures that have been reported [9]. As a solid, HEDP crystallises as a monohydrate, but an anhydrous crystalline form also exists above 70 ºC as evidenced by the X-ray diffraction (XRD) powder pattern [10].

To understand the three-dimensional interaction of a bisphosphonate with a surface/interface, it is important to fundamentally investigate the structural aspects of the molecule in its various degrees of protonation and its interaction with bone minerals. As the accepted benchmark molecule in the bisphosphonate family, HEDP would therefore be the logical starting point for a study using various complementary spectroscopic methods, each with its own strengths and weaknesses.

1.4 Hydroxyapatite as a model of bone

Natural bone is a poorly crystalline hydroxyapatite (HA) with the general composition of ±65% w/w mineral component, of which the HA has a crystallinity index of ±35 and is 7.4% carbonated [11]. The rest of the bone matrix is made up mainly of organic compounds (25%) and water (10%) [11]. Synthetic HA, $Ca_{10}(PO_4)_6(OH)_2$, has been used to substitute mineral bone in drug interaction studies, and many other calcium phosphitic compounds have been used extensively in the biological and medical fields for bone replacement or as mimicking agents [11]. HA has been compared with fluorinated, carbonated and biological apatites by means of Raman and IR spectroscopy [12-16] and powder diffraction methods [17, 18]. The main properties of HA have been shown to be similar to those of biological bone apatite. Due to the incorporation of carbonate [18] and thus the absence of OH in the crystal structure [16] of biological bone, it has been found that the interactions of bisphosphonates with bone and synthetic HA may differ [19]. However, chemical interactions have been shown to be very similar for HEDP with both bovine bone and synthetic HA, and therefore HA is still a viable substitute for biological bone in fundamental research [20]. Nevertheless, great care should be taken in the interpretation and extrapolation of interaction results.

1.5 Spectroscopic methods

The various techniques used in this study were chosen for their ability to contribute unique aspects to the understanding of and insight into the conformations of HEDP both in solution and in the solid state, as well as to its behaviour at the solid-solution interface.

NMR spectroscopy was chosen to investigate how pH affects the chemical nature of HEDP as chemical shifts are sensitive to both environmental changes (the solution) and chemical changes (deprotonation of the phosphonate groups) in the molecule. As the chemical shift in this study is a function of pH, the NMR data can also be used to monitor the degree of deprotonation of HEDP.

X-ray diffraction was chosen to investigate the solid-state aspects of HEDP as knowledge of the nature of molecular conformation and interaction in the solid state can be used to compare and rationalise what is observed in solution. Three-dimensional structural data can be obtained from both single crystal and powder XRD techniques. The preferred method is single crystal, but in many cases it is not possible to obtain good-quality single crystals and powder diffraction data are then analysed using the Rietveld method to determine the crystal structure, as in the case of anhydrous HEDP.

Vibrational spectroscopy is a unique technique for giving insight into local internal changes (being of a physical or chemical nature) in a molecule or to the intra/intermolecular interactions of molecules. This is done by analysing the shift or appearance/disappearance of the vibrational bands associated with the molecule of interest in the solid and/or solution phases. Raman spectroscopy is ideally suited to studying molecular interactions at the surface of a solid substrate and will therefore give insight into the interaction of HEDP with HA as a model of bone. Raman spectroscopy is also ideally suited for studying aqueous systems as water is a weak Raman scatterer, while infrared spectroscopy is ideal for observing changes associated with water molecules, as required during the dehydration of HEDP in the solid state. Thus, vibrational techniques will give

great insight into conformers and their interactions, both in the solid state and in solution.

1.5.1 Nuclear magnetic resonance (NMR) spectroscopy

The most important property for an atomic nucleus to be NMR-active is the nuclear spin, I, which can have values of $0 + \frac{1}{2}n$, where n is an element of the natural numbers, in units of $h/2\pi$ [21]. Values of $I = 0$ are indicative of NMR-inactive nuclei. Each nucleus has an associated proportionality constant, γ, called the 'magnetogyric ratio' associated with the nuclear magnetic moment, μ, which is directly proportional to the spin. This relationship can be written as:

$$\mu = \frac{\gamma I h}{2\pi} \tag{1.1}$$

By application of an external magnetic field, the nuclear moments can align themselves in $2I + 1$ orientations having a magnetic quantum number, m_I, with values of $-I, -I + 1, \ldots, I - 1, I$ and this interaction energy for each orientation can be written as [21]:

$$E = -\frac{\gamma h}{2\pi} m_I B \tag{1.2}$$

The NMR selection rules allow for a transition to have $\Delta m_I = \pm 1$, and thus the transition energy is:

$$\Delta E = \left| E_{m_{I+1}} - E_{m_I} \right|$$

$$\Delta E = \frac{\gamma h B}{2\pi} \tag{1.3}$$

from Eq. 1.2.

To detect this transition, external radiation must be applied such that the energy of this radiation, $h\nu$, equals ΔE. Substituting ΔE in Eq. 1.3 for $h\nu$ gives the fundamental resonance condition for the NMR experiment as:

$$\nu = \frac{\gamma B}{2\pi} \tag{1.4}$$

The relative resonance frequency of the fundamental resonance condition for an atomic nucleus in an NMR experiment depends mostly on its magnetic environment, and therefore on the variation in electron density (from chemical bonds and neighbouring atoms) of each nucleus [22]. Measuring this resonance frequency in conjunction with the spin-spin coupling of the nuclei will, in general, allow the determination of at least the connectivity of simple molecules. Comparative NMR spectra will also show whether the chemical environment/character of an atomic nucleus has changed significantly due to a chemical modification to either the environment (change in pH) or the molecule itself (ligand coordination).

In this study the ^{1}H, ^{13}C, ^{31}P and ^{23}Na NMR spectra of HEDP, in the monohydrate and anhydrous forms, as well as the calcium dihydrate salt, were investigated in DMSO-d_6, D_2O and H_2O as solvents to monitor and compare the various structural and conformational changes that occurred in a solution environment.

1.5.2 X-ray diffraction (XRD)

The diffraction of X-rays by the crystal lattice allows the determination of the molecular structure of solids. This requires knowledge of the atoms in a regular crystal system, the lattice parameters and the relative positions and intensities of reflections. Systematic absences of certain families of hkl reflections from the diffraction data allows the assignment of space groups or at least suggests a number of possible space groups to investigate. The condition for diffraction is mathematically described by Bragg's law:

$$2d_{hkl}\sin\theta = n\lambda \quad (n \in N) \tag{1.5}$$

where d_{hkl} is the spacing for the hkl plane, θ the scattering or reflection angle between the radiation and the hkl plane, and n the order of the diffraction [23] . This is graphically represented in Figure 1-2.

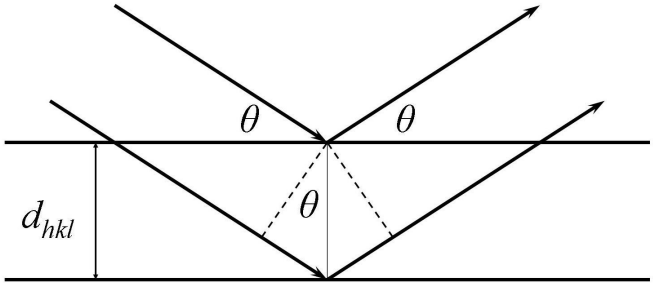

Figure 1-2. Schematic of X-ray diffraction from an hkl lattice plane, with interplanar distance d_{hkl} and diffraction angle θ [23]

1.5.2.1 Single-crystal XRD

Diffraction occurs in a crystal when Bragg's law is satisfied and the structure factor for the reflection, F_{hkl}, can be related to the measured intensity of that hkl plane's diffraction, I_{hkl}, as:

$$I_{hkl} = \left|F_{hkl}\right|^2 \tag{1.6}$$

F_{hkl} can be written as an imaginary function:

$$F_{hkl} = \sum_{j=1}^{N} f_j e^{2\pi i(hx_j+ky_j+lz_j)} \tag{1.7}$$

in which all N atoms, with fractional coordinates x, y and z, in the lattice contribute to an hkl plane, including the atomic scattering factor, f_j, for each atom type, j [23]. F_{hkl} is related to the electron density function, ρ_{xyz}, by the use of a Fourier transformation:

$$\rho_{xyz} = \frac{1}{V} \sum_{h,k,l=-\infty}^{+\infty} F_{hkl} e^{-2\pi i(hx+ky+lz)} \tag{1.8}$$

in which the maxima of ρ_{xyz} correspond to the atomic positions, and thus the crystal structure is solved [23]. A problem arises in the experimental data as seen in Eq. 1.6 when the phase information is not available. Successful methods to solve this problem are well established [23], but will not be discussed here. However, it is worth noting that the validity of the solutions involves the calculation of an R-factor, which is in general defined as:

$$R = \left(\frac{\sum \left| |F_{obs}| - |F_{calc}| \right|}{\sum |F_{obs}|} \right) \tag{1.9}$$

for all reflections. The smaller the value of R, the better the solution fit for the structure.

1.5.2.2 Powder XRD

The complexity of using powder XRD data for crystal structure determination stems from the fact that with this method diffraction is observed as a 'cone' due to the many randomly orientated crystallites, and thus three-dimensional data are compressed into one dimension [24]. Further complications arise from the fact that the data profile and the quality of data required are extremely dependent on the instrumentation, as evidenced by the number of factors that are weighted when attempting to solve an XRD powder pattern [24]. The structural solution of an XRD powder pattern follows a very similar method to that for single-crystal XRD, in which indexing, crystal system and lattice parameter determination, and space group identification become intrinsically more difficult due to the compression of the three-dimensional data into one dimension [24]. The most popular and effective method utilised at various stages of such an analysis is the Rietveld method [24], which will be discussed in more detail in Section 1.6.3.

Even though it would appear that attempting the solution of a crystal structure by utilising powder XRD data is extremely labour-intensive, it is the best method in the absence of single-crystal data of diffraction quality.

1.5.3 Vibrational spectroscopy

The energy of a molecule can be summarised as one of four components:

$$E_T = E_{trans} + E_{e^-} + E_{vib} + E_{rot} \tag{1.10}$$

The study of the vibrational energy associated with a molecule, E_{vib}, uses the two complementary techniques of infrared (IR) and Raman spectroscopy. A very comprehensive review of these two techniques and their applications can be found in reference [25] – only a concise synopsis of the two techniques is presented here. The relationship between IR and all Raman processes is shown schematically in Figure 1-3.

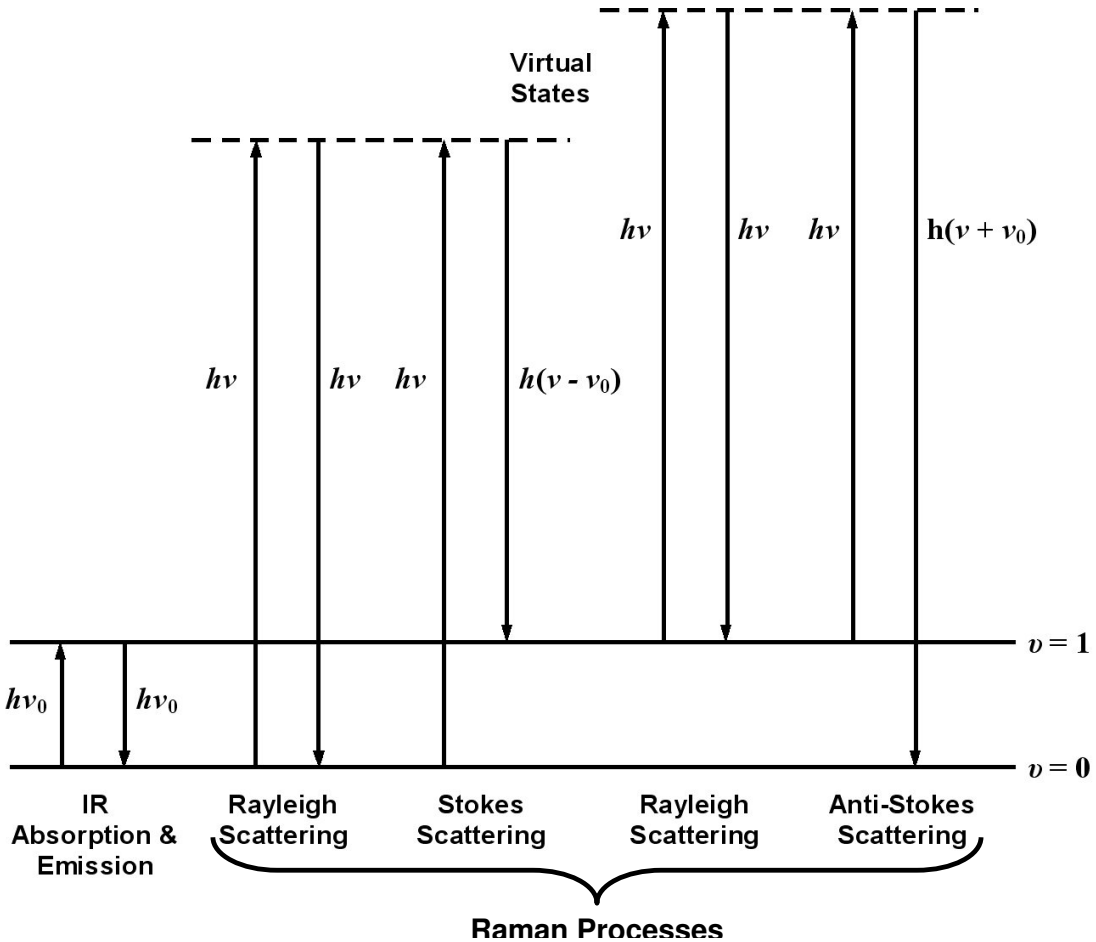

Figure 1-3. Schematic showing the difference between the various vibrational processes

1.5.3.1 Infrared (IR) spectroscopy

IR spectra originate from the absorption of a photon between two vibrational energy levels. In general, a vibrational mode is IR-active when the dipole moment, μ, associated with the mode is non-zero. From quantum mechanics it is shown that molecular vibrational energy levels are quantised and that the dipole moment of an associated vibration will couple with the electric field of the IR radiation, ν_{IR}, only when the associated energy of this IR radiation matches that of a specific vibrational energy level of the molecule, allowing the absorption and emission of IR photons by vibrational energy levels in the molecule's electronic ground state [26]. The frequency measured during IR absorption can be formulated as being:

$$\nu_{IR} = \frac{d\mu}{dx} \tag{1.11}$$

which describes the change of the permanent dipole moment, $d\mu$, as the molecule vibrates, dx.

1.5.3.2 Raman spectroscopy

Raman spectroscopy is a scattering technique during which a sample is irradiated with a single wavelength source (i.e. a laser) and electronic polarisation is induced in the dipole associated with a vibrational mode. Three scattering processes can occur when the sample is irradiated: Rayleigh, Stokes and anti-Stokes scattering. Rayleigh scattering occurs when the frequency of the scattered radiation equals that of the incoming radiation [26]. When the scattered radiation's frequency differs from that of the incident radiation, Stokes/anti-Stokes scattering occurs and it is the frequency difference between the incident and scattered radiation that is of interest to the spectroscopist. From classical theory these processes can be summarised as:

$$\mu_i = \alpha_0 E_0 \cos 2\pi\nu t + \frac{1}{2}\left(\frac{\partial\alpha}{\partial x}\right)_0 x_0 E_0 \{\cos[2\pi(\nu+\nu_0)t] + \cos[2\pi(\nu-\nu_0)t]\} \tag{1.12}$$

where the first term describes Rayleigh scattering and the last term the anti-Stokes ($\nu + \nu_0$) and Stokes ($\nu - \nu_0$) scattering [26] with the induced dipole moment, μ_i, dependent on the polarisability, α. In practice, Stokes scattering is mostly measured because it originates from the $\upsilon = 0$ vibrational level which is more populated than the $\upsilon = 1$ level from where the anti-Stokes scattering originates (see Figure 1-3), as described by the Boltzman distribution of these levels at ambient temperatures [26].

1.6 Molecular modelling

Molecular modelling is used to assist with and/or confirm many aspects of experimental chemistry. If the theory is an acceptable description of the system of interest, a wealth of information can be obtained theoretically, which would usually be very time-consuming to obtain experimentally. In the case of HEDP, the vibrational spectra are complex and many ambiguous, overlapping bands are observed, making empirical assignment very difficult. Calculation of the theoretical spectra can therefore be used to confidently identify and confirm bands that can be associated with chemical or conformational changes, as well as the associated intra/intermolecular interactions.

1.6.1 The theoretical method

Two main methods are used in molecular modelling: molecular mechanics (MM), which is based on the laws of classical physics, and the electronic structure method, which is based on quantum mechanics [27]. The latter can be divided into semi-empirical, *ab initio* and density functional theory (DFT); the most widely used of these is the DFT method which takes the effects of electron correlation into account [27]. The DFT method is very similar to the *ab initio* Hartree-Fock (HF) method, but here the electron is assumed to interact with an 'averaged electron density' [27].

In the DFT method, the electronic energy, E^e, can be seen as a summation of the electrons' kinetic energy, E^t, the potential energy of the nuclear-electron interaction, E^v, the electron-electron repulsion energy, E^j, and the exchange correlation term, E^{xc}, that describes the rest of the electron-electron interactions [27]:

$$E^e = E^t + E^v + E^j + E^{xc} \tag{1.13}$$

It is the numerical integration evaluation of the E^{xc} term that makes DFT the superior method to HF, but at the cost of calculation complexity. The E^{xc} term is a functional of the electron density function, ρ, and can be separated into the exchange and correlation functionals, $E^x(\rho)$ and $E^c(\rho)$, respectively:

$$E^{xc}(\rho) = E^x(\rho) + E^c(\rho) \tag{1.14}$$

A pure DFT functional (E^{xc}) is usually defined by pairing an exchange functional with a correlation functional as in the case of the BLYP functional where a Becke (B) defined functional (E^x) is combined with a Lee-Yang-Parr (LYP) functional (E^c) [27].

DFT hybrid functionals have also been defined where the E^{xc} term contains an HF-type E^x term contribution as HF theory contains an E^x term as part of its own formulation [27]. Thus,

$$E^{xc}_{hybrid} = c_{HF} E^x_{HF} + c_{DFT} E^{xc}_{DFT} \tag{1.15}$$

where the c's are constants. As an example, the classical B3LYP hybrid exchange-correlation functional could be defined as:

$$E^{xc}_{B3LYP} = E^x_{LDA} + c_0\left(E^x_{HF} - E^x_{LDA}\right) + c_x \Delta E^x_{B88} + E^c_{VWN3} + c_c\left(E^c_{LYP} - E^c_{VWN3}\right) \tag{1.16}$$

where LDA, B88 and VWN3 and LYP are all exchange or correlation functionals defined in the literature [27].

1.6.2 Basis sets

For a theoretical calculation it is also necessary to describe mathematically the orbitals that combine to approximate the total electronic wavefunction of the system under investigation [27]. Better orbital descriptions implies larger basis sets, which lead to longer calculation times being required.

There are three main ways to enlarge the description of an atomic orbital:

(1) Create split-valence basis sets in which two or more basis functions describe the same orbital, although these descriptions will differ in size. One can also have triple split-valence sets which use three contracted descriptions for each orbital type. An example of such a basis set is 6-311 [27].

(2) Introduce polarisation functions into the basis sets that describe the orbitals, with angular momentum beyond the ground-state description for the atom, such as p-orbital functions to s-orbital descriptions or d-orbital functions to p-orbital descriptions. This can be justified by arguing that because molecules are not a grouping of non-interacting separate atoms, a better description of the orbitals can be obtained by describing a possible change in shape of the atomic orbitals [27]. Their addition is indicated in brackets (a,b), where a indicates the function added to heavy atoms and b the function added to hydrogen atoms. Basis sets with higher angular momentum have more than one type of function added to either heavy or hydrogen atoms and can even have more than one of the same type of function added, indicated by a numerical coefficient in the bracket, e.g. (2df,3pd).

3) Enlarge the basis set by adding diffuse functions to the orbital description, which allows larger versions of the s- and p-orbital types. This is important for systems in which the electrons are further than normal from the nucleus, e.g. where there are lone pairs present or the system is anionic in nature [27]. In the basis set description, “+” denotes that diffuse functions are added only to heavy atoms, and “++” denotes that diffuse functions are

added to hydrogen atoms as well [27]. A graphical summary with examples of basis sets of all these effects is given in Table 1-2.

Table 1-2. Graphical representation of the different effects that can be added to expand the basis set used during molecular modelling [27]

Basis set effects	Graphical representation	Basis set examples
Split valency	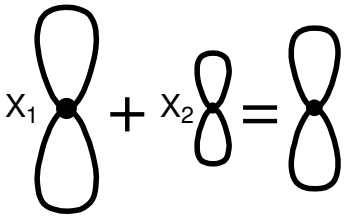	3-21G 6-31G 6-311G
Polarisation	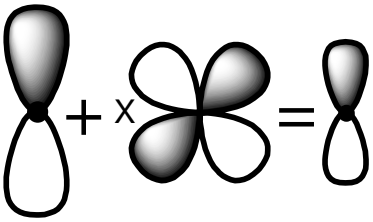	3-21G(d) 6-31G(d,p) 6-311(2df,3pd)
Diffuseness	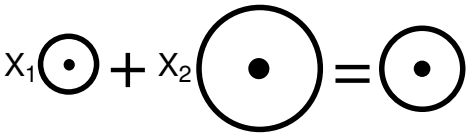	6-31G+(d,p) 6-311++(2df,3pd)

1.6.3 The Rietveld method

The Rietveld method is said to be the most powerful method for extracting solid-state structural information on a compound from experimentally obtained powder XRD patterns, and is based on the deceptively simple rationale of minimising parameters such that the residual quantity

$$S_y = \sum_{i=1}^{i} w_i \left(y_i - y_{ci}\right)^2 \qquad (1.17)$$

approximates zero during the least-squares refinement [24], where y_i and y_{ci} are the observed and calculated intensities at the ith step of the powder pattern, respectively, and $w_i = 1/y_i$. The complexity of the Rietveld method only becomes

apparent when the calculated intensity, y_{ci}, for the ith step is defined with all the necessary parameters during the refinement process:

$$y_{ci} = s \sum_{h,k,l=-\infty}^{\infty} L_{hkl} \left| F_{hkl} \right|^2 \phi(2\theta_i - 2\theta_{hkl}) P_{hkl} A + y_{bi} \tag{1.18}$$

The variables L_{hkl}, F_{hkl} and P_{hkl} are all separate functions for an hkl reflection, as allowed by Bragg's law (Eq. 1.5), defining the Lorentz, polarisation and multiplicity factors, the structure factor (similar to Eq. 1.7) and the preferred orientation function respectively [24]. s is a scaling factor, ϕ the reflection profile function, A the absorption factor and y_{bi} the background intensity at the ith step defined at least as a 5th order polynomial [24]. All of the factors and functions are instrument- and/or sample-dependent, and this is where the real complexity and difficulty of Rietveld refinement is experienced.

As with the single XRD case, Rietveld refinement has certain criteria of fit that have the same function as Eq. 1.9. As a result of so many variables having to be optimised simultaneously, various criteria of fit have been defined, of which the following are important: the R-structure factor

$$R_F = \frac{\sum \left| \sqrt{I_{K-observed}} - \sqrt{I_{K-calculated}} \right|}{\sum \sqrt{I_{K-observed}}} \tag{1.19}$$

the R-Bragg factor

$$R_B = \frac{\sum \left| I_{K-observed} - I_{K-calculated} \right|}{\sum I_{K-observed}} \tag{1.20}$$

the R-pattern

$$R_p = \frac{\sum \left| y_i - y_{ic} \right|}{\sum y_i} \tag{1.21}$$

and the R-weighted pattern

$$R_{wp} = \sqrt{\frac{\sum w_i (y_i - y_{ic})^2}{\sum w_i (y_i)^2}} \quad (1.22)$$

R_{wp} and R_B are most often used, but all the criteria are examined to decide whether the structure solution is valid as it can be seriously inflated by external factors such as sample impurity or can be deflated by factors such as significantly high background profiles [24].

1.7 Aim

The general use of bisphosphonates in bone degenerative diseases has been outlined, as well as the techniques and methods employed in this thesis. Very little is known about the interactions of bisphosphonates with bone on a fundamental, molecular as indicated by an analysis of available literature. Therefore the need exists for a more fundamental study of these compounds. HEDP is the oldest known, benchmark and chemically simplest bisphosphonate and would therefore be the most logical point to start such an investigation using hydroxyapatite as a simplified model for bone.

In all fundamental studies the validation of both theoretical and experimental methods are important. Therefore many relevant spectroscopic techniques as earlier described were used and the experimental data rationalised by theoretical calculations / methods.

It is therefore the aim of this thesis to investigate the interaction of HEDP with hydroxyapatite as a model of bone on a fundamental level using these various techniques for future extension and methodology development to study other bisphosphonates and solution/solid interaction environments more relevant to cancerous environments in the human body.

1.8 References

[1] R.G.G. Russell. *Ann. N.Y. Acad. Sci.* **2006**, *1068*, 367.

[2] H.A. Fleisch, R.G.G. Russell, F. Straumann. *Clin. Sci.* **1966**, *31*, 461.

[3] H.A. Fleisch, R.G.G. Russell, S. Bisaz, R.C. Mühlbauer, D.A. Williams. *Eur. J. Clin. Invest.* **1970**, *1*, 12.

[4] H.A. Fleisch. *Endocr. Rev.* **1998**, ***19***, 80.

[5] V.J. Lewington. *Phys. Med. Biol.* **1996**, *41*, 2027.

[6] V. Lungu, D. Niculae, P. Bouziotis, I. Pirmettis, C. Podina. *J. Radioanal. Nucl. Ch.* **2007**, *273*, 663.

[7] J.R. Zeevaart. *Metal-ion Speciation in Blood Plasma as a Tool in Predicting the in vivo Behaviour of Potential Bone-seeking Radiopharmaceuticals*, Delft University Press, Delft, **2001**, Chapter 1.

[8] J.R. Zeevaart, N.V. Jarvis, I. Cukrowski, G.E. Jackson. *S. Afr. J. Chem.* **1997**, *50*, 189.

[9] J.P. Silvestre, N.Q. Dao, Y. Leroux. *Heteroatom Chem.* **2001**, *12*, 73.

[10] E.G. Afonin, G.G. Aleksandrov. *Russ. J. Gen. Chem.* **2003**, *73*, 340.

[11] S.G. Dorozhkin, M. Epple. *Angew. Chem. Int. Ed.* **2002**, *41*, 3130.

[12] M.A. Walters, Y.C. Lang, N.C. Blumenthal, R.Z. le Geros, I.L.A. Konsker. *J. Inorg. Biochem.* **1990**, *39*, 193.

[13] G. Penel, G. Leroy, C. Rey, B. Sombret, J.P. Huvenne, E. Bres. *J. Mater. Sci – Mater. M.* **1997**, *8*, 271.

[14] G. Penel, C. Delfossea, M. Descamps, G. Leroy. *Bone* **2005**, *36*, 893.

[15] A. Antonakos, E. Liarokapis, T. Leventouri. *Biomaterials* **2007**, *28*, 3043.

[16] J.D. Pasteris, B. Wopenka, J.J. Freeman, K. Rogers, E. Valsami-Jones, J.A.M. van der Houwen, M.J. Silva. *Biomaterials* **2004**, *25*, 229.

[17] T. Leventouri, B.C. Chakoumakos, N. Papaneachou, V. Perdikatsis. *J. Mater. Res.* **2001**, *16*, 2600.

[18] T. Leventouri. *Biomaterials* **2006**, *27*, 3339.

[19] G.H. Nancollas, R. Tang, R.J. Phipps, Z. Henneman, S. Gulde, W. Wu, A. Mangood, R.G.G. Russell, F.H. Ebetino. *Bone* **2006**, *38*, 617.

[20] I. Cukrowski, L. Popović, W. Barnard, S.O. Paul, P.H. van Rooyen, D.C. Liles. *Bone* **2007**, *41*, 668.

[21] R.J. Abraham, J. Fisher, P. Loftus. *Introduction to NMR Spectroscopy,* 2nd Edition, John Wiley & Sons, Chichester, **1988**, Chapter 1.

[22] D.H. Williams, I. Fleming. *Spectroscopic Methods in Organic Chemistry,* 5th Edition, McGraw-Hill, Bath, **1995**, Chapter 3.

[23] C. Giacovazzo (Ed.). *Fundamentals of Crystallography*, Oxford University Press, Oxford, **1992**, Chapter 3.

[24] R.A. Young (Ed.). *The Rietveld Method*, Oxford University Press, Oxford, **1996**.

[25] J.M. Chalmers, P.R. Griffiths. *Handbook of Vibrational Spectroscopy,* 2nd Edition, John Wiley & Sons, Chichester, **2002**, all volumes.

[26] K. Nakamoto. *Infrared and Raman Spectra of Inorganic and Coordination Compounds,* 5th Edition, John Wiley & Sons, Chichester, **1997**, Part A.

[27] J.B. Foresman, Æ. Frisch. *Exploring Chemistry with Electronic Structure Methods,* 2nd Edition, Gaussian Inc., Pittsburgh, **1996**.

2 Experimental

2.1 Introduction

This chapter contains the necessary information for the description of each experiment performed to study the surface interactions of HEDP(aq), as well as HEDP in solution and in the solid state. The choice of each of the main techniques has been discussed in Chapter 1. These techniques are all necessary to obtain a global view of the surface interactions of HEDP, as well as to characterise HEDP itself and in solution.

2.2 Chemicals

HEDP was purchased from Fluka >97% and Dayang Chemicals >99%, and used as is for the preparation of the 0.5 M solutions and for solid-state investigations. The monohydrate form of HEDP was obtained by recrystallisation from deionised, distilled water, and the anhydrous form was obtained by heating HEDP at 120 ºC to ensure that all water of hydration and all adsorbed water was removed [1]. $Ca(OH)_2$ ≥ 95% and H_3PO_4 (85% in H_2O) were purchased from Sigma-Aldrich and hydroxyapatite (BIO-RAD, BIO-GEL®-HTP Gel) was obtained from Chemlab, Bryanston, South Africa.

$CaHPO_4$ was prepared by adding 3 g of $Ca(OH)_2$ to 4.86 ml of a 5 M phosphoric acid solution at boiling point, after which the desired product precipitated and was filtered, washed with distilled water and dried overnight at 120 ℃ [2]. The calcium dihydrate salt of HEDP, $Ca(CH_3C(OH)(PO_3H)_2)\cdot 2H_2O$ ($CaH_2L\cdot 2H_2O$), was prepared by adding $Ca(OH)_2$ to an HEDP solution in the molar ratio of 1:1. The desired product immediately precipitates out as it is only sparingly soluble at higher pH values and this precipitated complex was filtered and washed with deionised water and left to air-dry overnight [2]. The single crystal used for XRD

analysis was grown from a solution containing 25 mg of HA dissolved in 0.5 M of HEDP [2]. The bovine bone used was obtained from a local abattoir and treated with H_2O_2 and acetone [2] to remove as much of the organic component as possible.

The pH series of solutions used for the ^{31}P NMR study and Raman spectra Multivariate Curve Resolution analysis were prepared by titrating an initial solution of 20 ml of 0.5 M HEDP with a 0.5 M NaOH solution using a Metrohm 765 Dosimat autotitrator, that was calibrated by the two point calibration method. Sampling was done at pH intervals of 0.20 close to the equivalence points or at intervals of 0.50 away from them. This resulted in a sample set of 50 different pH values over the pH range 0.98 – 13.00. Each sample was placed in a separate NMR tube and used for both the NMR and FT-Raman analyses.

2.3 NMR spectroscopy

The NMR spectra of HEDP monohydrate ($H_4L{\cdot}H_2O$) and the anhydrous (H_4L) forms, as well as $CaH_2L{\cdot}2H_2O$, were obtained with DMSO-d_6 and D_2O as solvents. The spectra of the NaOH-titrated solutions were measured in H_2O as solvent.

2.3.1 ^{1}H and ^{13}C nuclei

The ^{1}H and ^{13}C spectra measured in DMSO-d_6 were referenced to the deuterated DMSO itself at 2.49 and 39.5 ppm respectively. All ^{1}H and ^{13}C measurements in D_2O and H_2O were referenced using an internal standard probe of $CDCl_3$ having saturation-recovery (SR) values of 4 100.56 Hz for the ^{1}H and –1 928.13 Hz for the ^{13}C data. All ^{1}H and ^{13}C spectra were measured on a Bruker ARX-300 spectrometer at 300.135 and 75.469 MHz respectively.

2.3.2 ^{31}P and ^{23}Na nuclei

All ^{31}P spectra were measured on a Bruker ARX-300 spectrometer at 121.46 MHz and referenced to 85% H_3PO_4 in H_2O at 0.00 ppm. The ^{23}Na data were collected at 132.26 MHz on a Bruker AVANCE-500 spectrometer and referenced to 1.0 M NaBr in H_2O.

2.4 Thermal gravimetric analysis

Data for HEDP·H_2O were collected using a Mettler/Toledo TGA/SDT851^e instrument. Thermal events were registered under a nitrogen atmosphere, in the range 25 – 300 ºC, with the temperature gradient set to 10 ºC per minute.

2.5 X-ray diffraction methods

2.5.1 Single-crystal X-ray diffraction

The single X-ray crystal structure analysis was performed using data collected at 20 ºC on a Siemens P4 diffractometer fitted with a Bruker 1K CCD detector and SMART control software [3] using graphite-monochromated, Mo-Kα radiation by means of a combination of ϕ and ω scans. Data reduction was performed using SAINT+ [3] and the intensities were corrected for absorption using SADABS [3]. The structure was solved by direct methods using SHELXTS [3] and refined by full-matrix least squares using SHELXTL [3] and SHELXL-97 [4].

All the hydrogen atoms were located experimentally and were included in the refinement. For the determination of $CaH_2L{\cdot}2H_2O$ (Figure 3-12A), a half-occupancy was assigned to the H5 and H6 atoms, which represent a disordered hydroxyl group bonded to P2, and equally distributed between O5 and O6. Also, H5 and H6 were allowed to ride on O5 and O6 respectively with $d_{O–H}$ = 0.82(1) Å, and the P-O–H angle made tetrahedral and allowed to rotate about the corresponding O-P bond. The isotropic displacement parameters of H5 and H6 were fixed at 1.5 times the equivalent isotropic displacement parameters of O5

and O6 respectively. The crystal data and refinement tables for $H_4L \cdot H_2O$ and $CaH_2L \cdot 2H_2O$ can be found in Tables A-1 and A-2 in the Appendix.

Perspective drawings of the structures of $H_4L \cdot H_2O$ and $CaH_2L \cdot 2H_2O$ were produced using Ortep-3 for Windows (version 1.076) [5], Mercury (version 1.4.2) [6] and POV-Ray for Windows (version 3.6) [7].

2.5.2 Powder X-ray diffraction

The powder XRD analysis was performed using a PANalytical X-pert Pro powder diffractometer with variable divergence and receiving slits, and an X'celerator detector using Fe-filtered Co-Kα radiation. Data were collected over the 2θ angle range of 5.0 – 90.0º. Data collection for H_4L was performed using an Anton Paar HTK 16 heating chamber with a Pt-heating strip both at room temperature and at 120 ºC, with a waiting time of 30 minutes at 120 ºC before data accumulation commenced. For the Rietveld refinement procedure, Y_2O_3 annealed at 1 200 ºC was also measured as a reference for instrument parameter refinement.

2.6 Rietveld refinement

The instrument parameters were refined by using the powder pattern of annealed Y_2O_3 as reference; the unit cell constants' parameters were kept constant and the instrument parameters were allowed to refine. All indexing and refinement procedures were done using the TOPAS Academic [8] software package.

The powder X-ray diffraction pattern of anhydrous HEDP was indexed and a Pawley [9] and Le Bail [10] fitting for the 2θ range 5 – 45º done for comparison, during which the cell parameters were refined using the instrument profile as obtained from the Y_2O_3 refinement. Structure determination was attempted using a 'first guess' rigid-body description of HEDP obtained from the known $HEDP \cdot H_2O$ structure which contained only the non-hydrogen atoms for the 2θ range 5 – 45º. After the best fit had been obtained by means of the rigid-body refinement procedure, all non-hydrogen atomic positions were allowed to be

refined independently until an optimal and acceptable R-value was obtained with a molecular solution that also made chemical sense.

2.7 Molecular modelling

Structural optimisations and vibrational spectra calculations were performed using Gaussian03 software [11], employing the 6-311++G(d,p) basis set unless otherwise stated.

For the calculation of the vibrational spectra of $CaH_2L \cdot 2H_2O$, the starting conformation coordinates from the crystallographic structure solution were used without further structural optimisation, and one full unit cell was necessary to reproduce the vibrational spectrum satisfactorily. The Hartree-Fock (HF/6-311++G(d,p)) level of theory was selected, based on initial evaluation of similar, simple systems modelled with analogous Density Functional Theory (DFT) which showed satisfactory comparisons for the region below 2000 cm^{-1}. The scaling factor used was determined to be 0.9051 [12].

Conformers of the various protonated forms of HEDP (H_3L^-, H_2L^{2-}, HL^{3-}, L^{4-}) in solution were generated from the known single-crystal structure of $H_4L \cdot H_2O$ [13]. Initial solvated, conformers for H_4L were generated using Macromodel 9.6207 of the Schrödinger Software Suite, utilising the MM/OPLS-2005 force field. The default solvation settings in Macromodel were used. All conformers of interest were then further optimised using the Gaussian03 software [11] performing the DFT calculations at the B3LYP/6-311++G(d,p) level of theory in conjunction with the SCRF IEF-PCM/UA0 solvation model. Final validity of all generated conformers during this very preliminary conformational analysis was based on the generation of imaginary frequencies during the final DFT calculations.

The hybrid functional B3LYP was selected, as it is widely used in literature and gives acceptable results regarding structural properties. It was decided to add diffusion functions (++), as ionic systems are also being modelled. The polarisation functions (d,p) were added to both non-hydrogen and hydrogen

atoms to ensure a better modelling of hydrogen bond interaction in the molecule(s). The solvation model as well as all other settings are default for the Gaussian03 package and are well known to give acceptable results.

2.8 Vibrational spectroscopy

2.8.1 Raman spectroscopy

Various experimental solid-state and solution Raman spectra were obtained using both a dispersive and an FT-Raman spectrometer.

All dispersive spectra were obtained by exciting the samples with the 514.5 nm (green) line of a Coherent Innova 300 Argon-ion laser. For the solid-state spectra, an Olympus confocal microscope with a 50X objective was used to focus the laser light on the sample or at a solid-liquid interface. The scattered light was dispersed and recorded by means of a Dilor XY multichannel Raman spectrometer equipped with a liquid nitrogen-cooled Wright Generation 1 CCD detector. The spectral resolution was 3 cm^{-1}, while laser output power at the source (300 – 500 mW) and integration times (30 – 120 seconds) was varied to obtain the best possible spectra. Three to four spectral accumulations were averaged, and the software used for data processing was Labspec 3.03.

A Linkam RMS 90 heating cell was employed to obtain the solid-state Raman spectrum for non-ambient conditions at 120 ºC, and the macro-Raman solution spectra on the dispersive system were obtained in an NMR tube using a 50 mm lens in a 180º backscattering geometry. The *in situ* Raman measurements that were done to monitor the interaction of HEDP with bone, HA and $CaHPO_4$ were performed on the dispersive instrument using the confocal microscope, by adding HEDP solution (0.5 – 0.005 M) onto solid HA or $CaHPO_4$ (on a microscope slide) and sequentially recording the Raman spectra until no further change was observed.

The FT-Raman spectra of the HEDP solutions were obtained in NMR tubes by using a Bruker IFS 100 FT-Raman spectrometer fitted with a liquid N_2-cooled Ge detector. All solid-state spectra were measured directly on the surface of the solid. All spectra were recorded for the region 100 – 3500 cm^{-1} using the 1 064 nm excitation line of an Nd:YAG laser operating at approximately 300 mW at the sample. The spectral resolution was 4 cm^{-1} and the spectra were signal-averaged over 128 – 512 scans as required, and processed using OPUS 5.5 software.

2.8.2 Fourier transform infrared (FTIR) spectroscopy

FTIR spectra were obtained under vacuum as a 1% w/w KBr disk using a Bruker IFS 113 spectrometer over the region 400 – 4000 cm^{-1} with a spectral resolution of 4 cm^{-1}. OPUS 5.5 software was used for data processing. The FTIR spectrum for HEDP at 120 ºC was obtained by heating the KBr pellet at 120 ºC for two hours, after which the pellet was immediately transferred to the spectrometer for spectral accumulation under vacuum.

2.9 Multivariate Curve Resolution (MCR)

The MCR routine of The Unscrambler® version 9.6 (CAMO Process AS, Oslo, Norway) was used for the pure component analysis of the bands in the wavenumber range 860 – 1280 cm^{-1}. This range was specifically chosen to include only those vibrational bands associated with the PO_3H_2 moieties. Non-negativity (for concentration values) and unimodality constraints were included for certain of the MCR analyses as required. The experimental spectra were modified with baseline offset and linear baseline correction before the MCR analysis commenced.

2.10 References

[1] E.G. Afonin, G.G. Aleksandrov. *Russ. J. Gen. Chem.* **2003**, *73*, 340.

[2] I. Cukrowski, L. Popović, W. Barnard, S.O. Paul, P.H. van Rooyen, D.C. Liles. *Bone* **2007**, *41*, 668.

[3] SMART (Version 5.054), SAINT (Version 6.45), SADABS (Version 2.10) and SHELXTS/SHELXTL (Version 6.12). Bruker AXS Inc., Madison, Wisconsin, USA, **2001**.

[4] SHELXS-97 and SHELXL-97. Sheldrick, GM University of Göttingen, Germany, **1997**.

[5] L.J. Faruggia. *J. Appl Crystallogr*. **1997**, *30*, 565.

[6] Mercury (Version 1.4.2). Cambridge Crystallographic Data Centre, http://www.ccdc.cam.ac.uk, **2007**.

[7] POV-Ray for Windows. (Version 3.6) Persistence of Vision Raytracer (Pty) Ltd., Victoria, Australia, http://www.povray.org, **2004**.

[8] A.A. Coelho, *J. Appl. Cryst.* **2000**, *33*, 899.

[9] G.S. Pawley. *J. Appl. Crystallogr.* **1981**, *14*, 357.

[10] A. Le Bail, H. Duroy, J.L. Fourquet. *Mater. Res. Bull.* **1988**, *23*, 447.

[11] M.J. Frisch, G.W. Trucks, H.B. Schlegel, G.E. Scuseria, M.A. Robb, J.R. Cheeseman, J.A. Montgomery, T. Vreven, K.N. Kudin, J.C. Burant, J.M. Millam, S.S. Iyengar, J. Tomasi, V. Barone, B. Mennucci, M. Cossi, G. Scalmani, N. Rega, G.A. Petersson, H. Nakatsuji, M. Hada, M. Ehara, K. Toyota, R. Fukuda, J. Hasegawa, M. Ishida, T. Nakajima, Y. Honda, O. Kitao, H. Nakai, M. Klene, X. Li, J.E. Knox, H.P. Hratchian, J.B. Cross, V. Bakken, C. Adamo, J. Jaramillo, R. Gomperts, R.E. Stratmann, O. Yazyev, A.J. Austin, R. Cammi, C. Pomelli, J.W. Ochterski, P.Y. Ayala, K. Morokuma, G.A. Voth, P. Salvador, J.J. Dannenberg, V.G. Zakrzewski, S. Dapprich, A.D. Daniels, M.C. Strain, O. Farkas, D.K. Malick, A.D. Rabuck, K. Raghavachari, J.B. Foresman, J.V. Ortiz, Q. Cui, A.G. Baboul, S. Clifford, J. Cioslowski, B.B. Stefanov, G. Liu, A. Liashenko, P. Piskorz, I. Komamori, R.L. Martin, D.J. Fox, T. Keith, M.A. Al-Laham, C.Y. Peng, A. Nanayakkara, M. Challacombe, P.M.W. Gill, B. Johnson, W. Chen, M.W. Wong, C. Gonzalez, J.A. Pople. Gaussian03, Revision D.01, **2004**.

[12] A.P. Scott, L. Radom. *J. Phys. Chem*. **1996**, *100*, 16502.

[13] J.P. Silvestre, N.Q. Dao, G. Heger, A. Cousson. *Phosphorus Sulphur* **2002**, *177*, 277.

3 Results & Discussion

3.1 Introduction

No single experimental technique can yield a full understanding of the chemical nature of HEDP or its conformers and/or their interactions in solution or with hydroxyapatite. NMR spectroscopy was used to study the chemical change that occurs as a function of pH. Raman spectroscopy was extensively used to study both the solid state of HEDP and HEDP in solution as a function of pH. The solid-state structural aspects of HEDP and its anhydrous form were investigated by single crystal and powder XRD methods, respectively, and speciation in solution was done using chemometrical methods. All these results and findings are presented in this chapter.

3.2 NMR Spectroscopy

3.2.1 ^{1}H, ^{13}C and ^{31}P nuclei

The observed chemical shifts in the ^{1}H and ^{13}C NMR spectra of HEDP·H_2O are easily assignable as a maximum of only three and two differentiable signals respectively is expected. As two of the three proton signals are of an acidic nature (the PO**H** and CO**H** protons), it would be expected that only one of the three (the C$\mathbf{H_3}$ protons) would be observed when measuring in D_2O as solvent. This was indeed observed and is confirmed by a previous report in the literature showing only a single proton chemical shift [1]. Using D_2O as a solvent would not have allowed anhydrous HEDP to be compared with HEDP·H_2O. Therefore, to observe the acidic protons for both anhydrous and monohydrate HEDP, the solvent was changed to DMSO-d_6 and dryness was confirmed by doing a blank run. As expected, the ^{13}C data were two signals in all cases, irrespective of the

solvent. All the NMR chemical shifts were assigned and coupling constants calculated; these can be found in Table 3-1.

The most notable feature is the change in the chemical shifts associated with the PO**H** and CO**H** protons for HEDP·H_2O and HEDP from 7.9 and 2.1 ppm to 10.1 and 5.7 ppm respectively, as measured in DMSO-d_6. This is attributed to the absence of dissolved crystal water in the anhydrous case. The chemical shifts in the ^{13}C NMR spectra do not differ significantly between the anhydrous and monohydrate HEDP when measured in DMSO-d_6. However, when the ^{13}C chemical shifts for HEDP·H_2O when measured in DMSO-d_6 are compared with those measured in D_2O, there is a significant change. The two observed ^{13}C signals shift from 69.3 and 19.9 ppm when measured in DMSO-d_6 to 79.6 and 28.6 ppm respectively when measured in D_2O. This dramatic change is attributed to the fact that in D_2O other less protonated forms are observed rather than only the H_4L form of HEDP, which one would be more likely to observe in DMSO-d_6. Even though this is not ideal, direct comparison of published solid-state ^{13}C NMR chemical shift data on HEDP [2] with those obtained in DMSO-d_6 seems to support this hypothesis as the published solid-state values of 70.1 and 17.1 ppm for the **C**OH and **C**H_3 nuclei respectively compare well with the values of 69.3 and 19.9 ppm obtained in DMSO-d_6. The ^{31}P chemical shift seems to be solvent dependent only as one goes from DMSO-d_6 to D_2O for HEDP, but a discrepancy noted during the comparison of the experimental data with the data published in the literature [1, 3] indicated that other factors, such as pH and therefore H_4L concentration, might contribute significantly to the position of the ^{31}P chemical shift in D_2O; this will be discussed in Section 3.2.2.

Table 3-1. ^{1}H, ^{13}C, ^{31}P NMR chemical shift (δ) and coupling constant (J) data for HEDP·H_2O and HEDP measured in A. DMSO-d_6 and B. D_2O as solvent

A. *DMSO-d_6*	HEDP·H_2O δ (ppm)	HEDP·H_2O J (Hz)	HEDP δ (ppm)	HEDP J (Hz)
PO**H**	7.9 (b)	-	10.1 (b)	-
CO**H**	2.1 (s)	-	5.7 (s)	-
C**H$_3$**	1.4 (t)	$^{3}J_{H,P}$ = 15.8	1.4 (t)	$^{3}J_{H,P}$ = 15.9
O**H$_2$**	3.8 (s)	-	-	-
COH	69.3 (t)	$J_{C,P}$ = 150.8	69.4 (t)	$J_{C,P}$ = 151.7
CH$_3$	19.9 (s)	-	19.9 (s)	-
P	25.2 (t)	$J_{P,C}$ = 148.8	25.1 (t)	$J_{P,C}$ = 149.8
B. *D_2O*				
PO**H**	-	-		
CO**H**	-	-		
C**H$_3$**	1.4 (t)	$^{3}J_{H,P}$ = 15.8		
COH	79.6 (t)	$J_{C,P}$ = 148.1		
CH$_3$	28.6 (s)	-		
P	21.7 (t)	$J_{P,C}$ = 150.0		

Geunin *et al*. [1] report that there are two ^{31}P chemical shift values for HEDP·H_2O at 25.3 and 18.7 ppm due to the fact that the two phosphonic acid groups are crystallographically non-equivalent in the solid state; one group is strongly hydrogen-bonded to the single molecule of H_2O found in the molecular unit. Therefore, in solution, it could be expected that the non-hydrogen-bonded ^{31}P solid-state chemical shift should be comparable, as in the ^{13}C case, to that of the single ^{31}P chemical shift observed in DMSO-d_6 solution, where both phosphonic acid groups are equivalent on the NMR timescale. The solid-state chemical shift value of 25.3 ppm does indeed correlate well with the chemical shift measured in DMSO-d_6 of 25.2 ppm, and confirms the non-hydrogen-bonded nature of the phosphonic acid groups in DMSO-d_6.

Similarly, the nature of the calcium dihydrate salt of HEDP, $CaH_2L{\cdot}2H_2O$, was investigated in both DMSO-d_6 and D_2O. $CaH_2L{\cdot}2H_2O$ is only sparingly soluble in both solvents, and therefore it was not possible to obtain ^{13}C NMR data. The NMR data that were obtained, as well as the coupling constants, can be found in Table 3-2. In this case the PO**H** and CO**H** protons were observed in D_2O for the

complex, indicating that their rate of proton exchange relative to the free-acid form of HEDP has changed sufficiently to be observed; this shows that this complex can be observed in the aqueous solution by means of solution NMR. Low solubility could account for the fact the PO**H** signals were not observed in DMSO-d_6. One would have hoped also to see a Ca-O**H$_2$** signal, but rapid D_2O exchange is probably the cause for it not having been observed. A similar change in the position of the ^{31}P chemical shift occurs for the $CaH_2L{\cdot}2H_2O$ complex as occurred with HEDP when moving from DMSO-d_6 to D_2O as solvent.

Table 3-2. ^{1}H, ^{13}C, ^{31}P NMR shift (δ) and coupling constant (J) data for $CaH_2L{\cdot}2H_2O$ measured in DMSO-d_6 and D_2O as solvent

$CaH_2L{\cdot}2H_2O$	DMSO-d_6		D_2O	
	δ (ppm)	J (Hz)	δ (ppm)	J (Hz)
PO**H**	-	-	8.4 (b)	-
CO**H**	1.2 (s)	-	2.0 (s)	-
C**H$_3$**	1.4 (t)	$^{3}J_{H,P}$ = 15.8	1.5 (t)	$^{3}J_{H,P}$ = 15.2
O**H$_2$**	3.7 (b)	-	-	-
P	25.2 (t)	-	21.7 (t)	-

3.2.2 pH-dependent ^{31}P and ^{23}Na NMR spectroscopy

The ^{31}P NMR data were collected for the solution series, prepared as described in Section 2.2, and the interaction of the Na^+(aq) ion was monitored by means of ^{23}Na NMR spectroscopy. The ^{23}Na chemical shift changed by only 0.9 ppm over the whole pH range. This shift is attributed to the increase in the solution's ionic strength as pH increases (due to the formation of highly charged species) rather than to the formation of hydroxo complexes, which form only above a pH value of 13.00 [4], or as a result of an interaction with HEDP.

Figure 3-1 shows the trend observed for the ^{31}P shift over the pH range. Obtaining the second derivative of this curve gives approximate values of the dissociation constants, pK_a, of the various protonated forms of HEDP, except for the H_4L/H_3L^- and H_3L^-/H_2L^{2-} which cannot be resolved by the NMR data. However, an average value was determined for the $H_4L \leftrightarrows H_3L^- \leftrightarrows H_2L^{2-}$ equilibrium. The second derivative-determined values compared with those from

Table 1-1 can be found in Table 3-3, and from this table it can be seen that they are in good agreement. The first POH deprotonation of each phosphonate group seems to have a shielding on the phosphorus nucleus. The second POH deprotonation still shows a shielding effect relative to the fully protonated H_4L, but not as efficient as mono-deprotonation, as the ^{31}P signal shifts downfield again with an increase in pH.

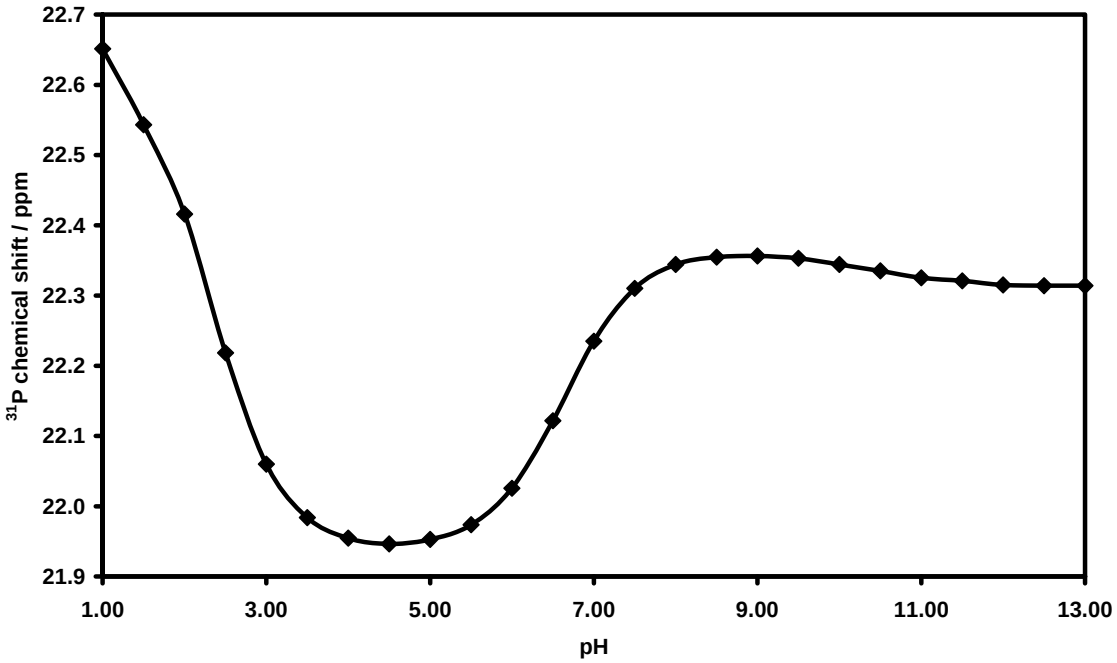

Figure 3-1. Variation in the ^{31}P chemical shift as a function of pH

Table 3-3. Comparison of reported pK_a values with pK_a values determined using the second derivative of the curve defined by the ^{31}P chemical shift as a function of pH for HEDP(aq)

Equilibrium reaction	pK_a †	pK_a ‡
$H_4L \leftrightarrows H_3L^- + H^+$	2.43	2.49
$H_3L^- \leftrightarrows H_2L^{2-} + H^+$	2.97	
$H_2L^{2-} \leftrightarrows HL^{3-} + H^+$	6.81	6.95
$HL^{3-} \leftrightarrows L^{4-} + H^+$	10.11	10.92

† From ref. [5]
‡ Determined from $f''(pH)$

3.3. Thermal gravimetric analysis

Figure 3-2 shows the first derivative curve of the weight percentage loss as a function of temperature, indicating that five major thermal events occur for HEDP upon heating.

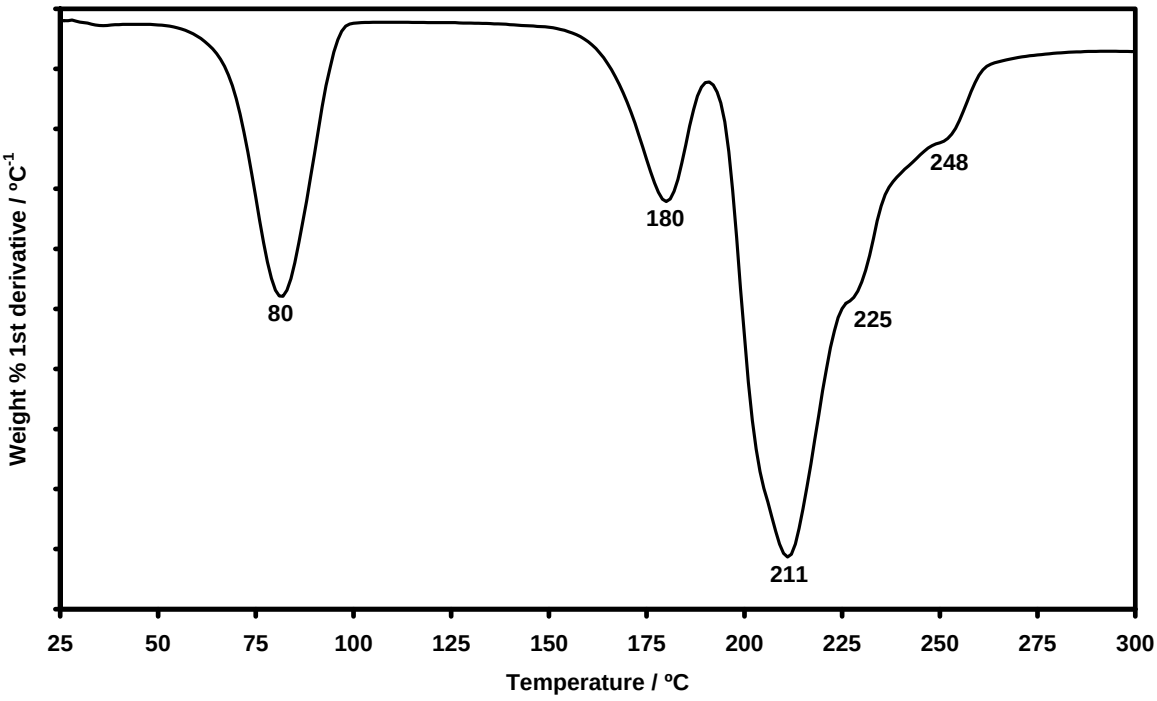

Figure 3-2. The first derivative curve of HEDP·H_2O for the temperature range 25 – 300 °C

The first event at 80 °C is the loss of the crystal water of hydration [6,7] and the second at 180 °C is the intermolecular loss of water to form a six-membered heterocyclic compound of which the derivative was isolated and a single crystal obtained [7]. The large bands at 211 °C and higher are reported to be phosphate and phosphate degradation products as a result of the breaking of the C-P bonds [6]. From this thermal gravimetric analysis the working temperature of 120 °C was chosen for anhydrous HEDP as this is above the dehydration temperature and would ensure that no surface-adsorbed water would be present as well.

3.4 X-ray diffraction methods

3.4.1 HEDP·H_2O

Uchtman and Gloss [8] were the first to report the single-crystal X-ray structure of HEDP in 1972, having an *R* value of 5.1%, but they were unable to determine accurately the hydrogen positions during this study. This is not unusual for bisphosphonate crystal structures [9]. Silvestre *et al*. [10] subsequently determined an accurate structure for HEDP·H_2O using neutron diffraction and reported this structure, as well as the hydrogen positions which they obtained by X-ray diffraction methods. Table 3-4 contains a summary of the crystallographic data as determined for the crystal structure. All other relevant data, bond lengths, bond angles and dihedral angles can be found in Table A-1 in the Appendix.

As a single molecular unit, HEDP (as H_4L) can have at most C_s as its highest point group symmetry. In the solid state, it adopts a C_1 conformation due to the very strong hydrogen bonding that occurs in the crystal structure [10]. This occurs in all other published structures containing any of the H_3L^-, H_2L^{2-}, HL^{3-} or L^{4-} forms of HEDP [9]. The molecular unit can be seen in Figure 3-3. Hydrogen bonding dominates the crystal lattice of HEDP·H_2O. The H_4L units generate a hydrogen-bonded network of two stacked two-dimensional staggered layers parallel to the *ac*-plane in the direction of the *b*-axis. These staggered H_4L layers are held together by a hydrogen-bonded layer of water molecules also parallel to the *ac*-face to complete the structure, as can be seen in Figure 3-4.

Table 3-4. Selected X-ray crystallographic data obtained for HEDP·H_2O

Empirical formula	$C_2 H_{10} O_8 P_2$	
Formula weight	224.04	
Crystal system	Monoclinic	
Space group	$P2_1/c$	
Unit cell dimensions	a = 6.9878(7) Å	α = 90º
	b = 17.5810(18) Å	β = 108.451(2)º
	c = 7.1140(8) Å	γ = 90º
Volume	829.05(15) Å^3	
Z	4	
Density (calculated)	1.795 g.cm^{-3}	
Final R indices ($I > 2\sigma(I)$)	R_1 = 0.0317, R_{w2} = 0.0844	
R indices (all data)	R_1 = 0.0319, R_{w2} = 0.0846	

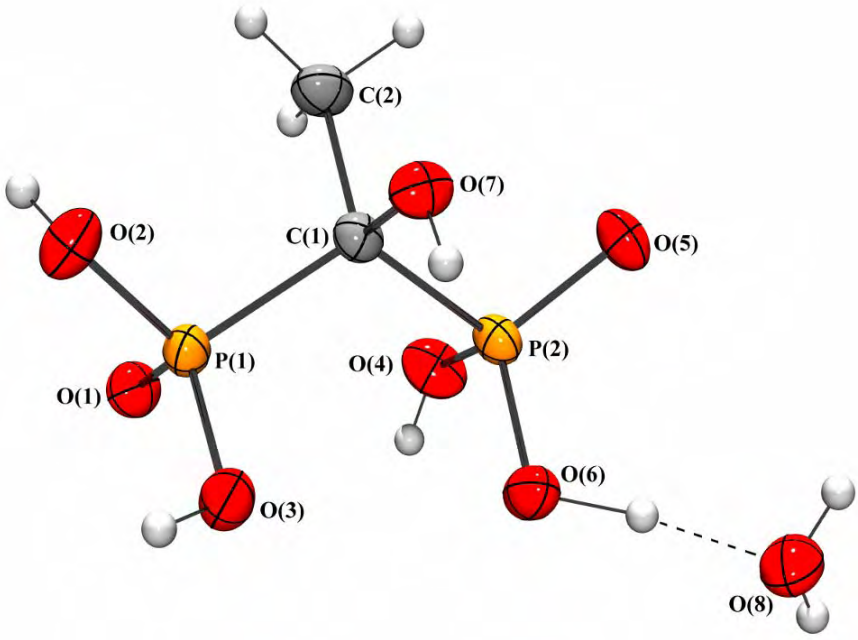

Figure 3-3. An Ortep/POV-ray drawing of the asymmetrical and molecular units of HEDP·H_2O. Ellipsoids are shown at the 50% probability level

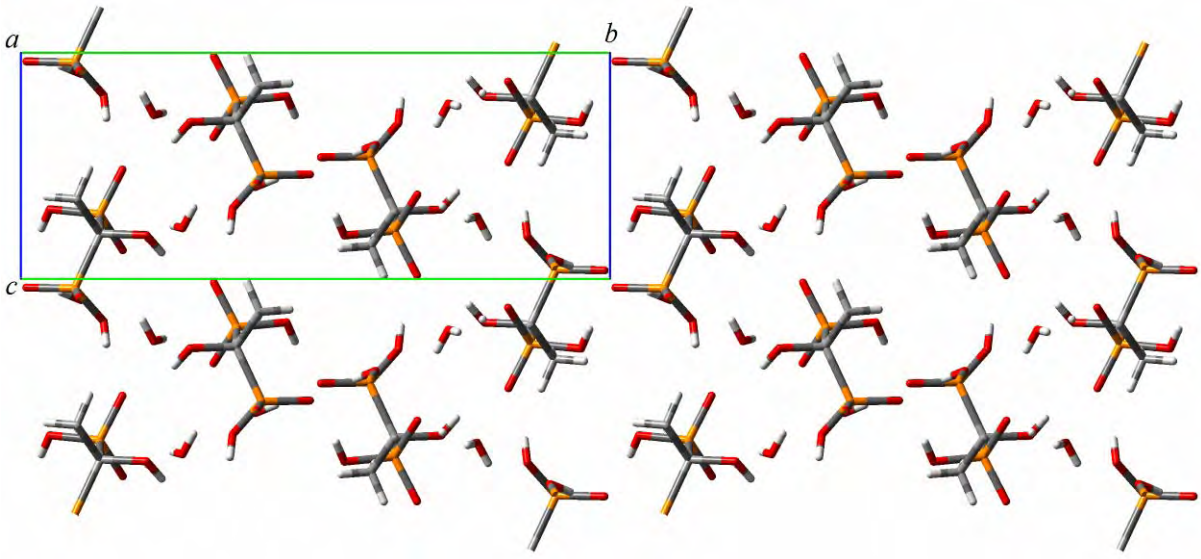

Figure 3-4. Expanded crystal lattice of HEDP·H_2O viewed along the *a*-axis

Table 3-5 lists notable hydrogen bond distances for HEDP as determined by X-ray diffraction in comparison with those determined by neutron diffraction methods [10]. Standard deviations are not included for ease of comparison, but can be found in Table A-1 in the Appendix. All standard deviations for values given in Table 3-5 range from 0.002 – 0.004 Å. The superiority of neutron over X-ray diffraction where hydrogen atoms are involved can be seen in the differences between the two sets of data, such as $d_{D–H}$, $d_{H\cdots A}$ and D$\hat{H}$A, but the accuracy of the X-ray data is obvious from the good agreement that exists for the two sets of data for the non-hydrogen atoms, such as $d_{D\cdots A}$ in Table 3-5 and the unit cell dimensions compared in Table 3-6.

The most notable hydrogen bond is the one that exists between H_2O and HEDP at P2-O6-H6···O8 where $d_{H6\cdots O8}$ = 1.40(4) Å (bold row in Table 3-5), making 06-H6 the longest PO-H bond in the HEDP molecule with $d_{O6\cdots H6}$ = 1.04(4) Å, compared with an average of 0.76 Å for the other PO-H bonds. In later sections it will be seen that the removal of crystal water is of significance in both the structural and spectral aspects of HEDP. The $d_{D–H}$ values differ the most between the X-ray and neutron data. This is due to the inherent difficulty of determining hydrogen bond distances accurately and is also reflected in the larger e.s.d values as seen in Table A-1.3 of the Appendix.

Table 3-5. Hydrogen bond data for HEDP·H_2O: X-ray (X) vs. neutron (N) data [10]

D-H…A	$d_{D–H}$ (Å)		$d_{H\cdots A}$ (Å)		$d_{D\cdots A}$ (Å)		DĤA (º)	
	X	N	X	N	X	N	X	N
O2-H2···O1*	0.77	1.003	1.84	1.604	2.615	2.604	177	176.4
O3-H3···O5**	0.77	1.046	1.72	1.437	2.483	2.476	169	172.7
O4-H4···O1***	0.73	0.999	1.90	1.622	2.623	2.617	170	174.0
O6-H6···O8	**1.04**	**1.121**	**1.40**	**1.317**	**2.435**	**2.437**	**173**	**175.8**
O7-H7···O5#	0.79	0.974	1.94	1.771	2.699	2.687	162	154.8
$O8\text{-}H8_A\cdots O7^{\#\#}$	0.76	0.984	1.95	1.737	2.696	2.697	166	164.5
$O8\text{-}H8_B\cdots O6^{\#\#\#}$	0.73	0.955	2.20	1.974	2.899	2.888	160	159.5

Symmetry transformations used to generate equivalent positions:
*: $-x, -y + 1, -z + 1$ **: $x, y, z + 1$ ***: $-x + 1, -y + 1, -z + 1$
#: $x, -y + 1.5, z + 0.5$ ##: $x + 1, y, z$ ###: $x, -y + 0.5, z - 0.5$

Table 3-6. HEDP·H_2O $P2_1/c$ unit cell comparison: X-ray vs. neutron data [10]

	X-ray	Neutron		X-ray	Neutron
a	6.9878(7) Å	6.983(9) Å	β	108.451(2)º	108.5(1)º
b	17.5810(18) Å	17.556(3) Å	V	829.05(15) $Å^3$	826.4 $Å^3$
c	7.1140(8) Å	7.109(9) Å	ρ	1.795 $g.cm^{-3}$	1.80 $g.cm^{-3}$

The O1=P1···P2=O5 dihedral is measured as 127.62º. As previously reported [10], when the C2-C1-P2-O5 dihedral is turned by ~120º such that the O1=P1···P2=O5 dihedral approximates 0º, one obtains a conformation (ignoring minor differences in the OH orientations) having C_s point group symmetry (Figure 3-5). It is also interesting to note that even though intermolecular hydrogen bonding dominates the structure, there is no hydrogen bonding between two water molecules or any significant intramolecular hydrogen bonding in HEDP.

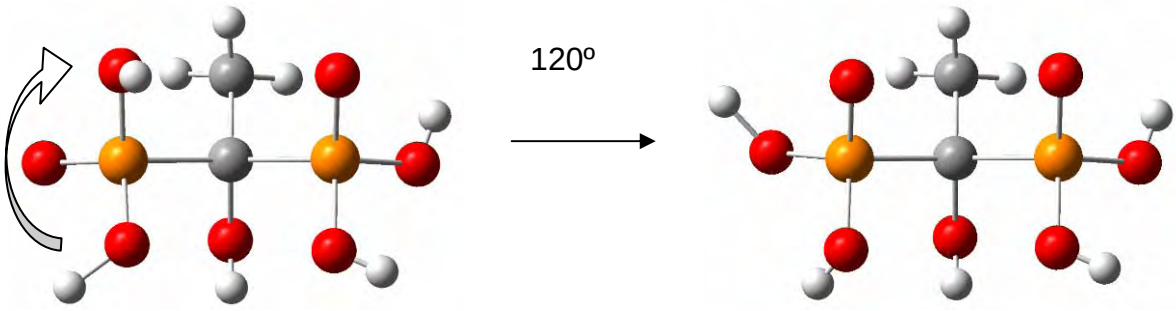

Figure 3-5. The HEDP can obtain pseudo C_s symmetry by rotation of one of the PO_3H_2 groups by ~120º

3.4.2 HEDP

Extensive attempts were made to obtain a single crystal of the anhydrous form of HEDP, but these were unsuccessful. Thus powder X-ray diffraction methods in conjunction with Rietveld analysis were employed to solve the structure. This has very successfully been done for organic molecular crystals having different phase transformations [11], including another bisphosphonate of importance to the pharmaceutical industry, namely risedronic acid (Figure 1-1E), that can have more than one hydrated state [12]. Figure 3-6 shows the powder X-ray diffraction patterns of HEDP·H_2O in comparison with the anhydrous HEDP to illustrate the definite structural rearrangement that occurs as one goes from the monohydrate to the anhydrous HEDP form.

TOPAS Academic [13] was used to index the unknown anhydrous HEDP powder pattern but, prior to this, two indexing sets with different cut-off criteria regarding reflection intensity (after normalisation) were performed on the known structure of HEDP·H_2O to validate the results and determine that the indexing could be accepted with confidence for the anhydrous HEDP. The two sets were: all reflections with an intensity above 10% (24 reflections) and all reflections above 15% (13 reflections) for the 2θ range 5 – 60º. Each indexing gave a ranked list of possible unit cell solutions, of which the top ten for both HEDP·H_2O (compared with its known structure) and HEDP can be found in Table 3-7 and Table 3-8 respectively. Indexing done using the 24-reflection set gave the most acceptable

results when compared with the experimental data for HEDP·H_2O. It is important to note that even though the correct space group for HEDP·H_2O is listed only as the third solution in Table 3-7, eight of the ten possible solutions' cell parameters correlate extremely well with the experimentally determined cell parameters of HEDP·H_2O.

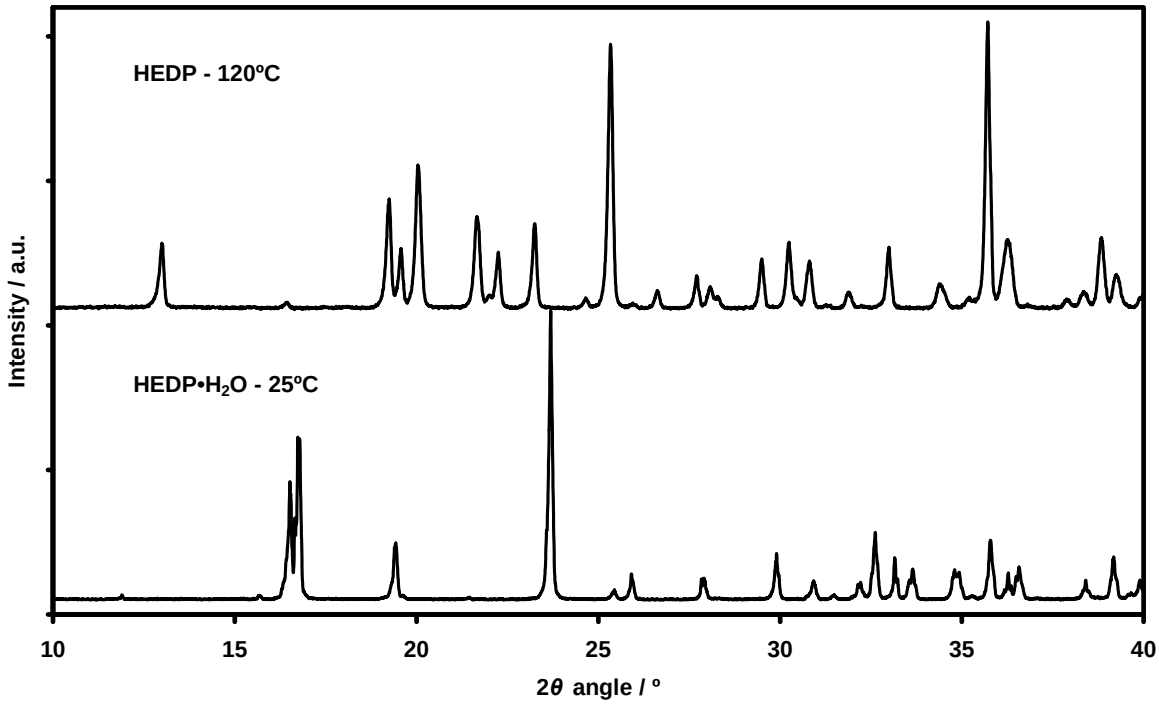

Figure 3-6. Powder XRD patterns of HEDP·H_2O and anhydrous HEDP showing that there is a structural difference between the two crystalline compounds

Table 3-7. The ten most probable index solutions (in Å and º) found for HEDP·H_2O compared with the experimental data displayed in bold at the top

Space Group HEDP·H_2O	Cell Volume	a	b	c	α	β	γ
$P2_1/c$	***829.05***	***6.9878***	***17.5810***	***7.1140***	***90***	***108.451***	***90***
$P2_1$	831.485	6.9987	17.5823	7.1238	90	108.462	90
$P2_1$	831.853	6.9988	17.5873	7.1246	90	108.458	90
$P2_1/c$	831.853	6.9988	17.5873	7.1246	90	108.458	90
$P2_1/c$	831.485	6.9987	17.5823	7.1238	90	108.462	90
$P2$	831.485	6.9987	17.5823	7.1238	90	108.462	90
$P2$	831.853	6.9988	17.5873	7.1246	90	108.458	90
~~$P2_1$~~	~~832.338~~	~~7.0000~~	~~17.5896~~	~~8.2586~~	~~90~~	~~125.061~~	~~90~~
Pc	831.853	6.9988	17.5873	7.1246	90	108.458	90
~~$P2_1/e$~~	~~832.338~~	~~7.0000~~	~~17.5896~~	~~8.2586~~	~~90~~	~~125.061~~	~~90~~
Pc	831.485	6.9987	17.5823	7.1238	90	108.462	90

Table 3-8. The ten most probable index solutions (in Å and º) found for HEDP

Space Group HEDP	Cell Volume	a	b	c	α	β	γ
$P2_1$	710.127	5.3981	10.3817	13.0550	90	103.925	90
$P2_1$	710.068	5.3980	10.3817	13.0542	90	103.923	90
$P2$	710.127	5.3981	10.3817	13.0550	90	103.925	90
$P2_1$	710.396	5.3992	10.3824	12.8720	90	100.089	90
~~$P2_1$~~	~~710.124~~	~~5.3981~~	~~10.3817~~	~~15.2804~~	~~90~~	~~123.978~~	~~90~~
$P2_1$	710.054	5.3979	10.3816	12.8701	90	100.100	90
$P2$	710.068	5.3980	10.3817	13.0542	90	103.923	90
$P2$	710.396	5.3992	10.3824	12.8720	90	100.089	90
~~$P2$~~	~~710.124~~	~~5.3981~~	~~10.3817~~	~~15.2804~~	~~90~~	~~123.978~~	~~90~~
$P2$	710.054	5.3979	10.3816	12.8701	90	100.100	90

The results for HEDP give four possible solutions based on the cell parameters. All solutions have the initial cell parameters: a = 5.398 Å, b = 10.382 Å, c = 12.962 Å combined with β = 100.10º or 103.92º in space group $P2_1$ or $P2$.

The two possibilities struck through in Table 3-8 were heuristically deemed to be less possible when compared with the other solutions.

A single water molecule has a calculated van der Waals' volume of ~17.5 Å^3 [14], resulting in the four water molecules in the HEDP·H_2O unit cell having a combined volume of 70 Å^3. Subtracting this from the experimentally determined cell volume of 829.05 Å^3 of HEDP·H_2O gives the volume of all H_4L units as 759.05 Å^3. Comparison of this value with that obtained for anhydrous HEDP of ~710 Å^3 from the indexing procedure shows that it would be valid to assume that four HEDP units are present within the unit cell of anhydrous HEDP. This implies that the asymmetrical unit should consist of two non-equivalent HEDP molecules as both $P2_1$ and $P2$ have Z = 2. The difference between the two calculated cell volumes containing only H_4L can be rationalised as resulting from the different packing geometry existing in the different cell structures in the anhydrous and monohydrate forms of HEDP and even as an 'interaction volume' between the water and H_4L molecules in the monohydrate case, which is not quantified here.

Both the Pawley and Le Bail powder XRD curve-fitting algorithms gave refinements, with an R_{wp} (mathematically defined in Eq. 1.22) between 6.44 and 7.44% for all space group and cell parameter combinations as stipulated earlier. It was therefore decided to continue with all four for the indicated structure determination as it was difficult to decide with confidence at this stage which unit cell parameter combination was the most likely.

A pseudo-Voigt function was selected to model the peak and background profiles of the experimental powder pattern as it approximates the Voigt function, which is a weighted summation of Gaussian and Lorentzian functions, adequately enough [15]. In the pseudo-Voigt case the width at half-maximum (FWHM) values for the Gaussian and Lorentzian functions are kept the same. All pseudo-Voigt variables and lattice parameters were further refined during the Pawley and Le Bail fittings and used as such to determine the rigid body structure.

The rigid body used in the structure refinement was generated from the single-crystal structure of HEDP·H_2O. Figure 3-7 shows the calculated,

experimental and difference XRD patterns for the four combinations of the cell parameters as obtained using the rigid body. Comparison of the indices of agreement R_{wp}, R_B and goodness of fit (GOF) in Table 3-9 for the $P2$ and $P2_1$ space groups shows that $P2_1$ is clearly the more plausible choice for the space group as the difference between the two sets is ~10% and the two most intense reflections experimentally obtained could not be adequately modelled in space group $P2$ (Figure 3-7). Unfortunately, no decision could yet be made on the β-angle value as the indices of agreement differ by less than 1% within the same space group. One reason could be that the low d-spacing values used during the initial indexing process could have introduced an error due to them being less accurate. Re-indexing was therefore attempted for d-spacing values greater than 2.5 Å, assuming that all lattice parameters are at least greater than 3 Å [16]. This resulted in a lowering of the space group symmetry, giving the cell as triclinic $P\bar{1}$ with a = 5.399 Å, b = 10.385 Å, c = 12.876 Å, α = 89.96º, β = 100.12º and γ = 90.02º. This correlates extremely well with the previously determined systems, and hinted at the β-angle being ~100.1º with $\alpha = \gamma$ = 90º. With $\alpha = \gamma$ = 90º, the $P\bar{1}$ space group transforms to $P2_1$.

An iterative refinement process was now followed using the rigid body for this unit cell, in which the cell parameters and rigid body positioning were alternately refined with each cycle until no further improvement in the indices of agreement was obtained. Figure 3-8 shows a perspective drawing of one filled unit cell obtained in this manner.

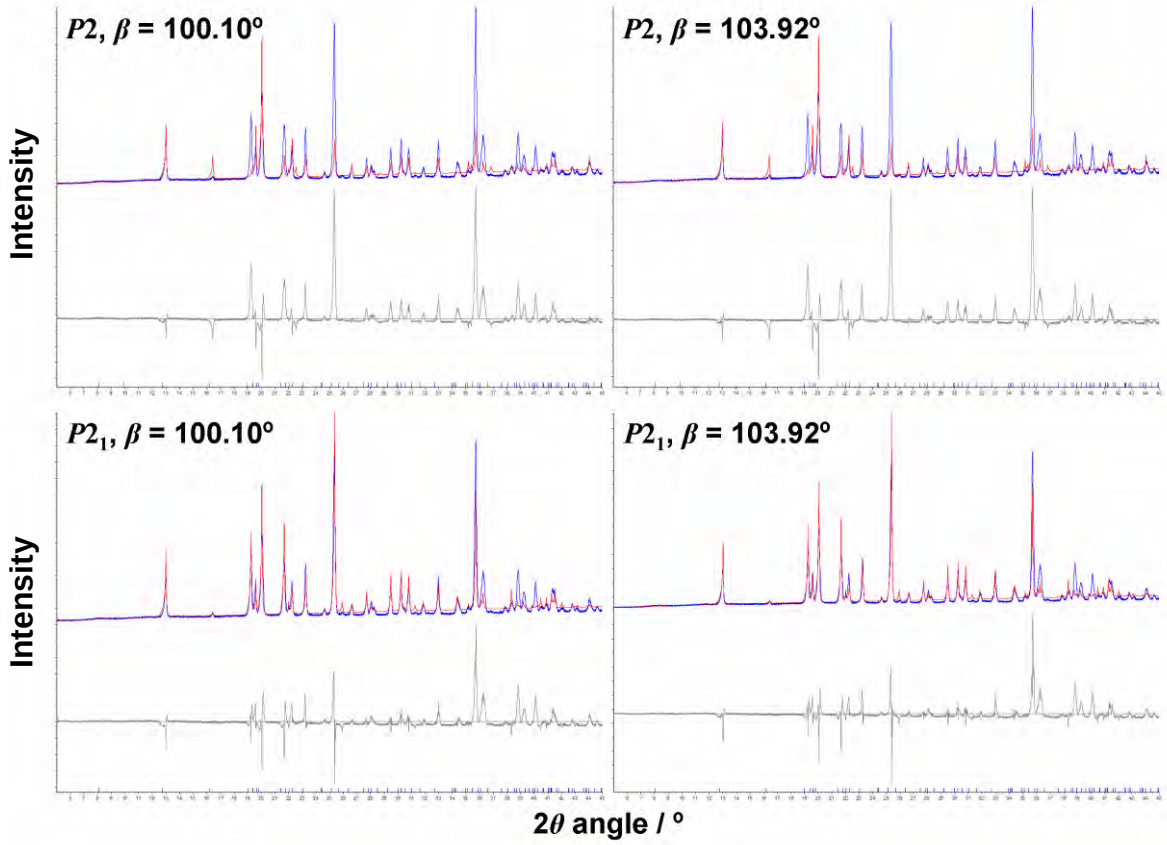

Figure 3-7. Difference (grey) powder X-ray diffraction spectra between the calculated (red) and experimental (blue) data for combinations of space groups and β-angles

Table 3-9. Values of R_{wp} (%), R_B (%) and GOF for the various space group and β-angle combinations

Space group	β-angle					
	100.10°			103.92°		
	R_{wp}	R_B	GOF	R_{wp}	R_B	GOF
$P2$	36.50	60.81	7.86	36.58	63.64	7.87
$P2_1$	25.72	51.28	5.54	26.32	50.92	5.65

As the lowest R_{wp} value obtained is still not acceptable at 25.72%, a re-refinement was done, including preferred orientation as a refinable parameter. This is justified by the fact that the sample was packed on the non-spinning Pt-heating strip using the top-loading technique, and thus during the thermal dehydration stage, the morphology of the sample can change (it is a platy material, new

crystallite formation/orientation, cracks in the powder surface, etc.) in such a way that preferred orientation is significantly present during measurement of the powder pattern. The preferred orientation was sufficiently modelled using an eight-order spherical harmonics function [17]. Table 3-10 displays the indices of agreement when preferred orientation is taken into account. Very importantly, during this second round of refinements the unit cell lengths and angles were also allowed to refine and the labels '100.1' and '103.92' for the β-angle serve only as labels from this point forward for comparison with Table 3-9.

Table 3-10. Values of R_{wp} (%), R_B (%) and GOF for the various space group and β-angle combinations with preferred orientation also refined

Space group	β-angle					
	100.10º			103.92º		
	R_{wp}	R_B	GOF	R_{wp}	R_B	GOF
$P2$	14.90	5.87	3.22	14.72	8.39	4.28
$P2_1$	11.10	3.40	2.39	13.37	4.88	2.88

All refinements dramatically improve the indices of agreement, but finally a single candidate can be identified as the most plausible solution to be optimised initially for the final refinement. The system was then again iteratively refined and the final structure solution using the rigid body was obtained as a = 5.407 Å, b = 10.387 Å, c = 12.887 Å and β = 100.071º in space group $P2_1$. Figure 3-8 shows the unit cell obtained for the final refinement; it can also be seen that the packing is chemically acceptable.

The final refinement, was done by removing the rigid body constraint and allowing all atoms to be able to move around independently from their original positions. When the final atomic positions were obtained, preferred orientation was introduced into the model for the last iteration of the final refinement. This was done as including preferred orientation initially in the final refinement could introduce systematic errors. The final structure obtained was still recognisable as HEDP, but slightly distorted. The difference XRD pattern between the experimental and calculated patterns is shown in Figure 3-9. The final indices of agreement were R_{wp} = 8.01%, R_B = 1.15% and GOF = 1.73.

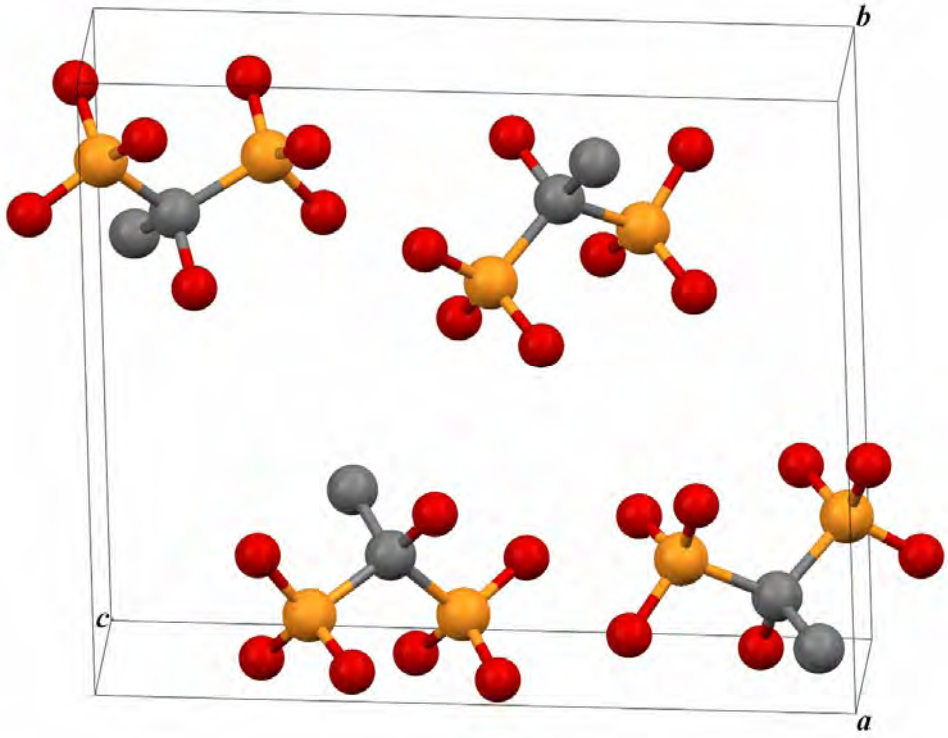

Figure 3-8. The unit cell packing obtained during the rigid body refinement for the unit cell $P2_1$ with β = 100.071°

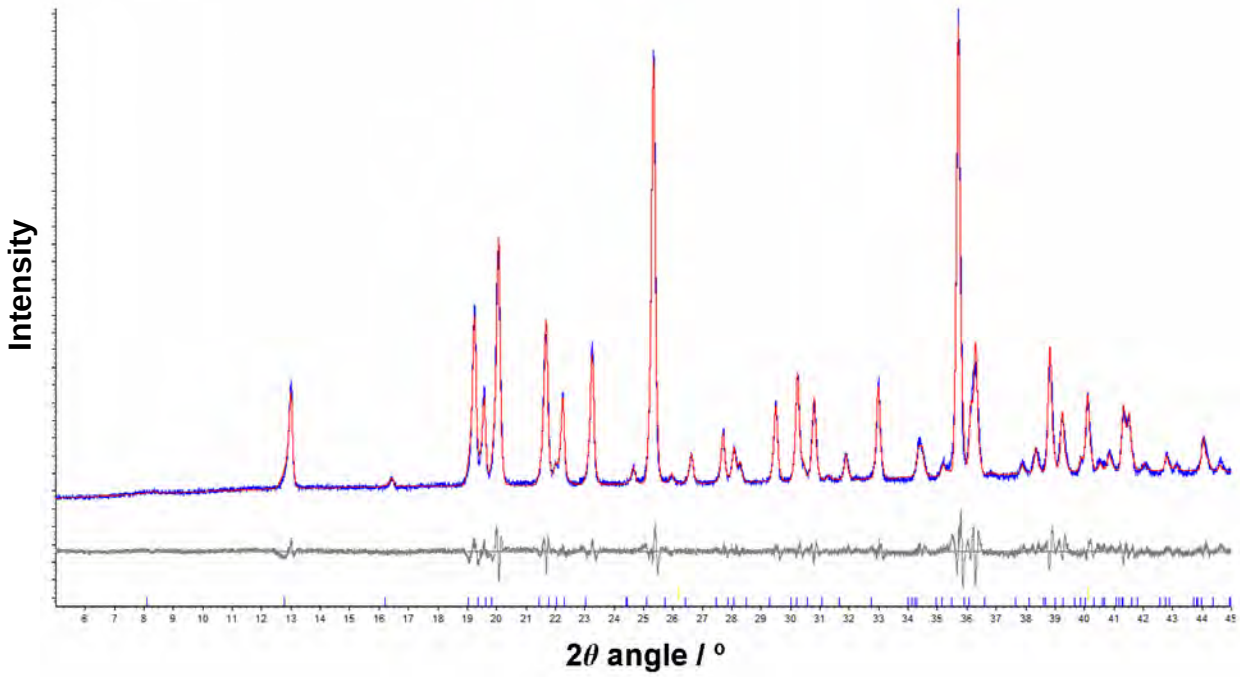

Figure 3-9. Difference (grey) powder X-ray diffraction spectra between the calculated (red) and experimental (blue) data for the final refinement of the structure

Figure 3-10 shows an overlay of the rigid body structure obtained with that finally obtained when the rigid body constraint was removed. The distorted nature required to model and obtain the best fit of the experimental powder pattern is highly probable due to the initial sampling methods. Data were not collected in a capillary set-up, which is ideally required to ensure that the intensity data are accurate. This facility was not available at the time the measurement was made. The data were collected on a Pt-heating strip: powder was placed on the strip and heated to the required temperature to remove the water of crystallisation and maintain the anhydrous form of HEDP during the measurement. During this dehydration process the powdered crystallites orientated themselves such that the preferred orientation of the crystallites contributed significantly to the intensity data, as seen from the comparison of the indices of agreement in Tables 3-9 and 3-10 before and after preferred orientation was included in the modelled system.

All these and other previously mentioned factors could also have contributed to the initial ambiguities of the cell parameters. This is also evidenced by the fact that one unit cell parameter became the most plausible solution after preferred orientation was taken into account. The positions of only the non-hydrogen atoms could be determined with a level of confidence. It would also have been advantageous to have been able to determine the hydrogen positions as this would have given more insight into the nature of hydrogen bonding for this molecule, specifically in the anhydrous solid state. Experimental determination of the hydrogen positions will definitely not be possible here as it is already difficult to determine them experimentally with good-quality X-ray data because twelve H atoms have approximately the same scattering contribution as one C atom. Ideally, to obtain hydrogen positions, high resolution neutron diffraction data of the deuterated analog could provide this answer.

Despite all the difficulties encountered, it seems that an acceptable determination of the crystal structure of anhydrous HEDP has been done. One aspect of the rigid body that was assumed, but that may not necessarily be true for anhydrous HEDP, is the orientation of the two PO_3H_2 moieties relative to each other. In HEDP·H_2O the PO_3 atoms of the two moieties, for all practical purposes, eclipse one another when one looks down the P1-P2 axis (Figure 3-11). From

the distorted structure obtained it would seem that this may not be the case as the two distorted PO_3 units seem to prefer a staggered conformation. In summary, Table 3-11 contains the X-ray crystallographic data as obtained from the Rietveld refinement for the rigid body structure, as well as the final distorted structure.

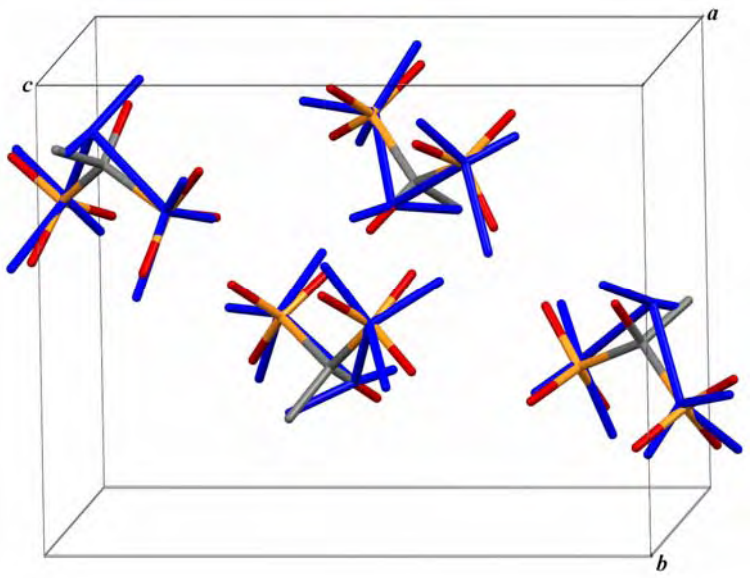

Figure 3-10. Unit cell packing of the rigid body structure superimposed on that of the atom-independent determined structure (blue)

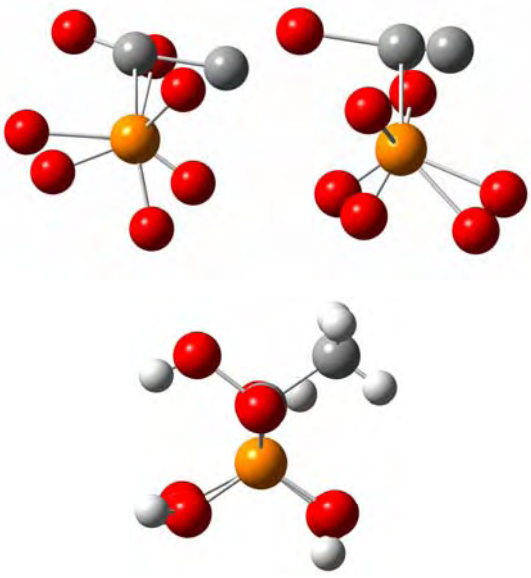

Figure 3-11. HEDP molecules viewed down the P1-P2 axis showing the two staggered (albeit distorted) H_4L units as determined by Rietveld refinement for the anhydrous case (top) compared with the eclipsed conformation in $HEDP{\cdot}H_2O$ (bottom)

Table 3-11. Crystallographic summary of the rigid body and independent atom determined structures of anhydrous HEDP

	Rigid body	Independent atom
Space group	$P2_1$	$P2_1$
a / Å	5.407	5.406
b / Å	10.387	10.285
c / Å	12.887	12.887
β / °	100.071	100.070
Z	2	2
R_{wp}	11.01%	8.01%
R_B	3.40%	1.15%
GOF	2.39%	1.73%

3.4.3 $CaH_2L{\cdot}2H_2O$

A first attempt at the single crystal structure determination for $CaH_2L{\cdot}2H_2O$ was done by Uchtman [18] but, similarly to $HEDP{\cdot}H_2O$, the hydrogen positions could not be experimentally determined. Since it was obvious from the literature [9] and during the structural investigation for anhydrous and monohydrated HEDP that hydrogen bonding plays such an important role in the chemistry and inter/intramolecular interaction of HEDP, a redetermination of the crystal structure was attempted and most of the hydrogen positions were successfully determined experimentally. Table 3-12 contains a summary of the crystallographic data as determined for the crystal structure. All other relevant data, bond lengths, bond angles and dihedral angles can be found in Table 1-B in the Appendix.

Figure 3-12A shows the molecular structure of $CaH_2L{\cdot}2H_2O$, as well as four other Ca-coordinated oxygen atoms. Similar to fully protonated HEDP, H_4L, the bisphosphonate molecule H_2L^{2-} can have C_s as its highest point group symmetry, but again adopts a C_1 conformation due to the hydrogen bonding stabilising the lattice. Calcium is eight-coordinated in this structure, with Ca-O bond lengths ranging between 2.3578(17) and 2.5921(18) Å (an average of 2.475 Å), which is

comparable to the average Ca-O bond length of 2.41 Å in calcium oxide at 298 K [19].

Table 3-12. Selected X-ray crystallographic data obtained for $CaH_2L \cdot 2H_2O$

Empirical formula	$C_2\ H_{10}\ Ca\ O_9\ P_2$	
Formula weight	280.12	
Crystal system	Triclinic	
Space group	$P\bar{1}$	
Unit cell dimensions	a = 6.9499(6) Å	α = 92.7330(10)º
	b = 7.5961(6) Å	β = 106.3140(10)º
	c = 9.7000(8) Å	γ = 112.4250(10)º
Volume	447.33(6) Å^3	
Z	2	
Density (calculated)	2.080 g.cm^{-3}	
Final R indices ($I > 2\sigma(I)$)	R_1 = 0.0339, R_{w2} = 0.0942	
R indices (all data)	R_1 = 0.0344, R_{w2} = 0.0947	

Parallel to the ab-face of the unit cell, a network of infinite two-dimensional layers is formed, and each layer is linked via bridging coordination of the Ca atoms with the O8 atom of the water molecules, as well as the H_2L^{2-} molecular unit; other extensive intermolecular hydrogen bonding also occurs. Two symmetry-related H_2L^{2-} units bridge pairs of Ca atoms, with each Ca atom forming a six-membered chelate ring by bonding through the O1 and O4 oxygen atoms of one of the H_2L^{2-} units, and forming a five-membered ring with the other H_2L^{2-} unit by bonding with its O2 and O7 oxygen atoms. The Ca···Ca pair distance is 5.4237(10) Å. Two four-membered rings, $(Ca1\text{-}O2)_2$ and $(Ca1\text{-}O8)_2$, are also formed when two symmetry-related O2 H_2L^{2-} atoms and two symmetry-related O8 water oxygen atoms form coordination bridges to other Ca atoms, resulting in Ca···Ca distances of 3.7907(9) Å and 4.1334(9) Å for the O2- and O8-four-membered rings respectively. This results in each Ca atom being linked by coordination bridges to three other Ca atoms, forming the previously mentioned infinite

two-dimensional network layers. All these rings discussed are shown for clarity in Figure 3-12B. At this point it should be noted that the proton on O6 is equally disordered between O5 and O6, and these network layers are linked via hydrogen bonds between O5-H5···O5*, O6-H6···O6** and O9-H9$_b$···O6$^{\#\#}$, where the symmetry transformations are *: $-x + 1, -y + 1, z$, **: $-z + 1, -x + 1, -y + 2, -z + 1$ and ##: $x, y, z - 1$ respectively. Due to the disorder of the O6 proton, it is presumed that one hydrogen bond is formed for each O$_n$-H$_n$ (n = 5, 6) link, where one O atom is protonated (acting as the donor) and the other unprotonated (acting as the acceptor).

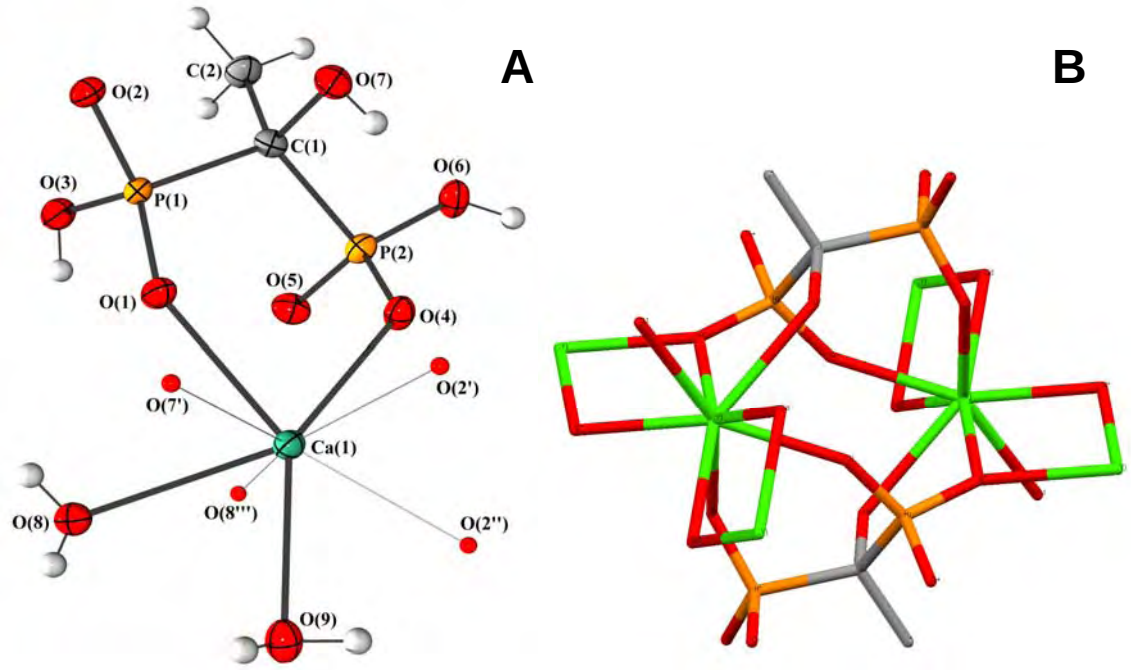

Figure 3-12. A. An Ortep/POV-ray drawing of the molecular unit of $CaH_2L{\cdot}2H_2O$ showing the eight-coordinate nature of the calcium atom. Ellipsoids are shown at the 50% probability level and the symmetry transformations used to generate the equivalent positions are ': $-x, -y + 1, -z$; '': $x + 1, y, z$; ''': $-x + 1, -y + 2, -z$ B. Capped stick representation of the partial crystal structure of $CaH_2L{\cdot}2H_2O$ showing the four, five and six membered formed in the crystal structure as discussed in the text.

3.5 Vibrational spectroscopy and molecular modelling

3.5.1 HEDP and its various protonated forms

3.5.1.1 Solid-state spectroscopy

As already discussed, HEDP has both a monohydrate and anhydrous phase in the solid state, and also has the various protonated forms, H_4L, H_3L^-, H_2L^{2-}, HL^{3-} and L^{4-}, that exist in an aqueous solution. Vibrational spectroscopy (and specifically Raman spectroscopy because of its versatility) is an ideal tool for investigating the structural changes that occur during the loss of hydration and solvation under different conditions. Figure 3-13 shows the Raman spectra of HEDP·H_2O and HEDP for the region 100 – 1600 cm^{-1} and Figure 3-14 shows the Raman spectra for the two compounds for the region 2600 – 3200 cm^{-1}. Due to the structural rearrangement, the most prominent changes in the Raman spectrum occur predominantly in the vibrational bands associated with the PO_3H_2 moieties and that associated with the water of hydration. Vibrational band assignments can be found in Table 3-13. Various sources (references [20-25]) were used to make the complete empirical assignment for HEDP·H_2O. Assignments for anhydrous HEDP were tentatively confirmed and refined by means of molecular modelling of a single H_4L unit conformer. Generation of this modelled conformer is discussed in more detail later on in this chapter under Section 3.5.1.2.

In the low wavenumber region, seen in Figure 3-13, the most notable changes are the appearance of a lattice mode at 168 cm^{-1} and the disappearance of the hydrogen bond band at 241 cm^{-1}. A weak band at 233 cm^{-1} in the spectrum of anhydrous HEDP is assigned to a similar hydrogen bond band, but should occur either inter- or intramolecularly between to H_4L units as this type of bonding was observed in both the $H_4L·H_2O$ and $CaH_2L·2H_2O$ cases . The band at 274 cm^{-1} of HEDP·H_2O is assigned to the ρPO-H / δC-C-O band as it seems that this band could be affected by a loss of hydration and is therefore not observed in the anhydrous HEDP spectrum. In general, bands will shift to a higher wavenumber

(if otherwise not dramatically affected by structural factors) as temperature increases. The shift of the ρPO-H band from 343 cm^{-1} to 327 cm^{-1} is indicative of structural change as the band shifts to a lower value rather than a higher one. The changes and 'simplification' of the band structure for the region 411 – 528 cm^{-1} are attributed specifically to the loss of hydration as all these bands are associated with the PO_3H_2 or COH groups. The ν^sC-P band at 627 cm^{-1} shifts to 632 cm^{-1} and does not seem to be affected by the structural rearrangement. It is known that this vibration is very likely to be mixed up with other vibrations [20] and it is also far removed from sites affected by the loss of hydration. The νC-CO band at 822 cm^{-1}, however, shifts lower and is also lower in intensity for anhydrous HEDP than HEDP·H_2O, and thus indicative of the rearrangement occurring during the dehydration process.

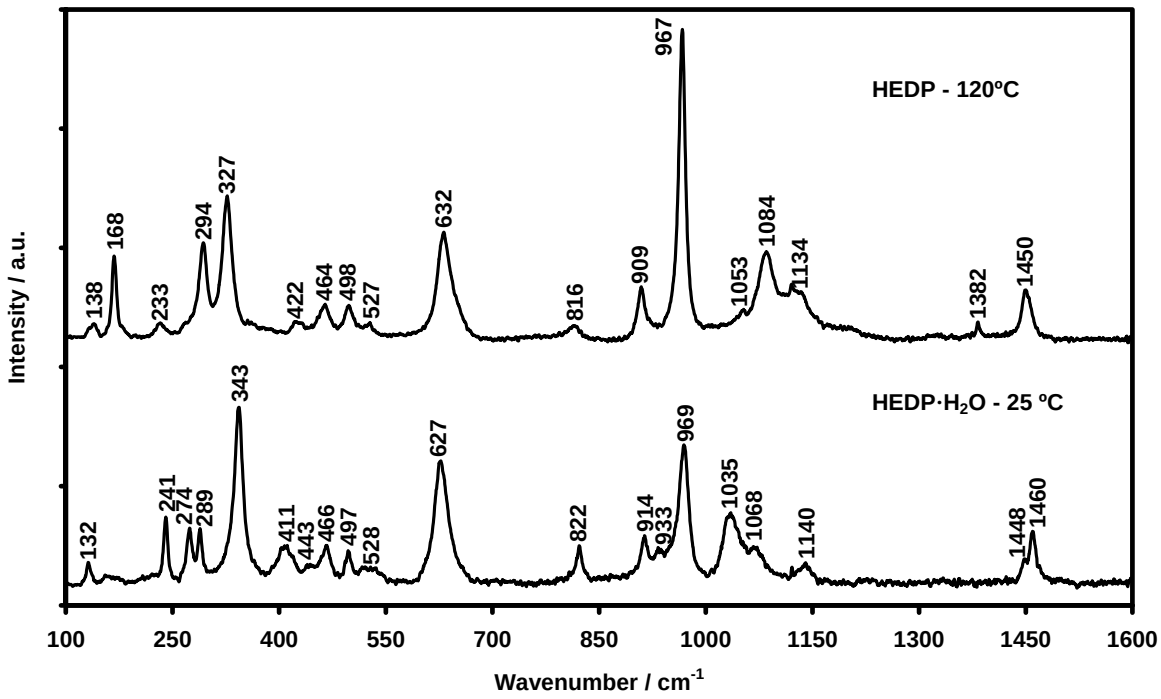

Figure 3-13. Raman spectra of HEDP·H_2O and anhydrous HEDP showing the bands mostly associated with vibrational bands involving non-hydrogen atoms

The bands found between 933 and 1140 cm^{-1} are assigned to stretching vibrations involving specifically the PO_3H_2 groups. Compounds containing P=O and P-OH groups have complex band structures in this region, making analysis

difficult [20]. Despite this limitation, it can still be seen that changes in relative intensities and band positions are indicative of the structural change. There is a notable increase in intensity of the strongest band at 969/967 cm^{-1}, assigned to the ν^{s}P-O(H) band, as the two PO_3H_2 moieties become chemically equivalent (but not necessarily symmetry equivalent) as water of hydration is lost. The well-described [20] δ^{as}C-CH_3 bands at 1448, 1460 and 1450 cm^{-1} are observed in both spectra, but in the anhydrous case the weak band at 1382 cm^{-1}, assigned to the δ^{s}C-CH_3, becomes Raman active and is a good indicator of the presence of a CCH_3 moiety [20].

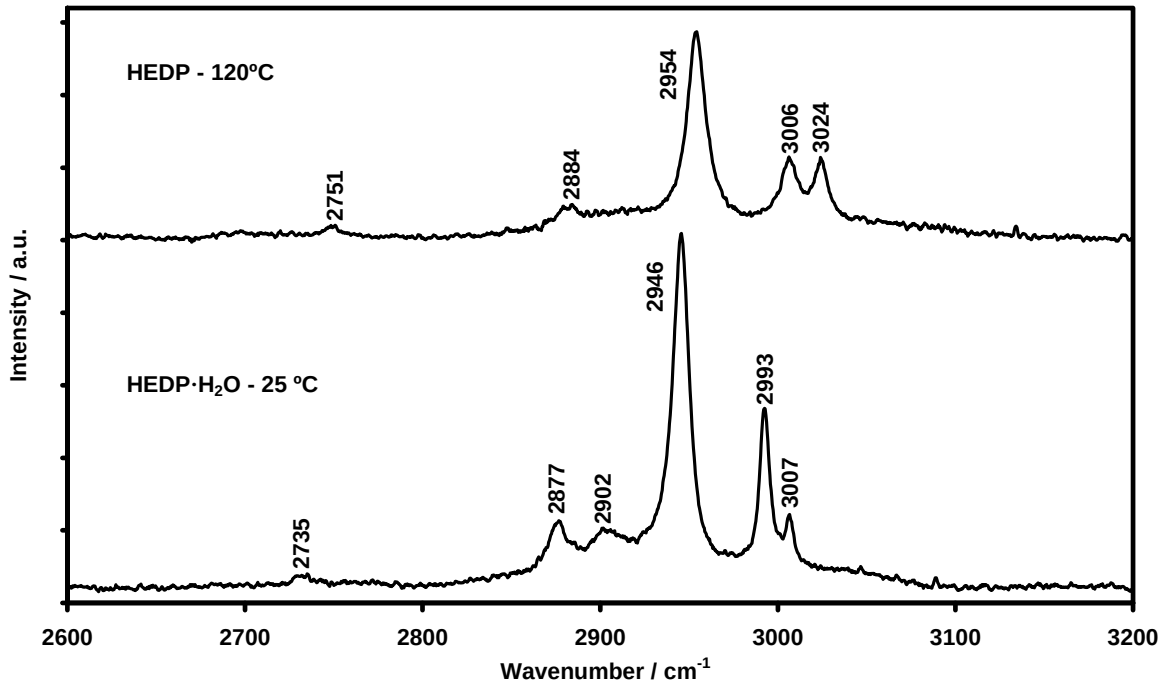

Figure 3-14. Raman spectra of HEDP·H_2O and anhydrous HEDP of the spectral region associated with the CH_3 and OH stretching bands

Only two notable differences are observed in the νCH/OH region of the Raman spectra. The band at 2902 cm^{-1}, assigned to the hydrogen-bonded νOH vibration, is not present in the anhydrous HEDP spectrum and the relative intensity of the two $\nu^{as}CH_3$ bands at 2993 and 3007 cm^{-1} change as one goes from the HEDP·H_2O to anhydrous HEDP, also probably due to structural effects.

Figure 3-15 shows the mid-infrared spectrum for HEDP·H_2O and anhydrous HEDP for the region 400 – 4000 cm^{-1}, and their assignments can be found in

Table 3-13. Similar rationales can be employed to explain changes in the vibrational bands observed, and only the most important spectral features will be discussed. Bands associated with the δOPO vibrations (<550 cm^{-1}) are observed to be more intense in the IR spectrum than in the Raman spectrum for both compounds, while the stretching vibrational bands associated with the PO_3H_2 moieties show a complex and overlapping band structure in the 900 – 1300 cm^{-1} region relative to the more well-defined, albeit still complex, structure of the same region in the Raman spectrum. The water-associated bands of HEDP·H_2O are broad and strong in intensity and, in conjunction with the broad bands usually associated with phosphonic acids [20], make analysis of the high-wavenumber region difficult. Bands indicated with an * in Figure 3-15 at 697, 1649, 3285 and 3483 cm^{-1} are assigned to the water of hydration [21, 25].

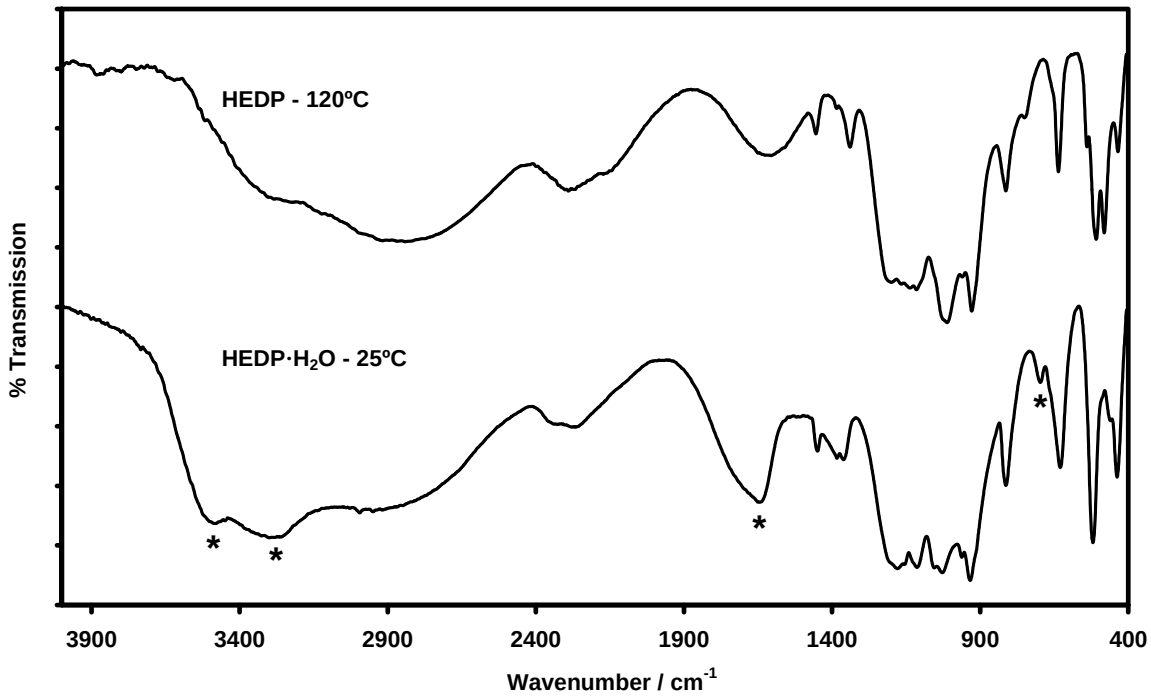

Figure 3-15. Mid-infrared spectrum of HEDP·H_2O and anhydrous HEDP prominently showing the bands associated with H_2O (marked *) disappearing during the loss of hydration

Table 3-13. The vibrational assignment of HEDP·H_2O and anhydrous HEDP

Assignment	HEDP·H_2O		HEDP	
	Infrared	Raman	Infrared	Raman
Lattice		132 w		138 w
Vibrations				168 m
Inter or intraHEDP				233 w
νOH···O				
νOH···OH_2		241 m		
ρPO-H / δCCO		274 m		
δC-C		289 m		294 m
ρPO-H		343 vs		327 s
ρCO-H		411 w		422 w
	438 m	443 w	435 m	
ρPO-H	461 w, sh	466 w		464 w
		497 w	481 s	498 w
	520 s	528 w	508 s	527 w
			540 m, sh	
ν^sC-P	620 m	627 s	636 m	632 s
H_2O libration	697 w			
-			750 m, sh	
νC-CO	813 m	822 w	813 m	816 vw
νC-O-H		914 w		909 w
ν^sP-O(H)	933 vs	933 w	929 vs	
	962 vs	969 s	960 s, sh	967 vs
			1011 vs	
	1028 vs		1023 vs, sh	
δPO-H / ν^{as}P-O(H)		1035 m		
				1053 vw, sh
	1055 vs, sh			
		1068 w		1084 m
	1114 vs		1115 s	
νP=O / δPOH		1140 vw	1137 s	1134 w, sh
	1155 vs, sh			
			1166 s, sh	
	1178 vs			
	1202 vs, sh		1200 s	
-	1362 m		1339 w	
δ^sC-CH_3	1384 m		1385 w, sh	1382 vw
δ^{as}C-CH_3	1449 m	1448 w,sh	1454 w	1450 w
		1460 m		
νO=P-OH			1607 m, br	
δH_2O	1649 s, br			
νO=P-OH			2171 m, sh	
	2279 m, br			
			2290 s, br	
	2328 m, sh			
νPO-H		2735 vw		2751 vw
νO=P-OH	2830 s, br		2842 s, br	
$\nu^s CH_3$		2877 m		2884 m

Assignment	HEDP·H_2O		HEDP	
	Infrared	Raman	Infrared	Raman
νOH_2		2902 m		
$\nu^{s}CH_3$	2950 w	2946 vs		2954 vs
$\nu^{as}CH_3$	2995 w	2993 s		3006 s
		3007 m		3024 m
νOH_2	3285 vs, br			
	3483 vs, br			

ν: stretch, δ: deformation, ρ: rock
s: symmetrical, as: anti-symmetrical
vw: very weak, w: weak, m: medium, s: strong, vs: very strong
sh: shoulder, br: broad

Interestingly, it has been noted that the relative intensities of the broad bands centred at approximately 2800, 2300 and 1600 cm^{-1} can be used to distinguish between $RP{=}O(OH)_2$ and $R_2P{=}O(OH)$ acids [20]. In the IR spectrum of compounds containing the $P{=}O(OH)_2$ moieties, the 1600 cm^{-1} band has the weakest intensity of the three bands, whereas it is the strongest band in compounds containing the $R_2P{=}O(OH)$ acid functionality. Comparison of the three bands' intensities in the IR spectrum obtained for anhydrous HEDP shows that the 1600 cm^{-1} band is of lowest intensity as is expected for HEDP which can be classified as being an $RP{=}O(OH)_2$ acid, indicating that no thermal degradation has occurred regarding the two PO_3H_2 moieties.

3.5.1.2 Solution spectroscopy

HEDP solutions in aqueous medium were investigated by means of Raman spectroscopy as it is by far the superior vibrational technique when investigating systems of an aqueous nature. The degree of protonation of HEDP is highly pH-dependent [7] and thus knowledge of the solution's pH indicates what species are present or vice versa. In Section 3.2 it was shown that this change can be followed by means of NMR spectroscopy, but NMR spectroscopy could not differentiate between the presences of discrete species in this case as the two techniques measure very different molecular properties. Figure 3-16 shows the experimental species distribution diagram obtained from the experimental pK_a values of HEDP [5] for the pH range 0.98 – 13.00. It can be seen that the

distribution is relatively uncomplicated, except in the region for H_3L^- where both H_4L and H_2L^{2-} overlap simultaneously.

Analysis of the FT-Raman spectra over the measured range of 100 – 3500 cm^{-1} showed that observable spectral changes occurred only in the region 860 – 1280 cm^{-1}, which contains the bands associated with the PO_3H_2 moieties. This is rationalised by the change in PO bond order that occurs as deprotonation progresses. Figure 3-17 shows a topographical plot of the 860 – 1280 cm^{-1} wavenumber region for pH = 0.98 – 13.00; the bands assigned to each protonated form of HEDP are indicated. The dominant PO bands at 957, 1061, 968 and 989 cm^{-1} can be assigned to the H_4L/H_3L^-, H_2L^{2-}, HL^{3-}, and L^{4-} species respectively. At low pH, the broad band observed at 1186 cm^{-1} is assigned to a mixed intra/intermolecular POH/water hydrogen-bonded band. Other bands observed in the Raman spectra during the investigation are at ~640, 1450, ~2878 and 2937 cm^{-1}, and are assigned to the ν^{s}C-P, $\delta^{as}CH_3$, $\nu^{s}CH_3$ and $\nu^{as}CH_3$ vibrations respectively [18]. It should be noted that over the whole measured pH range, the position of the ν^{s}C-P gradually shifted from 635 to 644 cm^{-1}. This shift to a higher wavenumber value as a function of pH has been reported previously [24].

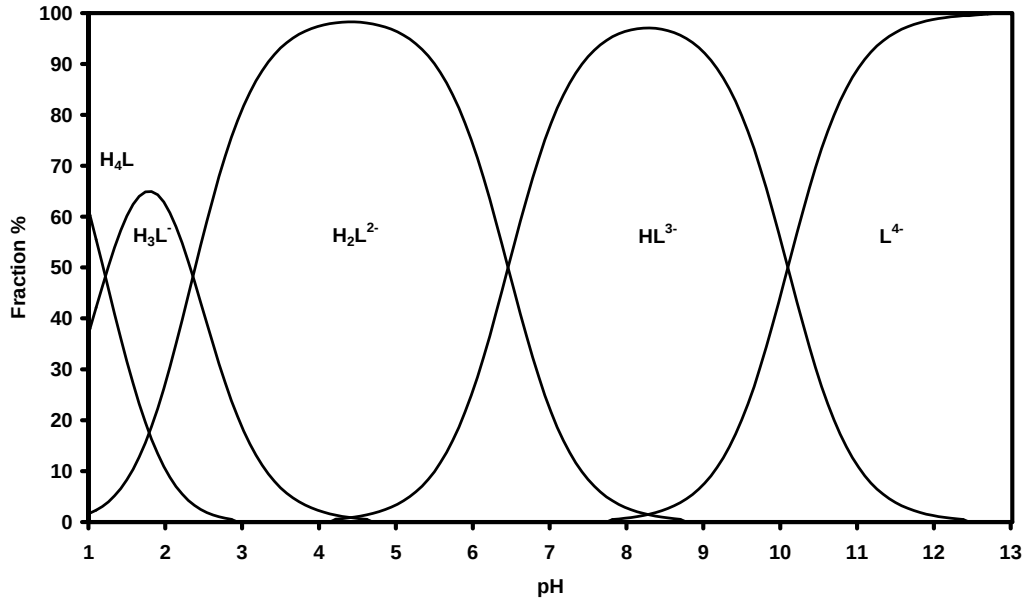

Figure 3-16. The species distribution diagram of HEDP(aq) for the pH region 0.98 – 13

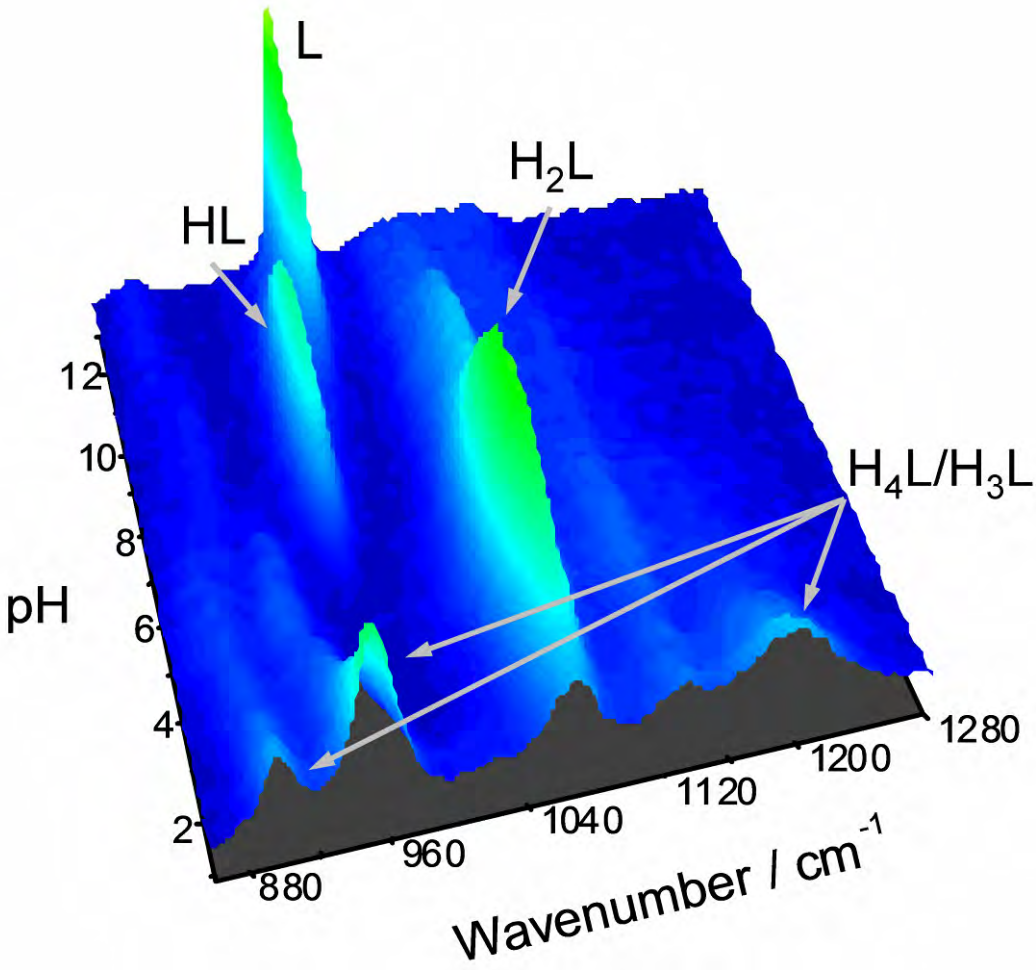

Figure 3-17. Topographical plot of the 860 – 1280 cm^{-1} wavenumber region for pH = 0.98 – 13.00 showing the bands of the various pH-dependent protonated forms of HEDP as indicated

It can be seen from Figure 3-16 that Raman spectroscopy does allow the discrete observation of the various protonated species of HEDP. Even though NMR could not differentiate between discrete species, it is seen in Figure 3-18 that if we define x as the independent variable for the function plotted in Figure 3-1, it accurately follows the same trend as the appearance and disappearance of the νPO Raman bands of the various protonated forms of HEDP where the ^{31}P NMR data are superimposed on a stack plot of the Raman spectra of the νPO region for the pH range 0.98 – 13.00.

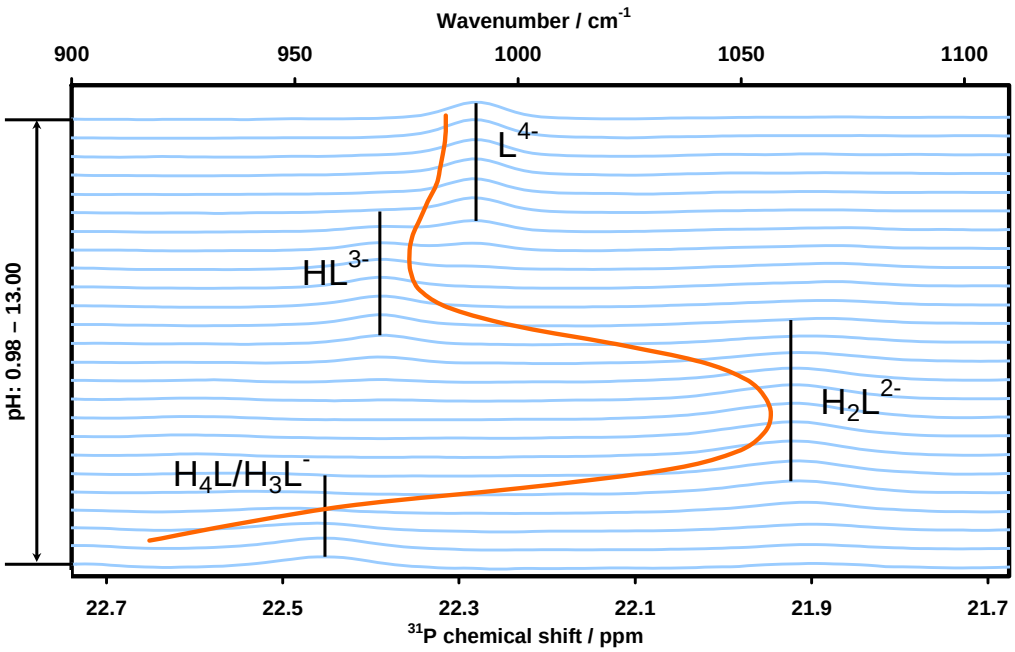

Figure 3-18. An overlay plot showing the similar trend of the ^{31}P NMR chemical shift relative to the discrete Raman band positions of the various protonated forms of HEDP for the *ν*PO vibrational region

Even in solution, HEDP produces a complex Raman spectrum for analysis in the *ν*PO region, which fortunately simplifies as HEDP is deprotonated at higher pH values. Various attempts at modelling the vibrational spectrum of HEDP·H_2O in the solid state did not reproduce the experimental vibrational spectrum satisfactorily. This is most probably due to the strong contribution of the hydrogen-bonded water molecule, as well as to the infinite hydrogen-bond networks that exist in the solid-state crystal structure. In solution, the HEDP molecule is free of solid-state interferences and constraints, and the Raman spectrum is simplified due to the dynamic nature of solutions. Unfortunately, due to the free bond rotation that occurs in solution for HEDP, the problem arises of determining which conformer for each species is the most probable to model and reproduce correctly the experimentally observed spectrum as the theoretical calculation is done on a statically solvated molecule and HEDP itself is not rigid. The strong hydrogen bond present in the solid-state structure indicates that strong inter- and intramolecular interaction should not be ignored in solution as it has previously been reported that this is highly likely to occur at low pH and high HEDP concentrations [24]. Taking all these factors into account, it is therefore

highly probable that there is a strong preference (energetically or sterically) for certain conformers to be predominant in solution. In Figure 3-19 it can be seen that both H_4L and L^{4-} are achiral, with L^{4-} having the highest degree of rigidity of all the protonated forms. H_3L^- and HL^{3-} are chiral, due to the non-equivalent degree of protonation for the two PO_3H_2 moieties but, in principle, H_2L^{2-} could be either chiral (both H^+ on the same phosphonic group) or achiral (one H^+ per phosphonic group). The chiral form of H_2L^{2-} was disregarded in this case. Judging from the similarity in pK_a values of H_4L and H_3L^- (Table 3-3), as well as from the crystal structures known for metal complexes containing H_2L^{2-} [9], the successive deprotonation will not occur from only one phosphonic acid group, but will rather involve one H^+ from each phosphonic group. All conformers that were either non-convergent or generated imaginary (i) wavenumbers were deemed unsuitable for further analysis, as they are not at an energy minimum for the molecule. There is no experimental evidence that the COH proton is removed; this aspect was not investigated.

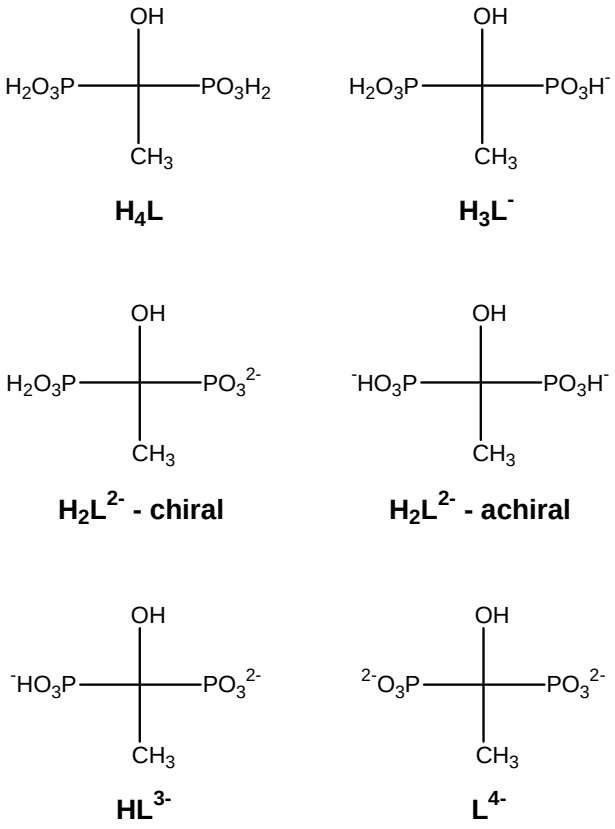

Figure 3-19. The various degrees of protonation possible for HEDP in solution

The conformational analysis done was by no means complete, but only preliminary to see if sensible conformers could be obtained to verify and explain the measured solutuion Raman spectra for the various protonated forms of HEDP(aq). H_4L proved to be the most problematic of all the protonated forms as it is not a rigid molecular system. As quantum mechanical calculations are time-consuming, the simpler molecular mechanics approach was employed first to generate initial starting conformers for H_4L. The Macromodel software package generated 31 non-equivalent, convergent conformers for H_4L, after a 1000 cycle molecular dynamics run. These 31 conformers had an energy distribution of 20.4 kJ/mol from the lowest to the highest energy conformer generated. At this point it should be mentioned that energies calculated by molecular mechanics have no physical meaning, but can still be used on a preliminary level to distinguish conformeric candidates that would have the lowest energy relative to other conformers. Fifteen of the conformers' mirror images were also determined and only one contained an internal mirror plane, accounting for all 31. The two conformers of lowest single-point energy contribute 21.3% to the total conformer population, and each contains two intramolecular hydrogen bonds. On this basis, these two conformers were further used for DFT calculations. Both conformers generated an *i*-wavenumber in their DFT-calculated vibrational spectra after being DFT-optimised first, indicating saddle point structures. These Raman spectra also do not compare satisfactorily with the experimental data as the experimental Raman spectra do not contain contributions from only H_4L (H_3L^- is present in significant quantities as seen from the species distribution diagram, Figure 3-16) and experimentally there seems to be strong intra/intermolecular hydrogen-bond influences as well. Figure 3-20 shows all 31 of the convergent conformers generated with the Macromodel software for H_4L, with the corresponding C and P atoms superimposed on each other. The CH_3 moiety is rigid for all conformers and the COH moiety can be seen to have only three main orientation possibilities ~120º from one another. The spread of orientations of the PO_3H_2 is a good indication of the difficulties encountered for H_4L and therefore molecular modelling of the H_4L Raman spectrum could not assist in the identification of a predominant conformer or the assignment of the Raman bands of H_4L. A full, extensive conformational analysis of H_4L would therefore be required to find the true energy minimum structure.

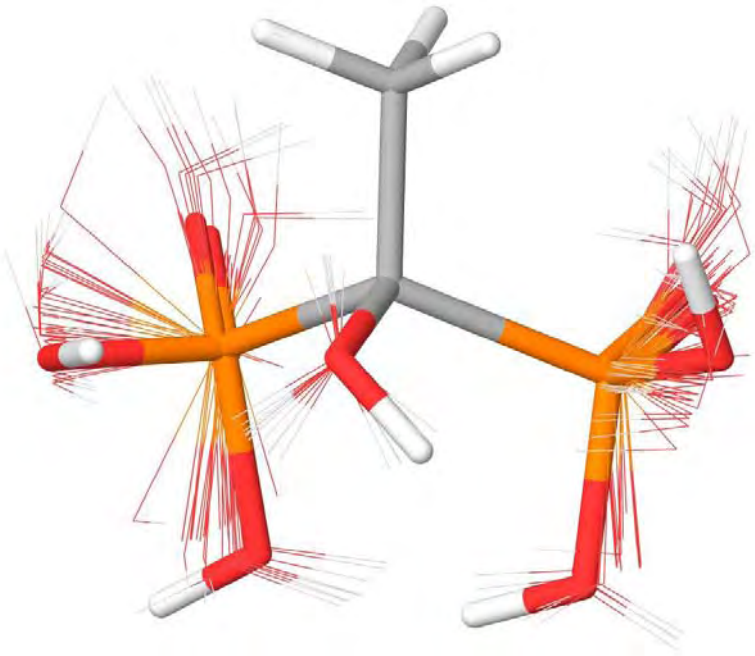

Figure 3-20. Superimposed structures of the 31 converging MM theory generated H_4L conformers. The conformer of lowest relative energy is illustrated as the tube structure

Curiously, by comparison, the theoretical Raman spectrum of the lowest energy conformer matched that of the experimental solid-state Raman spectrum of anhydrous HEDP (H_4L), and was used to tentatively confirm assignments as mentioned in Section 3.5.1.1. The assignment of the Raman spectrum of H_3L^- caused similar problems, but at least a most probable conformer could be determined. These difficulties are all ascribed to the hydrogen-bond interactions that are expected in this pH and concentration region [24]. All valid conformers found for H_3L^-, H_2L^{2-}, HL^{3-} and L^{4-} can be seen in Figure 3-21.

Vibrational assignments in the Raman spectra below 600 cm^{-1} were made difficult by the presence of a broad band centred at 479 cm^{-1} originating from the glass of the NMR tubes, as well as by the significant baseline fluorescence that was observed at lower wavenumbers for all samples. The vibrational assignments for H_2L^{2-}, HL^{3-} and L^{4-} above 600 cm^{-1} can be found in Table 3-14. A scale factor of 1.052 was used, except for bands marked with an *, which are reported unscaled.

This scale factor was calculated by comparing the experimental data with the theoretical data, and using the $\nu^{S}PO_3$ as reference point.

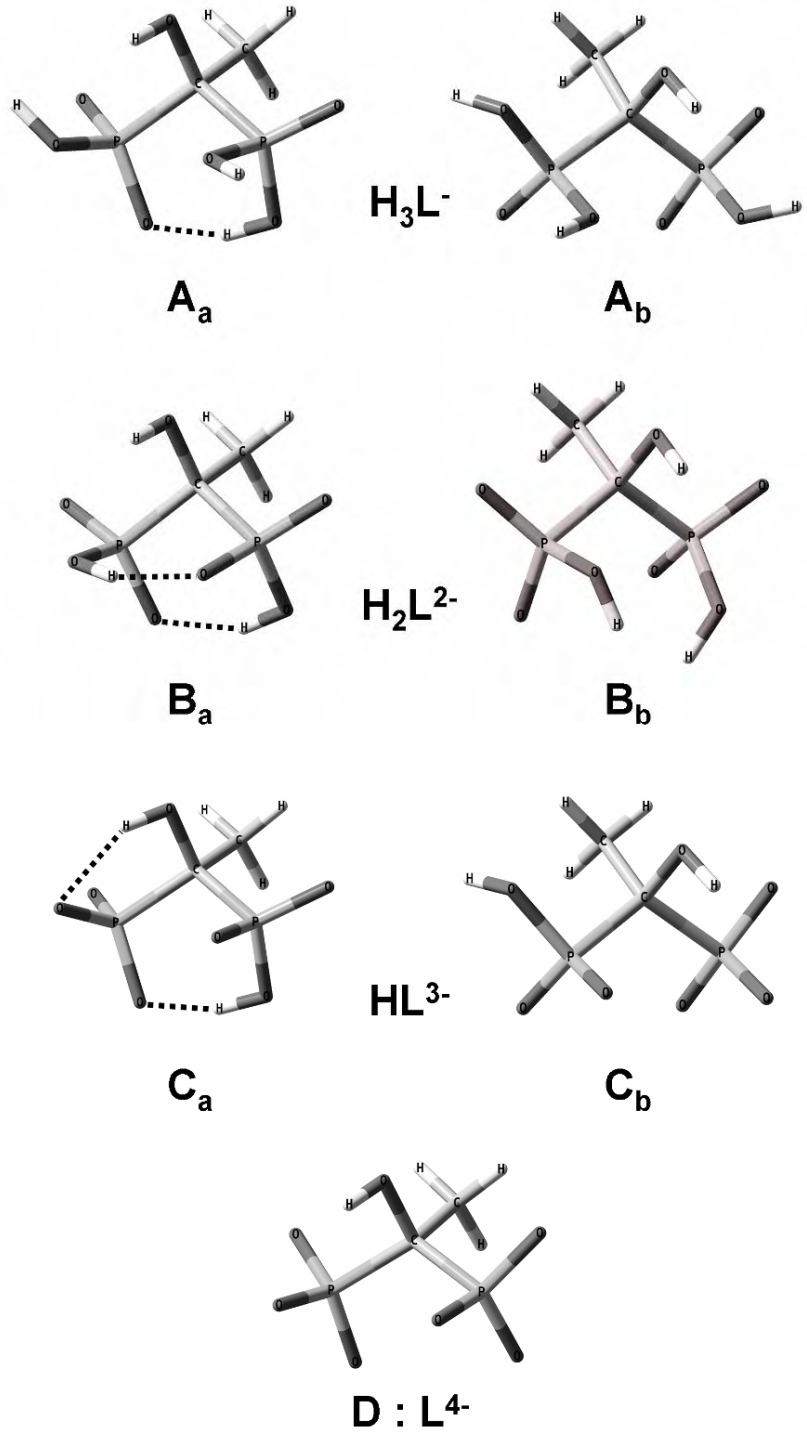

Figure 3-21. All conformers that did not give *i*-wavenumbers during the vibrational analysis for A: H_3L^-, B: H_2L^{2-}, C: HL^{3-} and D: L^{4-}. The intramolecular hydrogen-bonded conformers (a) were preferred above the (b) non-hydrogen-bonded conformers

Table 3-14. Vibrational assignment for the Raman spectra of the H_2L^{2-}, HL^{3-} and L^{4-} protonated forms

Assignment [20]	H_2L^{2-}		HL^{3-}		L^{4-}	
	Exp.	Calc.	Exp.	Calc.	Exp.	Calc.
ν^{s}C-P	637 m	634	639 m	638	645 w	634
νC-CO	808 vw	833	797 w	795	808 vw	799
νC-OH	926 vw	967	899 w	942	885 vw	903
$\nu^{s}PO_3^{2-}$	-		970 s	972	989 vs	992
$\nu^{s}PO_3^{-}$	1061 s	1071	-		-	
$\nu^{s}PO_3^{-}$ / $\nu^{as}PO_3^{2-}$	-		1069 m	1081	-	
νPO / νC-C / δCC-O	1132 w,br		1132 w,br		1105 w,br	
$\delta^{s}CH_3$	1381 vw	1402	1377 vw	1390 1400	1367 vw	1382
$\delta^{as}CH_3$	1454 w	1555 1563	1454 w	1550 1557	1452 vw	1555
$\nu^{s}CH_3^{*}$	2878 w	3031	2880 w	3027	2875 w	3025
$\nu^{as}CH_3^{*}$	2939 m	3097 3117	2937 m	3095 3104	2937 m	3094 3102
νPO-H*	2995 w	2910	2995 w	2907	-	

ν: stretch, δ: deformation
s: symmetrical, as: anti-symmetrical
vw: very weak, w: weak, m: medium, s: strong, vs: very strong
sh: shoulder, br: broad
* unscaled

Figure 3-22 shows the experimental Raman spectrum of a solution at pH 4.40 where H_2L^{2-} is present at maximum concentration, as well as those of two calculated conformers of two H_2L^{2-} that gave no *i*-wavenumbers for the region 600 – 1800 cm^{-1}. From calculation it was found that the broad band centred at ~1131 cm^{-1} represents vibrations associated with νPO, νC-C and δCC-O modes or mixtures thereof. The $\nu^{s}PO_3^{-}$ at 1061 cm^{-1} and the ν^{s}C-P at 637 cm^{-1} are the most intense bands in the experimental Raman spectrum of H_2L^{2-} and correlate best with the calculated Raman spectrum of conformer B_a. Conformer B_a has two intramolecular hydrogen bonds of ~1.8 Å each. A band observed at 2995 cm^{-1}, assigned to νPOH, is strongly indicative of intramolecular hydrogen bonding as it has been reported that this type of hydrogen bond can shift the νOH band to as low as 2500 cm^{-1} [20]. A shift to a lower wavenumber value of this band (due to the intramolecular hydrogen bonding) was also observed in the theoretical spectrum. In addition, the energy of conformer B_a has been calculated to be

30.84 kJ/mol lower than that of conformer B_b, making B_a the thermodynamically favoured conformer.

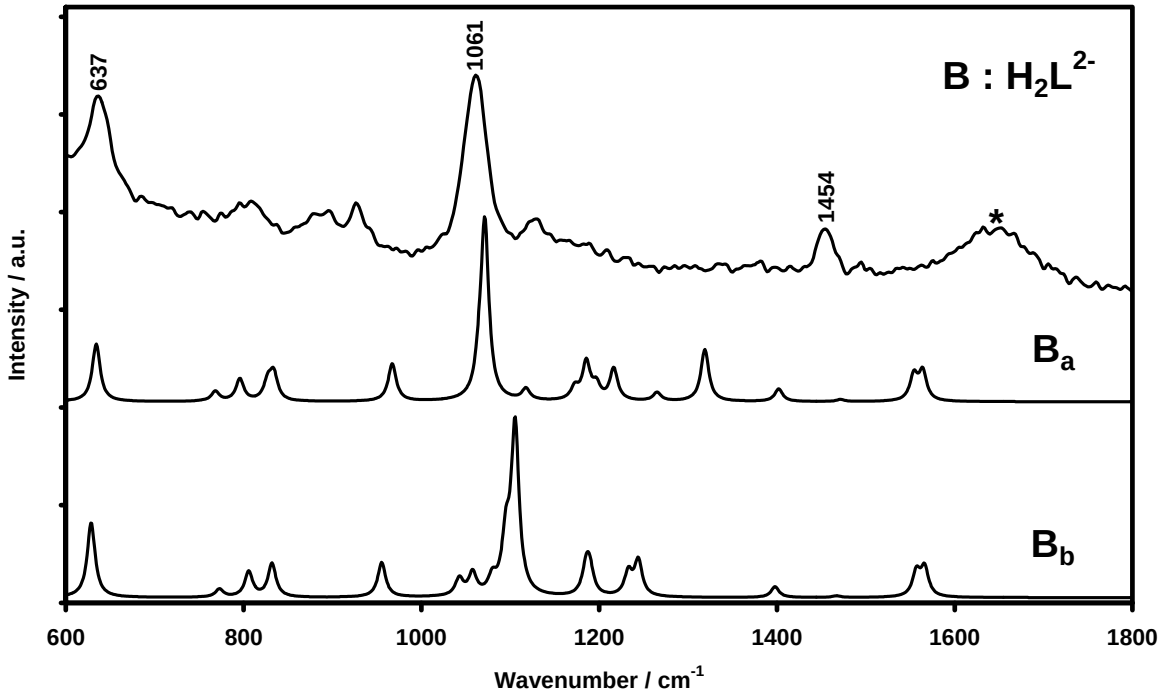

Figure 3-22. Comparison between the experimental and theoretically calculated Raman spectra for H_2L^{2-}. The band marked with an * originates from the solvent water

Figure 3-23 shows the experimental Raman spectrum of a solution at pH 8.20 where HL^{3-} is present at maximum concentration, as well as that of two calculated conformers of HL^{3-} that gave no *i*-wavenumbers. Once again, the broad band centred at ~1132 cm^{-1} represents vibrations associated with the νPO, νC-C and δC-C-O modes or mixtures thereof. The two calculated spectra look similar but, on closer inspection, the spectrum of conformer C_a matches the experimental data better, especially for the 637, 797, and 970 cm^{-1} bands. In addition, the calculated energy of conformer C_a was found to be 26.5 kJ/mol lower than that of conformer C_b, suggesting that it is thermodynamically more favoured, probably due to the two calculated intramolecular hydrogen bonds of 1.6 and 2.1 Å which exist at the POH···OP' and COH···OP' moieties. Once again a band at 2995 cm^{-1} is observed, which is indicative of the presence of intramolecular hydrogen bonding as found in conformer C_a.

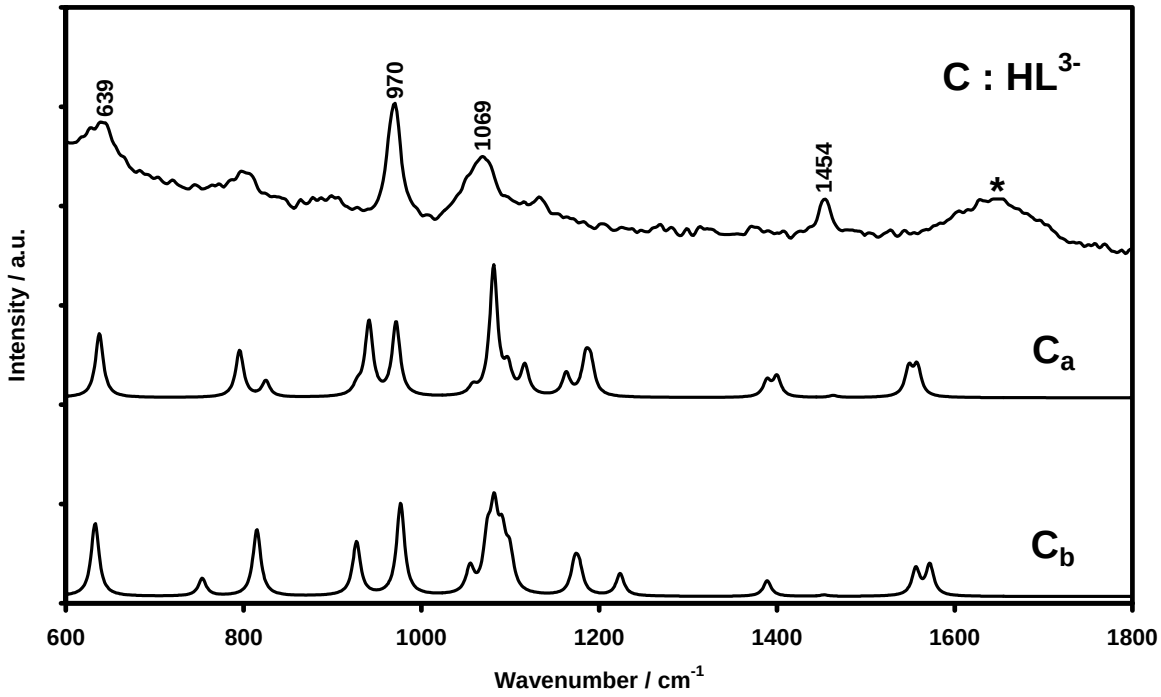

Figure 3-23. Comparison between the experimental and theoretically calculated Raman spectra for HL^{3-}. The band marked with an * originates from the solvent water

Figure 3-24 shows the experimental (of a solution at pH 13.00 where L^{4-} is present at maximum concentration) and calculated Raman spectrum of L^{4-}. It has the simplest spectrum of all the protonated forms of HEDP and assignment is therefore quite straightforward for this totally deprotonated form of HEDP. Similar to H_2L^{2-} and HL^{3-}, it was found that the broad band centred at ~1105 cm^{-1} collectively represents the vibrations associated with the νPO, νC-C and δCC-O modes or mixtures thereof. The dramatic increase in intensity of the $\nu^{S}PO_3^{2-}$ band at 989 cm^{-1} is a direct result of the two PO_3^{2-} moieties becoming chemically equivalent, similar to the solid-state case for anhydrous HEDP, but probably also symmetrically equivalent due to the dynamic nature of the solution environment. As mentioned previously, the comparison of H_3L^- and H_4L was complicated by the fact that the experimental Raman spectra overlap closely, and it was not possible to obtain pure species spectra to compare with the theoretically calculated data.

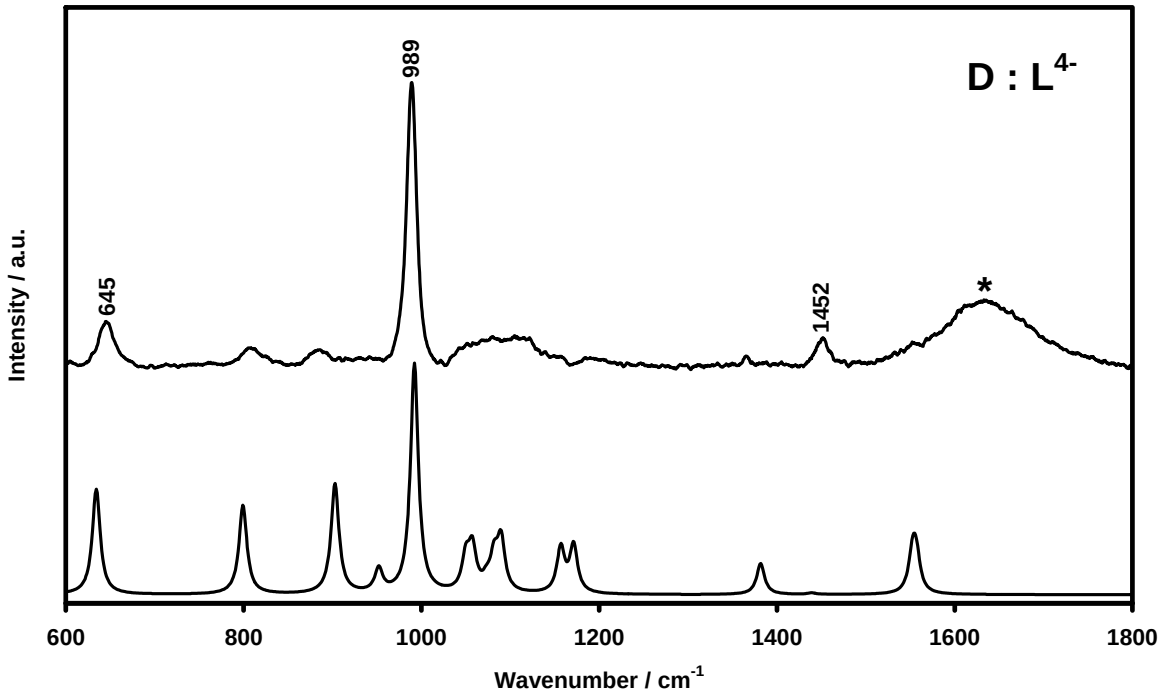

Figure 3-24. Comparison between the experimental and theoretically calculated Raman spectra for L^{4-}. The band marked with an * originates from the solvent water

The solid-state structure of $CaH_2L{\cdot}2H_2O$ makes for an interesting comparison with conformer B_b of H_2L^{2-}. The orientation of the $^-O\text{-}P\cdots P\text{-}O^-$ moiety in B_a is not suitable for chelation with an M^{2+} cation, even though it is the lowest energy conformer in solution, as evidenced by the experimental and theoretical data. The question therefore arises as to what the preferred conformer for coordination with M^{2+} could be. Using the solid-state crystal structure conformation of CaH_2L as input for the optimisation and Raman spectrum calculation in solution generates two *i*-wavenumbers and has a O=P···P=O dihedral angle of 134.4º, which indicates that it is not the preferred conformer for chelation in solution. If the Ca-chelated conformer B_b is used as input, a vibrational analysis is obtained with no *i*-wavenumbers and a O=P···P=O dihedral angle of 49.1º, indicating that it is probably the conformer required for chelation with Ca^{2+}. This implies that conformer B_a has to go through a transition state to become B_b, to coordinate with Ca^{2+}. In summary, conformer B_a is the uncoordinated conformer of $H_2L^{2-}(aq)$ and B_b the required higher energy, coordinating conformer of H_2L^{2-} in solution. Unfortunately, due to the insolubility of $CaH_2L{\cdot}2H_2O$, no experimental data could

be obtained for $CaH_2L(aq)$ to compare with the calculated Raman spectrum to confirm this postulation.

3.5.2 Solid-state Raman spectroscopy of CaHEDP salts

During the investigation of the interaction of 0.5 M and 0.005 M HEDP(aq) solutions with hydroxyapatite, two CaHEDP complexes were spectroscopically observed to form at the solid-solution interface. One was identified and characterised as $CaH_2L{\cdot}2H_2O$. Unfortunately, the other could not be isolated for characterisation, but the Raman spectrum could be obtained and is assigned. As stated in Section 2.2, the single crystal of $CaH_2L{\cdot}2H_2O$ used for XRD analysis was also used to obtain its reference Raman spectrum. In this section the analysis of only the Raman spectra will be discussed, and the nature of interaction in Chapter 4. Figure 3-25 shows the Raman spectra of the two macroanatomical types of bone, trabecular (cancellous) and compact (cortical) [26] in comparison with HA and $CaHPO_4$. The main bands are indicated to serve as a guide, but all bands have been assigned in Tables 3-15 and 3-16.

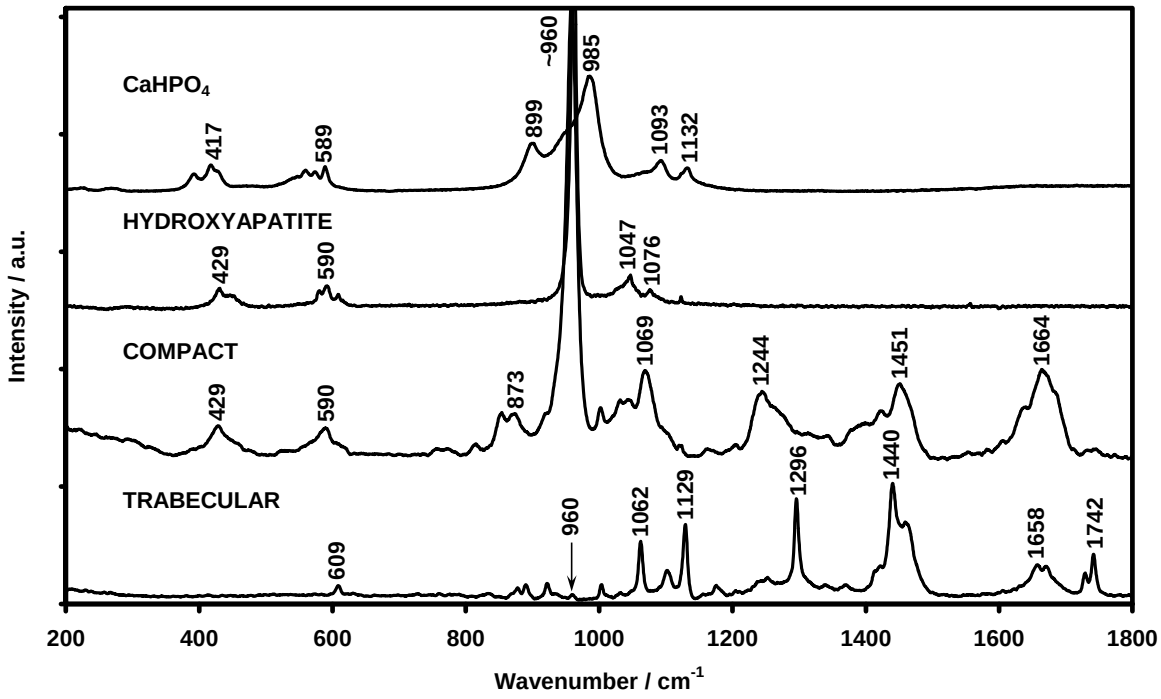

Figure 3-25. The Raman spectra of trabecular and compact bone, HA and $CaHPO_4$ for the region 200 – 1800 cm^{-1}

The difference between the Raman spectra of the trabecular and compact bone is very notable. This can be ascribed to the fact the calcium phosphate apatitic mineral is the dominant component in the compact bone, whereas the trabecular bone is much more organic in nature [26]. The organic components, such as collagen, remaining lipids and blood, dominate its Raman spectrum to such an extent that the most intense band of HA at 960 cm^{-1} is hardly visible. The majority of bands observed above 1100 cm^{-1} are assigned to this organic phase in trabecular bone. Penel *et al*. [27] have done a comprehensive assignment and discussion of the Raman spectra of the organic phase found in bone, and therefore the assignment of the organic phase's Raman bands observed on compact and trabecular (porous) bone during this study is given in Table 3-15, but will not be discussed in detail.

Figure 3-26 shows the comparative Raman spectra of $CaH_2L{\cdot}2H_2O$, the unknown Ca-HEDP complex and $HEDP{\cdot}H_2O$. Many vibrational bands are observed for all three compounds, but three non-overlapping bands were identified by which the compounds could be used to monitor the formation or disappearance of the Ca complexes as HEDP is added to the surface of bone, HA or $CaHPO_4$. These bands are assigned to the ν^{s}C-P, ν^{s}P-O(H) and δPO-H/ν^{as}P-O(H) vibrations and are: 627, 972 and 1036 cm^{-1} for $HEDP{\cdot}H_2O$; 641, 963 and 1072 cm^{-1} for $CaH_2L{\cdot}2H_2O$; and 658, 946 and 1088 cm^{-1} for the unknown Ca-HEDP complex. Similar to the analysis of the HEDP(aq) spectra, the bands assigned to the ν^{s}P-O(H) and δPO-H/ν^{as}P-O(H) vibrations show the most dramatic shift due to the change in the P-O bond order [30], which is in turn due to either the different modes of Ca^{2+} coordination or the degree of deprotonation. Other bands could probably also be used to differentiate between the three compounds, but might not be observed if they are present at lower concentrations. These can be used as a secondary means of confirmation when observed.

The vibrational assignment of HA and $CaHPO_4$, as well as the full assignment of the Raman spectra obtained from $CaH_2L{\cdot}2H_2O$ and the unknown Ca-complex, can be found in Table 3-16. Hartree-Fock (HF) methods were selected for the molecular modelling of $CaH_2L{\cdot}2H_2O$, even though these methods do not take dynamic electron correlations into account (see Section 1.6.1.1 and Ref. [31]).

This was done as no initial geometrical optimisation was performed on the structure as determined from XRD, resulting in a less time-consuming calculation. Initial test calculations done on simpler, single molecules (relative to the $CaH_2L{\cdot}2H_2O$ unit cell) to compare the HF and B3LYP/DFT methods, in combination with various basis set combinations, ranging from 6-31G(d) – 6-311G++(2d,p); showed that the scaling factor required for the computed vibrational wavenumbers was the only dramatic difference between the two methods. Notably, because HF methods do not show a linear relation between the calculated and theoretical vibrational wavenumbers as the DFT methods do [32], only wavenumbers below 2000 cm^{-1} were assigned. Bands observed above 2000 cm^{-1} were assigned from literature sources (see Table 3-16).

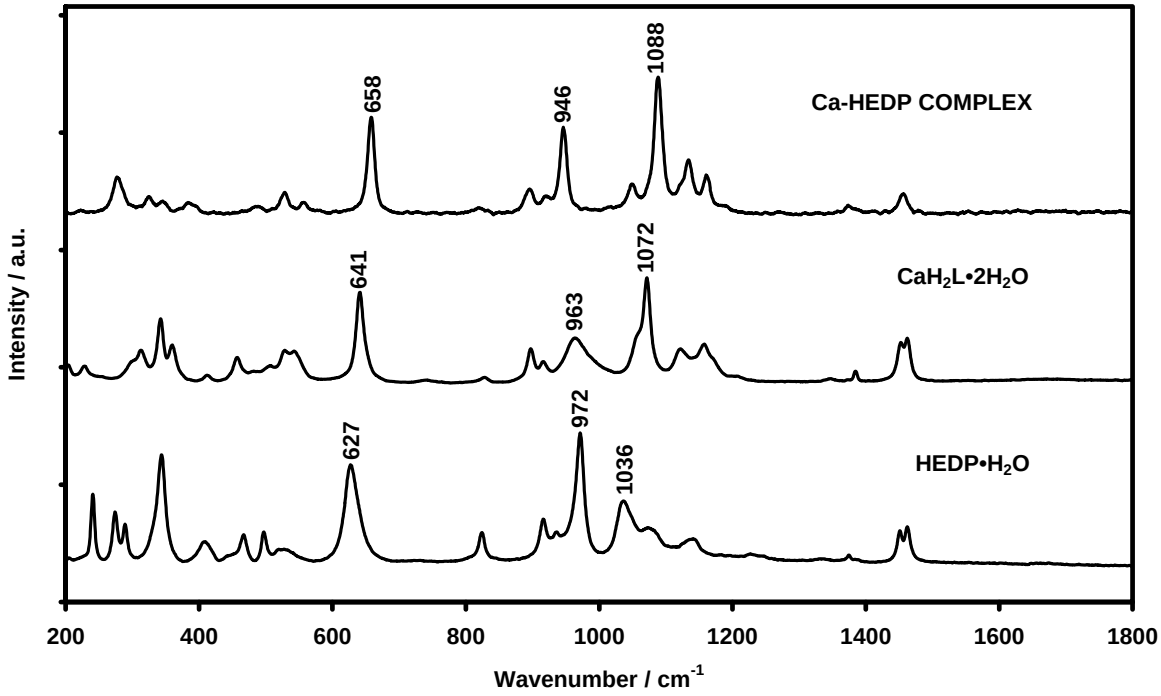

Figure 3-26. Comparative Raman spectra of HEDP, $CaH_2L{\cdot}2H_2O$ and the unknown Ca-HEDP complex. Unique non-overlapping bands are labelled

Table 3-15.

Assignment [27]	Bone Compact	Bone Porous	Assignment [27]	Bone Compact	Bone Porous	Assignment [27]	Bone Compact	Bone Porous
$\delta^{as}PO_4^{3-}$	429		νC-C trans (phospholipids, blood)		1062	νC=C (blood)	1636	
$\delta^{as}PO_4^{3-}$	590		$\nu^{as}PO_4^{3-}$ / νCO_3^{2-} B type	1069	1102	ν*cis*-C=C (lipids)		1658
$\delta^{as}PO_4^{3-}$		609	νCO_3^{2-} A type			Amide I-α helix	1664	
νCO_3^{2-} B type / νC-C-O (collagen)	767		νC-C (*trans*-phospholipids, proteins)		1129	Amide I (collagen)		1670
νC-C / νC-O-C (collagen)	813	836	ν^{s}C-O-C (proteins: Tyr, Phe) (collagen, lipids, blood)		1176	νC=OOC (collagen, lipid)	1744	1729 1742
δC-C-H_{ar} / (collagen, lipids)	854		Amide III-β (collagen, blood)	1244	1241 1253	νPO-H		2727
νC-C Ile / Val / Thr / Tyr (collagen, lipids)	873	878	δC=CH (phospholipids)		1296	$\nu^{s}CH_2$ (lipids)		2848
νP-OH / νC-C Pro ring (collagen, lipids)	922	922	Amide III-α helix (collagen, blood)		1339	$\nu^{as}CH_2$ (lipids) / $\nu^{s}CH_2$ (proteins)	2883	2883
νC-C_{aliph} Lys / Val / Leu (collagen)		935	Heme (collagen, blood)	1390		Heme (blood)		2915
$\nu^{s}PO_4^{3-}$	959	960	Heme (blood)	1422	1419	$\nu^{s}CH_3$ (proteins, lipids) / $\nu^{as}CH_2$ (proteins)	2942	2936
νHPO_4^{2-} / Phe (collagen, lipids)	1002	1004	δCH_2 (lipids)		1440	$\nu^{s}CH_3$ (lipids)		2958
$\nu^{as}PO_4^{3-}$	1042	1050	$\delta^{as}CH_3$ / δCH_2 (proteins, collagen, blood)	1451		$\nu^{s}CH_3$ (collagen, blood)	2978	
Pro / Phe / Tyr / Thr	1030	1032	δCH_2 (lipids)		1459	νC=CH (collagen, blood)	3066	3061

ν: stretch, δ: deformation; s: symmetrical, as: anti-symmetrical; ar: aromatic, aliph: aliphatic

Amino acids: Ile (isoleucine), Val (valine), Thr (threonine), Tyr (tyrosine), Lys (lysine), Leu (leucine), Pro (proline), Phe (phenylalanine)

CO_3^{2-} A type – CO_3^{2-} substituted in OH^- site of HA

CO_3^{2-} B type – CO_3^{2-} substituted in PO_4^{3-} site of HA

Table 3-16. Raman band assignments for $CaHPO_4$, $CaH_2L{\cdot}2H_2O$ and the unknown Ca-HEDP complex

Vibrational assignments†	Solid 'substrates'		HEDP complexes		
	$CaHPO_4$ [28]	HA [29]	Ca-complex	$CaH_2L{\cdot}2H_2O$ Exp.	Calc.
Probable lattice vibrations	140 w		114 vw	110 vw	
	180 w			121 vw	
	224 w		144 vw	149 w	
	268 w			170 w,sh	
			185 vw	182 w	
νOH…O				204 w	263
			223 vw	228 w	273
δC-C			277 m	254 vw	
				301 m,sh	
δOPO			326 w	313 m	311
			345 w	342 s	332
			383 w	360 m	355
				412 w	394
$\delta^{as}PO_4^{3-}$	392 m	431 m			
	417 m	447 m			
	428 m,sh				
δOPO				457 m	459
			487 w	482 w,sh	494
				506 w	513
			529 w	528 m	559
$\delta^{as}PO_4^{3-}$	539 m				
	560 m	580 m			
	573 m	592 m			
	589 m	608 w			
			557 w	543 m	589
νC-P			658 s	641 vs	643
				742 w,br	756
νC-C-O			819 w	828 w	871
$\nu^{as}PO_4^{3-}$	899 s				
νC-O-H			897 m	898 m	909
ν^{s}P-O(H)			920 m,sh	916 w	929
			946 s	963 m,br	1000
					1028
$\nu^{s}PO_4^{3-}$	958 s,sh	962 vs			
	985 vs				
$\nu^{as}PO_4^{3-}$	1065	1047 m			
	1093				
	1132				
δPO-H / ν^{as}P-O(H)			1049 m	1057 sh	1054
			1088 s	1072 vs	1076
$\nu^{as}PO_4^{3-}$		1076 w			
δCO-H			1134 m	1122 m	1116

Vibrational assignments†	Solid 'substrates'		HEDP complexes		
	$CaHPO_4$ [28]	HA [29]	Ca-complex	$CaH_2L \cdot 2H_2O$ Exp.	Calc.
νP=O / δPOH			1160 m	1158 m	1141
			1188 sh	1172 sh	1185
				1207 w	
$\delta^{s}CH_3$			1374 w	1373 vw	
				1385 w	
$\delta^{as}CH_3$			1456 m	1452 s	
				1462 s	
νPO-H			2725 w	2743 w	
$\nu^{s}CH_3$			2882 m,sh	2883 m	
			2887 m		
			2953 vs	2950 vs	
$\nu^{as}CH_3$				2983 sh	
				2991 s	
			3006 s,sh		
			3010 vs		
νO-H / νOH_2			3222 m	3224 vw,br	
				3354 w	
				3409 sh	
νO-H / HA		3578 s	3571 m		

† Bands that could be confidently assigned from the calculated spectra are given. Bands above 2000 cm^{-1} show a large scale factor error and are therefore not given as they could be confidently assigned from the literature [20–24].
ν: stretch, δ: deformation
s: symmetrical, as: anti-symmetrical
vw: very weak, w: weak, m: medium, s: strong, vs: very strong
sh: shoulder, br: broad

Three calcium complexes in solution have been identified for HEDP by means of glass potentiometric (GEP) studies, namely $CaHL^-$, Ca_2L and CaL^{2-}, for which the stability constants (log β) are 13.17, 9.53 and 5.34 respectively [5]. The fact that CaH_2L was not found by GEP, and the unknown complex formed (supposedly at lower HEDP concentrations) prompted the modelling of hypothetical solution compositions, using literature-reported data [5] and an assumed stability constant of the complex CaH_2L. The total Ca^{2+}(aq) concentration was allowed to vary over a wide range, between $1x10^{-3}$ and $1x10^{-7}$ M. The reason for this was that the stock HEDP solution was calcium-free and that most of the calcium leached from the solid phase (HA, bone, or CaHPO4) was instantly involved in the complex-formation reaction with HEDP, as evidenced by the Raman spectra in Figure 3-26. From the modelling results it appeared that the overall stability

constant (log β) for CaH_2L should be approximately 18. A selection of the modelled species distribution diagrams is shown in Figure 3-27 to facilitate the discussion. The species distribution diagram shown in Figure 3-27A (generated using the experimental conditions and stability constants of $CaHL^-$, Ca_2L, and CaL^{2-} [5] and CaH_2L, log β = 18.5) explains why the complex CaH_2L could not be obtained using GEP. CaH_2L is formed first (at lower pH values), but only to a small extent (only a small portion of the total calcium dissolved is in solution) and in the pH range where the H_2L^{2-} ligand is the dominant species present. The concentration of CaH_2L is therefore not significant enough to influence other Ca-HEDP equilibria dramatically. According to the reaction equation,

$$Ca^{2+} + H_2L^{2-} \rightarrow CaH_2L$$

there is no proton involved, and hence there is no change in the total free-proton concentration in a solution when only this complex is formed, and will therefore not be directly detected by GEP. Even though GEP is a powerful and versatile analytical technique for studying metal complexes, it is only successful when the free-proton concentration varies due to complex-formation reactions. Because CaH_2L is highly insoluble, it does not contribute to the change in free-proton concentration. Secondly, the species distribution diagrams in Figure 3-27 are for fully soluble Ca-HEDP systems, and even with this assumption CaH_2L is formed at very low concentrations as seen in Figure 3-27 A and 3-27B.

The complexes $CaHL^-$ and Ca_2L in Figure 3-27A start to form almost simultaneously in the pH range between 5 and 6, but Ca_2L forms predominantly in this region. When the total calcium concentration is decreased to $1x10^{-6}$ M and the total ligand concentration increased to 0.005 M (similar to the experimental conditions for the lower HEDP concentration of 0.005 M), then the solution composition changes dramatically (as can be seen in Figure 3-27B). Clearly, at the lower total metal ion concentration, the complex Ca_2L is not formed to any significant concentration level. $CaHL^-$ is the major calcium complex with only a small fraction of CaH_2L being formed. The results for an HEDP

concentration of 0.5 M can be seen in Figure 3-27C and represent the conditions of the experimental results when the formation of CaH_2L at very low pH was observed and the conditions under which the CaH_2L single crystal was obtained. Even at a high total metal ion concentration ($1x10^{-3}$ M), there is no evidence of Ca_2L formation. This strongly suggests that $CaHL^-$ is the unknown complex observed in the experimental Raman spectra obtained.

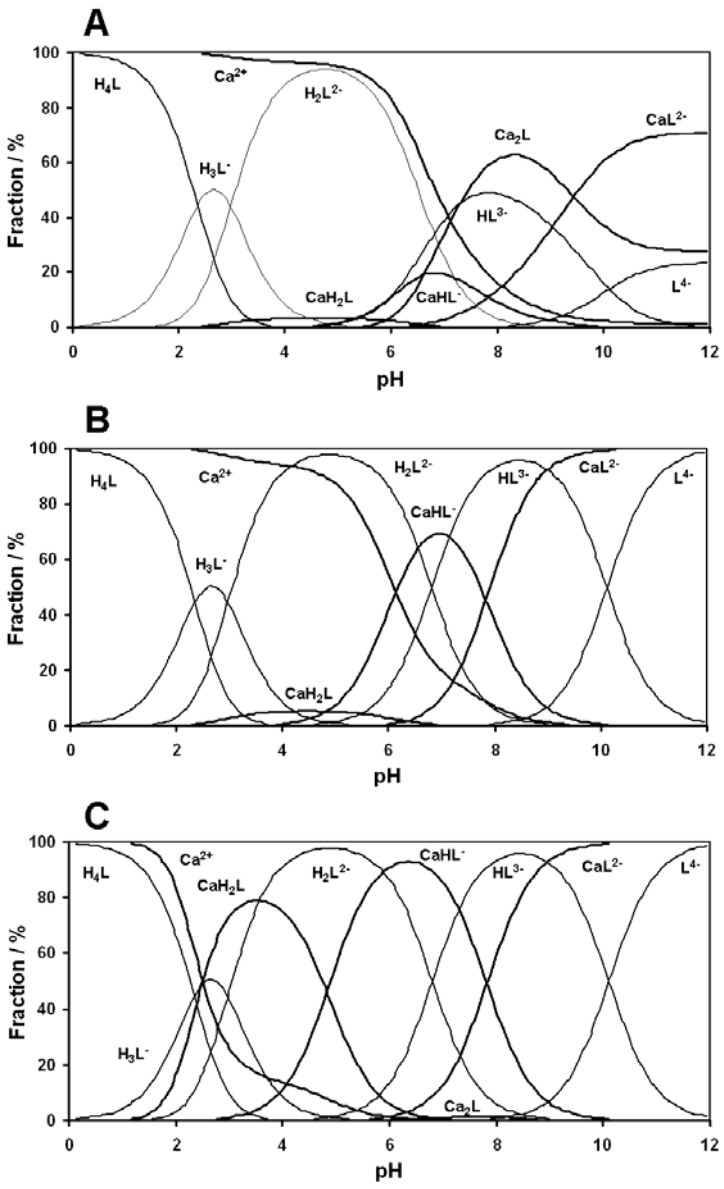

Figure 3-27. Species distribution diagrams of hypothetical, totally soluble Ca-HEDP systems generated under different total ligand and metal ion concentrations. A. $[L_T]$ = $1x10^{-3}$ M, $[M_T]$ = $9x10^{-4}$ M, log$\beta(CaH_2L)$ = 18.5; B. $[L_T]$ = $5x10^{-3}$ M, $[M_T]$ = $1x10^{-6}$ M, log$\beta(CaH_2L)$ = 18.0; C. $[L_T]$ = $5x10^{-1}$ M, $[M_T]$ = $1x10^{-3}$ M, log$\beta(CaH_2L)$ = 18.0

Further evidence that $CaHL^-$ is the unknown Ca complex can be found in the shift of the ν^sC-P band to a higher wavenumber as HEDP is deprotonated in solution [24] and as observed in this study. In Figure 3-26 the shift of this band occurs such that the wavenumber value of the unknown Ca-HEDP complex (658 cm^{-1}) is greater than that of $CaH_2L{\cdot}2H_2O$ (641 cm^{-1}), which in turn is greater than that of $HEDP{\cdot}H_2O$ (627 cm^{-1}) giving the series: unknown Ca-HEDP complex > $CaH_2L{\cdot}2H_2O$ > $HEDP{\cdot}H_2O$. The degree of protonation of $HEDP{\cdot}H_2O$ is greater than that of $CaH_2L{\cdot}2H_2O$, and if the shift of the ν^sC-P band is used as an indicator of the degree of deprotonation, we can write a deprotonation series, based on the ν^sC-P band position, of: $Ca_x(H_yL)_z{\cdot}nH_2O$ > $CaH_2L{\cdot}2H_2O$ > $H_4L{\cdot}H_2O$. For this series to be true, y = 0,1. However, y = 0 is not the most likely possibility as it is formed at high pH values, making y = 1 the likely candidate. To have a neutral solid present means the formula unit is $Ca_3(HL)_2{\cdot}nH_2O$, where n is unknown at this stage.

Attempts to increase the amount of this Ca-HEDP complex was done by adjusting the pH of an HEDP solution by addition of $Ca(OH)_2$(s). If the molar ratio of $Ca(OH)_2$:HEDP was 1:1, $CaH_2L{\cdot}2H_2O$ precipitated (confirmed by XRD), while a ratio of 2:1 gave a mixture of complexes that could not be resolved by XRD.

3.6 Multivariate curve resolution

The species distribution diagram of HEDP(aq) has been generated from experimental [5] data, as seen in Figure 3-16, for the pH region under investigation. As stated previously, it was not possible to resolve the pure spectra of H_4L and H_3L^- from the experimental data due to the species overlap associated with the pH region in which these species are shown to be at their maximum concentration. Multivariate curve resolution (MCR) was therefore utilised to attempt to distinguish the various species from one another. The region of 860 – 1280 cm^{-1} was selected as a suitable range in the Raman spectra for MCR analysis as it contains the bands associated with the PO_3H_2 moieties that vary with pH. The bands below this range were weak and, due to the high fluorescence background observed in the lower wavenumber region, it was

suspected that they would introduce errors into the MCR analysis. Particular bands such as the ν^{s}C-P stretch at ~640 cm^{-1}, which exhibits a small but constant shift over the pH range, for example, could result in each spectrum being identified as a separate component. The region above 1280 cm^{-1} contains bands assignable to the aqueous medium, as well as bands associated with the methyl vibrations that overlap with these water bands, and it was thus also deemed unnecessary to include this region.

Therefore, if a hydrogen-bonded system were to exist at low pH and high HEDP concentration, and were to contribute significantly to the Raman spectra, one could expect MCR analysis to find a six-component system when considering the total residuals of the MCR fitting. If such a hydrogen-bonded system does not contribute to the Raman spectra, one should determine only a five-component system, which represents the five protonated/deprotonated forms of HEDP. Also, each of the components is known from Figure 3-16 to have only one pH region of maximum concentration, and they can therefore not be observed more than once. Therefore the unimodal constraint [33] of MCR was also investigated.

Figure 3-28 shows the MCR-determined species distribution diagrams for a six-component system calculated multimodally and unimodally. By comparing the six-component species distribution diagrams in Figure 3-28A and 3-28B, it can be seen that a species is present which closely overlaps with the region where H_2L^{2-} is expected (blue line in Figure 3-28A), or a species is present simultaneously with H_3L and H_2L (red line in Figure 3-28B). The two unknown species are also present in pH regions where the hydrogen-bonded species are not expected. Therefore this confirms that a six-component analysis does not correctly describe the system. Therefore a hydrogen-bonded species does not contribute significantly enough to the experimental data set to be observed as a separate species.

The five-component multimodal and unimodal analyses both show very good agreement with the experimentally generated species distribution diagram, as can be seen in Figure 3-29A and Figure 3-29B respectively, two anomalies (marked *) are observed in Figure 3-29A. When considering only the species

distribution diagrams, it could be deduced that unimodality is a valid assumption as it is the best fit for the experimentally generated species distribution diagram, as seen in Figure 3-29B. Comparison of both the multimodal and unimodal MCR analyses generated with the experimental spectra obtained at pH values where each protonated form of HEDP is at its maximum concentration, as shown in Figures 3-30A and 3-30B respectively, shows good agreement for H_2L^{2-}, HL^{3-} and L^{4-}.

The discrepancies again arise in the cases of H_4L and H_3L^-. The experimental Raman spectrum at pH 0.98 is predicted to have an H_4L/H_3L^- ratio of approximately 3:2, indicating that both species will be observed simultaneously and that not all bands in the experimental Raman spectrum of H_4L can be assigned to H_4L only. For the unimodal result of H_4L, as seen in Figure 3-30B, it can be clearly seen that this MCR analysis associates all the bands observed experimentally as originating from H_4L, which is unlikely. In the multimodal case, seen in Figure 3-30A, we see that both H_4L and H_3L^- contain bands in their experimental Raman spectra that can be assigned to the pure component generated spectra of H_4L and H_3L^- as being contaminants, which is a much more realistic view of the species that are really present.

With regard to Figure 3-29A, the two anomalies (marked *) occurring in the multimodal case are thought to result from possible hydrogen-bonded species that manifest themselves in this fashion, rather than being detected as a formal species during the six-component MCR analysis. More evidence to support this possible hydrogen bonding can be found in the paper by Zeevaart *et al.* [5] on an H_6L^{2+} species that could be reinterpreted as strong hydrogen bonding rather than the presence of a formal species.

In summary, it seems that the deprotonation of HEDP over the pH range studied is well described as being a five-component system, with strong anecdotal evidence that hydrogen bonding occurs. This results in the generation of anomalies in the pure component distribution diagram as obtained by MCR analysis.

Unfortunately, these pure component spectra still seem to contain hydrogen bonding contributions associated with each separate protonated form, and they therefore do not compare well with the modelled vibrational data as the system modelled does not take intermolecular hydrogen bonding between two H_4L or H_3L^- units into account.

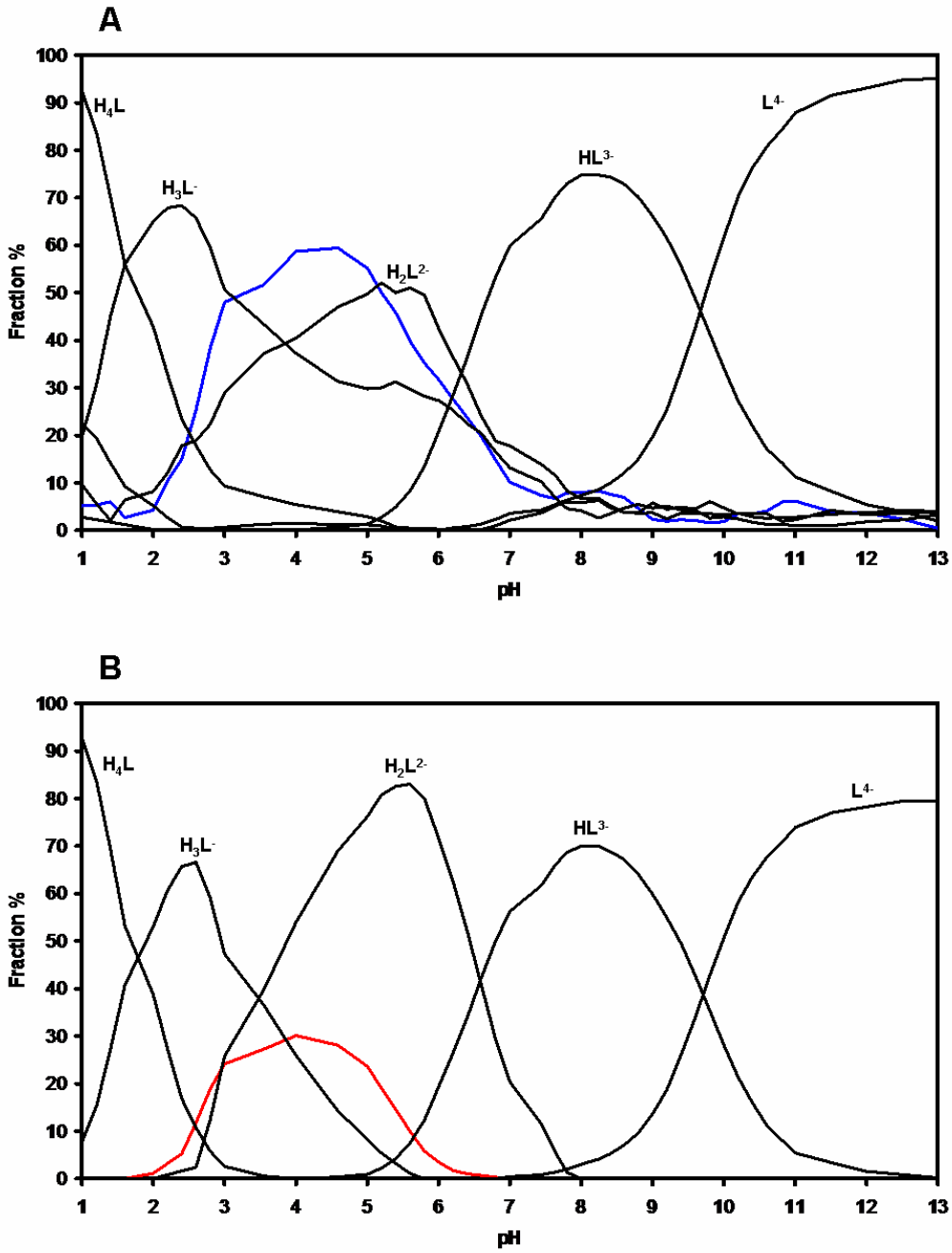

Figure 3-28. The six-component MCR species distribution diagram for HEDP calculated A. multimodally and B. unimodally. The component in blue and red is the sixth, unknown component

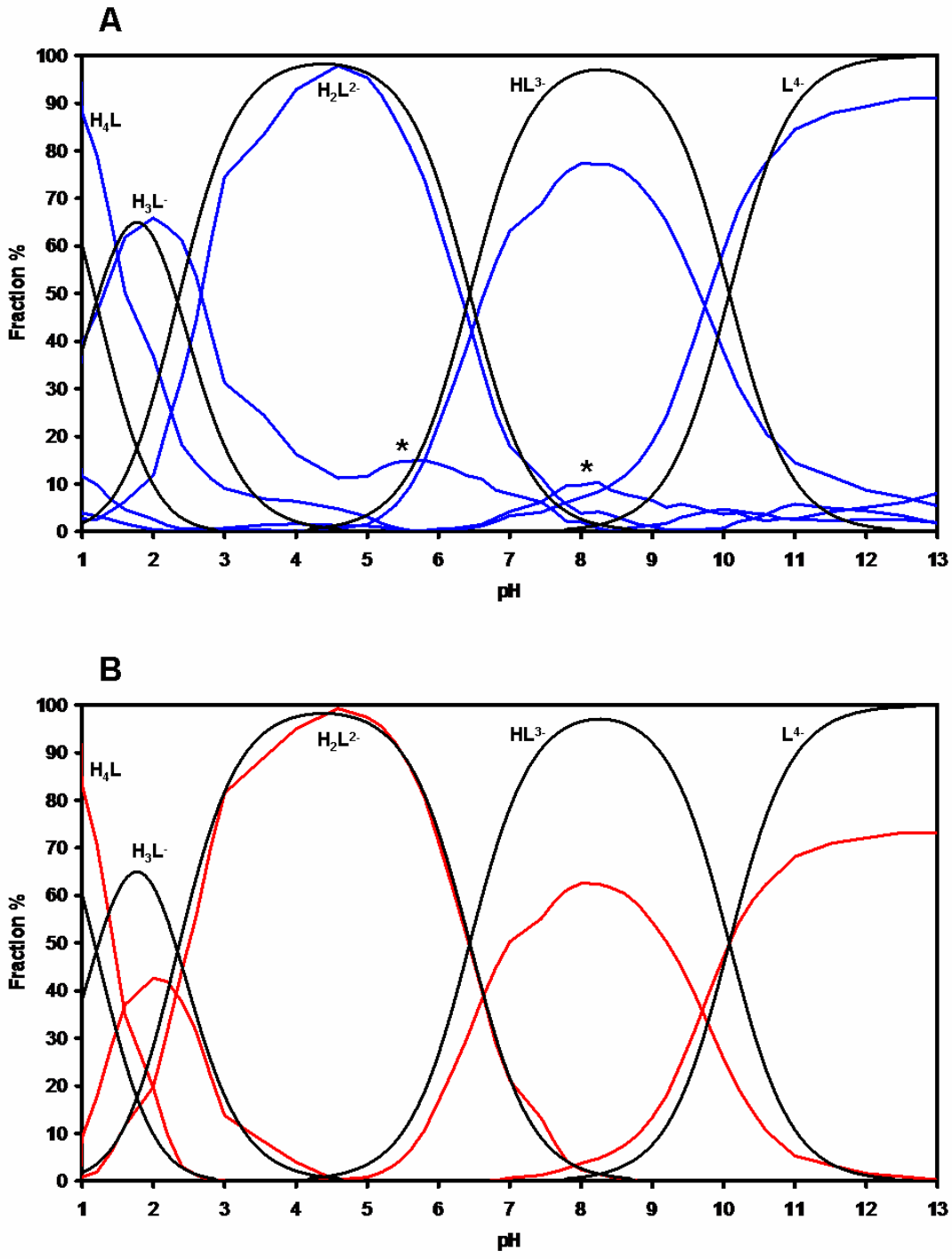

Figure 3-29. The five-component MCR species distribution diagram for HEDP calculated A. multimodally (in blue) and B. unimodally (in red). Both are superimposed on the experimentally generated species distribution curve (in black) for comparison. Anomalies marked with an * are discussed in the text

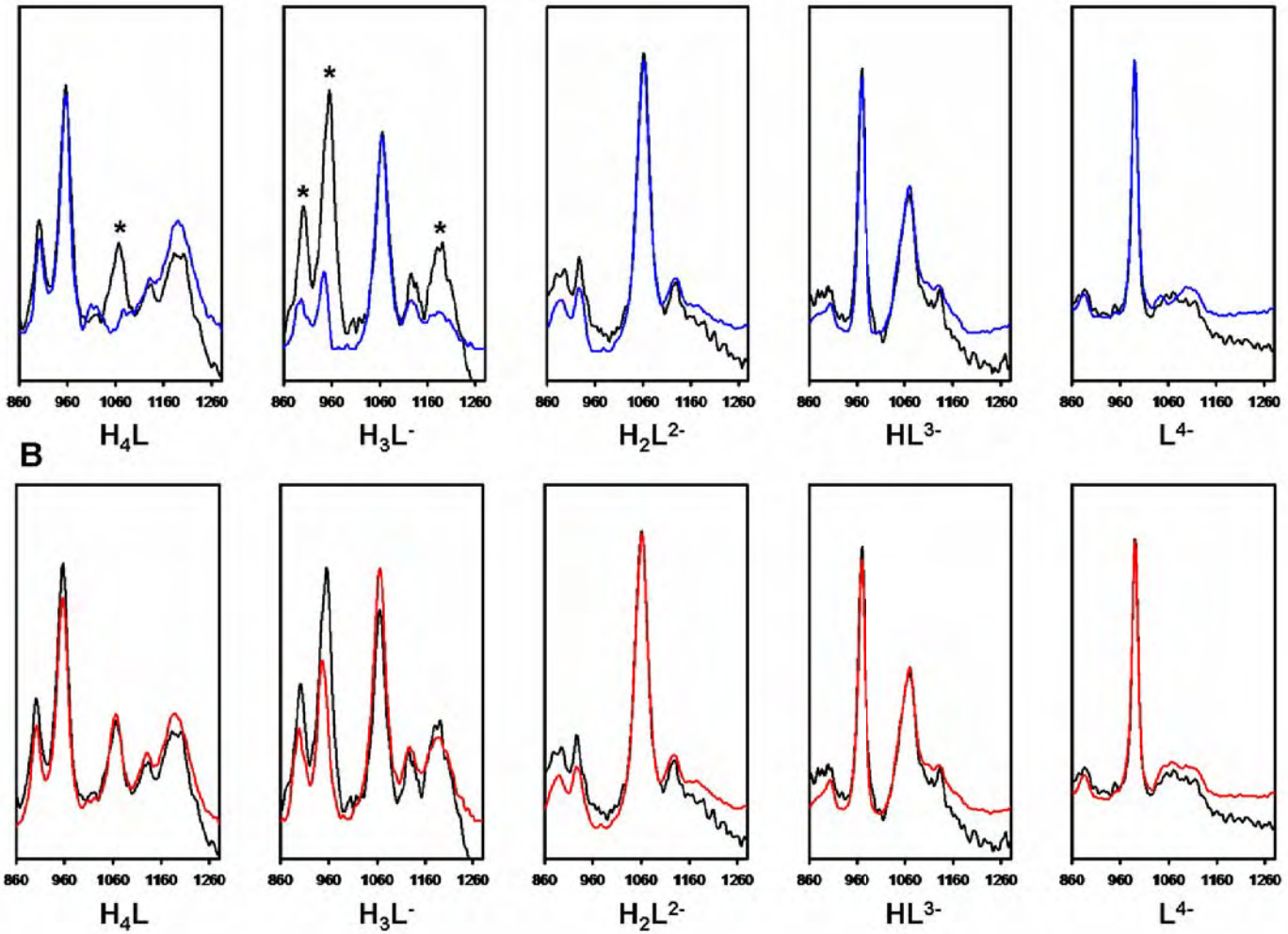

Figure 3-30. A. Multimodal (blue) and B. unimodal (red) generated pure component Raman spectra in comparison with experimental Raman spectra taken at pH values where each species is present at maximum concentration. The contamination of H_4L and H_3L^- can be clearly seen and the contaminant bands are marked with an *

3.7 Conclusions

It was illustrated in this chapter that various spectroscopic techniques can be used to obtain different, complimentary and supporting information regarding HEDP, its protonated forms and their conformers. Each technique gave different information regarding the nature of the structure and conformeric interactions. The use of molecular modelling to support what was observed shows that theoretical methods can be used to aid in the interpretation of HEDP's experimental data. This leads to a better understanding of HEDP, its various protonated forms and their conformers' interaction in solution, solid state and solid-solution interface that will be discussed in Chapter 4.

3.8 References

[1] E. Guenin, E. Degache, J. Liquier, M. Lecouvey. *Eur. J. Org. Chem.* **2004**, 2983.

[2] R.K. Harris, L.H. Merwin, G. Hägele. *Z. Naturforsch. B*, **1989**, *44*, 1407.

[3] R.K. Harris, L.H. Merwin, G. Hägele. *J. Chem. Soc., Faraday Trans.* **1989**, *85*, 1409.

[4] K. Popov, L.H.J. Lajunen, A. Popov, H. Rönkkömäki, M. Hannu-Kuure, A. Vendilo. *Inorg. Chem. Comm.* **2002**, *5*, 223.

[5] J.R. Zeevaart, N.V. Jarvis, I. Cukrowski, G.E. Jackson. *S. Afr. J. Chem.* **1997**, *50*, 189.

[6] E.G. Afonin, G.G. Aleksandrov. *Russ. J. Gen Chem.* **2003**, *73*, 340.

[7] A.J. Collins, G.W. Frasier, P.G. Perkins, D.R. Russell. *J. Chem. Soc., Dalton Trans.* **1974**, 960.

[8] V.A. Uchtman, R.A. Gloss. *J. Phys. Chem.* **1972**, *76*, 1298.

[9] J.P. Silvestre, N.Q. Dao, Y. Leroux. *Heteroatom Chem.* **2001**, *12*, 73.

[10] J.P. Silvestre, N.Q. Dao, G. Heger, A. Cousson. *Phosphorus Sulfur* **2002**, *177*, 277.

[11] A.J. Florence, K. Shankland, T. Gelbrich, M.B. Hursthouse, N. Shankland, A. Johnston, P. Fernandes, C.K. Leech. *Cryst. Eng. Comm.* **2008**, *10*, 26.

[12] N. Redman-Furey, M. Dicks, A. Bigalow-Kern, R.T. Cambron, G. Lubey, C. Lester, D. Vaughn. *J. Pharm. Sci.* **2005**, *94*, 893.

[13] A.A. Coelho, *J. Appl. Cryst.* **2000**, *33*, 899.

[14] V. Gogonea, C. Bãleanu-Gogonea, E. Osawa. *Theochem*. **1998**, *432*, 177.

[15] T. Ida, M. Ando, H. Toraya. *J. Appl. Cryst.* **2000**, *33*, 1311.

[16] A. Coelho. *Topas Academic Version 4.1 – Technical Reference*, **2007**, Chapter 12.

[17] R.A. Young (Ed.). *The Rietveld Method*, Oxford University Press, Oxford, **1996**.

[18] V.A. Uchtman. *J. Phys. Chem.* **1972**, *76*, 1304.

[19] G. Fiquet, P. Richet, G. Montagnac. *Phys. Chem. Miner.* **1999**, *27*, 103.

[20] D. Lin-Vien, N.B. Colthup, W.G. Fateley, J.G. Grasselli. *The Handbook of Infrared and Raman Characteristic Frequencies of Organic Molecules*, Academic Press Inc., London, **1991**, Chapters 2, 4 & 16.

[21] K. Nakamoto. *Infrared and Raman Spectra of Inorganic and Coordination Compounds,* 5th Edition, John Wiley & Sons, Chichester, **1997**, Part A.

[22] L.A. Myund, E.A. Bus'ko, N.I. Smirnova, S.N. Terekhin, N.M. Dyatlova, K.A. Burkov. *Vestn. Lenin U. Fiz. Kh. Seriya 4*, **1987**, *3*, 48.

[23] E.A. Bus'ko, L.A. Myund, S.N. Terekhin, K.A. Burkov, N.M. Dyatlova, N.A. Volkova. *Zh. Neorg. Khim.* **1988**, *33*, 603.

[24] L.A. Myund, E.A. Bus'ko, S.N. Terekhin, K.A. Burkov. *Vestn. Lenin U. Fiz. Kh. Seriya 4*, **1990**, *1*, 33.

[25] G.E. Walfaren. *J. Phys Chem.* **1990**, *94*, 2237.

[26] J.H. Lin. *Bone*, **1996**, *18*, 75.

[27] G. Penel, C. Delfosse, M. Descamps, G. Leroy. *Bone*, **2005**, *36*, 893.

[28] F.S. Casciani, R.A. Condrate. *Proc. Int. Congr. Phosphorous Compds*, **1980**, *2*, 175.

[29] G. Penel, G. Leroy, C. Rey, B. Sombret, J.P. Huvenne, E. Bres. *J. Mater. Sci., Mater. Med.* **1997**, *8*, 271.

[30] L. Popović, D. De Waal, J.C.A. Boeyens. *J. Raman Spectrosc.* **2005**, *36*, 2.

[31] K.V. Berezin, V.V. Nachaev, T.V. Krivokhizina. *Mol. Spectrosc.* **2003**, *94*, 398.

[32] K.V. Berezin, V.V. Nachaev. *J. Appl. Spectrosc.* **2004**, *71*, 164.

[33] R. Tauler, A. de Juan. In *A Practical Guide to Chemometrics*, P. Gemperline (Ed.). Taylor and Francis: CRC Press, New York, **2006**. Chapter 11.

4 Interactions of HEDP with HA

4.1 Introduction

Chapter 3 was concerned mainly with HEDP, its protonated forms and their conformations in the solid state and in solution. An understanding of the interaction of HEDP in solution with the bone mineral interface is also of importance to appreciate and compare the potencies of various bisphosphonates in the future. This chapter discusses the use of Raman spectroscopy to probe the nature of this solid-solution interface.

4.2 The interaction of HEDP with various calcium phosphates

Raman spectroscopy has been successfully used to characterise bone [1], HA as a model of bone [2, 3] and bisphosphonates [4–10]. The interaction of HEDP with HA has also widely been studied using theoretical [11] and experimental methods [12]. Thus far, it seems that only one published Raman spectroscopic study has attempted to investigate the interaction of a bisphosphonate with HA [13]. The main reason for this is probably the fluorescence that is observed when using FT-Raman with 1 064 nm excitation. This fluorescence is confirmed by an FT-Raman spectroscopic study of fluoroapatite, heated HA, calcium phosphate, $Ca_3(PO_4)_2$, calcium hydrogenphosphate dihydrate, $CaHPO_4{\cdot}2H_2O$, calcium hydroxide and calcium carbonate, which showed strong fluorescence bands in the Raman spectra of these compounds [14]. It was found to be due to the impurities present, such as rare earth minerals contained in the structure of the

compounds. It was therefore decided to in this study use an excitation line, such as the 514.5 nm (green) line of an Ar-ion laser, to ensure that the HEDP-solid interaction could be investigated without the interference of fluorescence.

As mentioned in Section 1.4, HA can be used as a simplified model of bone because the Raman spectra of the mineral phase of bone and HA match, as shown in Figure 3-25. $CaHPO_4$, unlike its dihydrate, $CaHPO_4{\cdot}2H_2O$ [15], does not occur in normal or pathological calcifications but it showed similar reactivity towards HEDP. In a previous study [16] an 'adhesion-decalcification concept' was proposed in which HPO_4^{2-} is initially formed during the action of carboxylic acids on HA and the subsequent decalcification thereof, allowing Ca^{2+}(aq) to be available for complex formation. A similar process might be involved in the reaction of bisphosphonic acids with HA, and thus $CaHPO_4$ was included as a source of aqueous HPO_4^{2-} for comparison with the reactions of HEDP with bone and HA. As Raman spectra were obtained at the solution/solid reaction interface, one would not be able to distinguish by Raman spectroscopy chemically between $CaHPO_4$ and $CaHPO_4{\cdot}2H_2O$ as the source of HPO_4^{2-}(aq).

The interaction of HEDP was investigated at both low (0.005 M) and high (0.5 M) concentrations of HEDP, and it appears that it interacts with bone, HA and $CaHPO_4$ in the same manner, forming needle-like fused spheres, as can be seen in Figure 4-1.

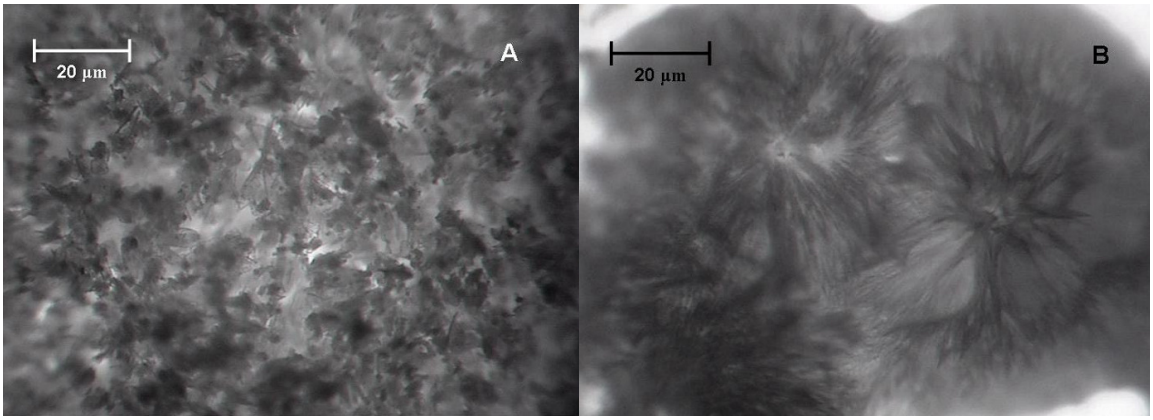

Figure 4-1. Micrographs of HA crystals A. before addition and B. after addition of 0.5 M HEDP

Figure 4-2 shows the Raman spectra of the reaction products formed during the HEDP(aq)-solid interaction. From this, it can be seen that HEDP reacts with the Ca^{2+} ion found in all three solids, forming similar Ca complexes. The three non-overlapping bands identified in Section 3.5.2 for $CaH_2L{\cdot}2H_2O$ and the unknown Ca-HEDP complex can be used to identify which of these compounds has formed. Bands at 640, 963 and 1072 cm^{-1} are assigned to the $CaH_2L{\cdot}2H_2O$ complex and bands at 658, 946 and 1088 cm^{-1} to the unknown Ca-HEDP complex. It can be seen that the Raman spectra of bone and HA are very similar, and judging from the relative intensities of the Raman bands of the two Ca complexes, it seems that the $CaH_2L{\cdot}2H_2O$ complex is dominant in the bone and HA cases, but the unknown Ca-HEDP complex is favoured in the $CaHPO_4$ interaction. This is proof that HA can be substituted for bone when studying the interaction of HEDP by means of Raman spectroscopy at the solid-solution interface.

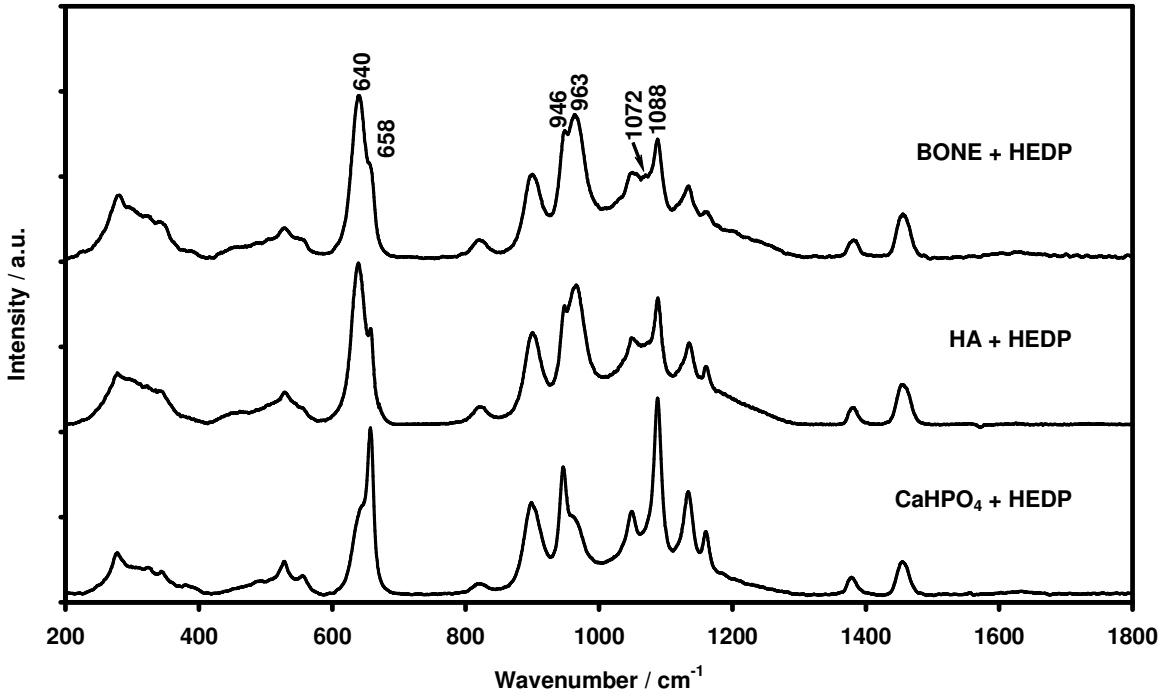

Figure 4-2. Raman spectra of products formed during the interaction of HEDP with bone, HA and $CaHPO_4$

It was seen that low HEDP concentrations (i.e. adding multiple drops of the 0.005 M solution (pH ~2.2) or a drop of 0.5 M HEDP (pH ~0.8) to the HA surface)

at first favoured the formation of the unknown Ca-HEDP complex identified by its Raman bands at 658, 946 and 1088 cm^{-1}. Further addition of a sufficient amount of HEDP resulted in $CaH_2L \cdot 2H_2O$ starting to form, as evidenced by the appearance of its Raman bands at 641, 963 and 1072 cm^{-1}, and both complexes were then present. Similar results were obtained for the addition of HEDP solutions to $CaHPO_4$. When a small volume of 0.5 M HEDP was added to bone, both complexes formed simultaneously. These observations suggest that the formation of the different complexes is dependent on the pH at the solid-solution interface where the CaH_2L complex forms under more acidic conditions. This is in good agreement with the reported successive, pH-dependent formation of several calcium complexes in solution [17], as well as with the formation of Ca complexes, as thoroughly discussed in Section 3.5.2 where it was postulated that the unknown Ca-HEDP complex was probably $CaHL^-$ and would likely precipitate as $Ca_3(HL)_2 \cdot nH_2O$.

All the above studies were done at conditions (low pH, high HEDP concentrations) not found at the biological bone surface, and the Ca^{2+} was liberated during an initial acid-leaching process. Two 0.5 M HEDP solutions were adjusted with NaOH to a pH of 5.0 and 7.4 respectively. At pH 5.0 the dominant protonated form of HEDP is H_2L^{2-}, whereas the human physiological pH is slightly basic at 7.4 [18]. Trying to record spectra at the solid-solution interface for these pH values proved unsuccessful. Both solutions were then placed in contact with HA for seven days and the solutions as well as the solid remaining after the solvent had evaporated were analysed using Raman spectroscopy.

Figure 4-3 shows the spectra of the two solutions. The experimentally generated species distribution diagram has HEDP present as 90% HL^{3-} and 10% H_2L^{2-} at pH 7.4. The bands at 970 and 1064 cm^{-1} in the spectrum obtained for the solution with pH 7.4 are assigned to the HL^{3-} form of HEDP, as seen in Table 3-14. The shoulder at ~1058 cm^{-1} may be a result of the most intense band of H_2L^{2-}. The bands observed at 931 and 1062 cm^{-1} in the spectrum of the solution at pH 5.0 are assigned to the H_2L^{2-} form of HEDP. Reference Raman spectra were obtained of solids before HA was brought into contact with the solution. These spectra represent the $Na_xH_yL_z \cdot nH_2O$ salts present in the solution.

If any change were to occur due to the interaction of the HEDP solution with HA, it would only be possible to observe this indirectly from the change in the spectra associated with these salts as a function of pH, as the solution composition changes. It will probably not be possible to observe directly with Raman spectroscopy any Ca-HEDP complexes that could have formed in this manner as such complexes are highly insoluble and would therefore not be present in significant quantities upon evaporation of the aqueous medium.

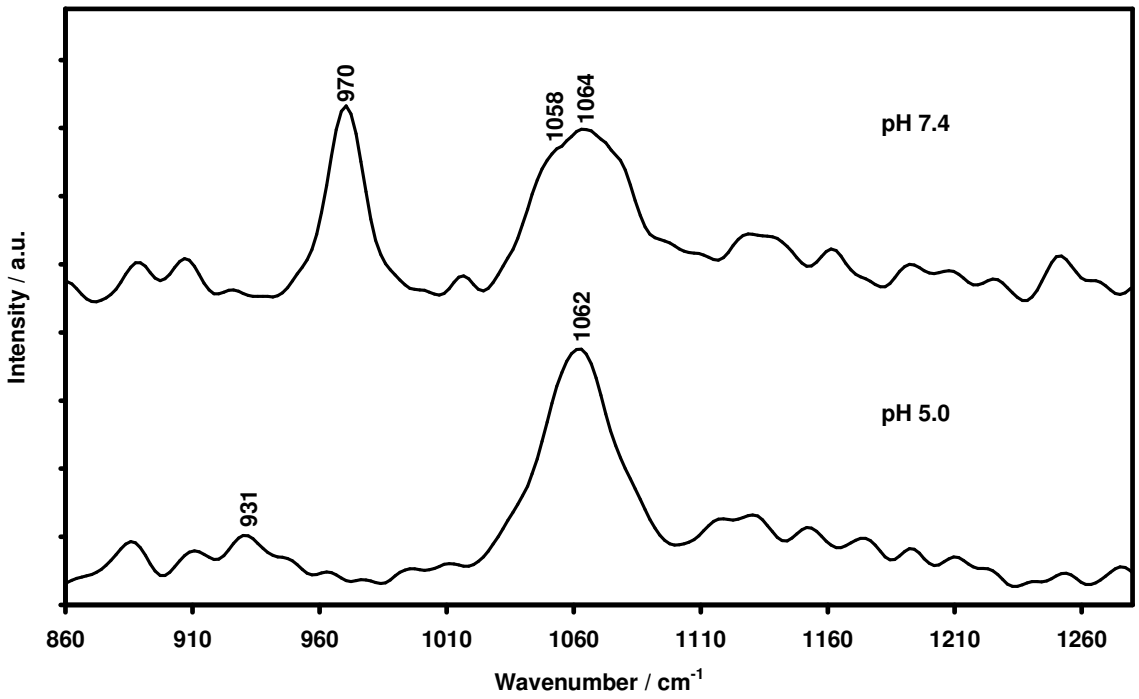

Figure 4-3. Raman spectra of HEDP solutions that were in contact with HA for seven days at pH 5.0 and 7.4

Figure 4-4 shows the Raman spectra of the solid obtained from evaporating the solution without HA interaction, as well as the solid obtained from solution brought into contact with HA at pH 5.0. The ν^{s}C-P band at 650 cm^{-1} is observed in both spectra, but an extra shoulder is observed in the spectrum at 665 cm^{-1} after HA was added. Having two ν^{s}C-P bands present indicates that a mixture of two compounds is probably present. The single band at 650 cm^{-1} is probably from the disodium HEDP salt, and the shoulder band at 665 cm^{-1} probably originates from the trisodium HEDP salt. A new band at 719 cm^{-1} is assigned to the ν^{as}C-P vibration. Changes in the region associated with νP-O(H) bands at

1072, 1087 and 1135 cm^{-1} can also be seen, indicating that a reaction did take place.

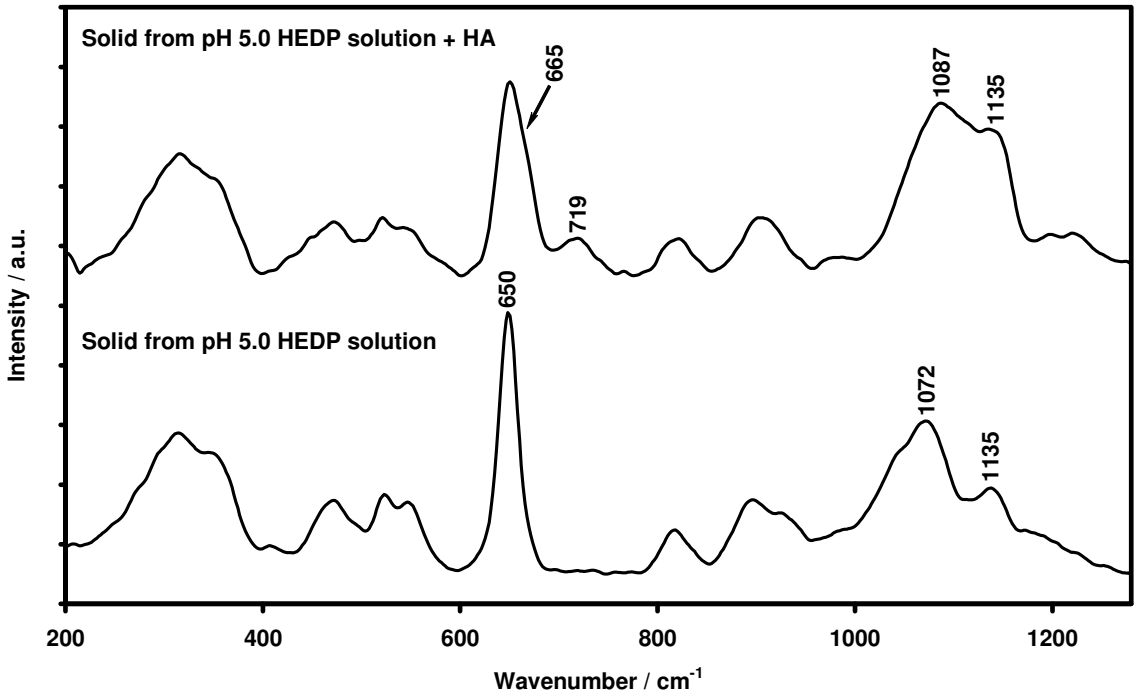

Figure 4-4. Raman spectra of solids obtained from solution before and after HEDP containing solution at pH 5.0 was exposed to HA

Figure 4-5 shows the Raman spectra of the solid obtained from evaporating the solution without HA interaction, as well as the solid obtained from solution after the solution was brought into contact with HA at pH 7.4. The new bands observed at 449 cm^{-1} are assigned to a δOPO vibration, and those at 721 cm^{-1} to the ν^{as}C-P vibration. Again, bands in the νP-O(H) region change, as can be seen at 1076 and 1107 cm^{-1}, indicating an interaction did indeed occur.

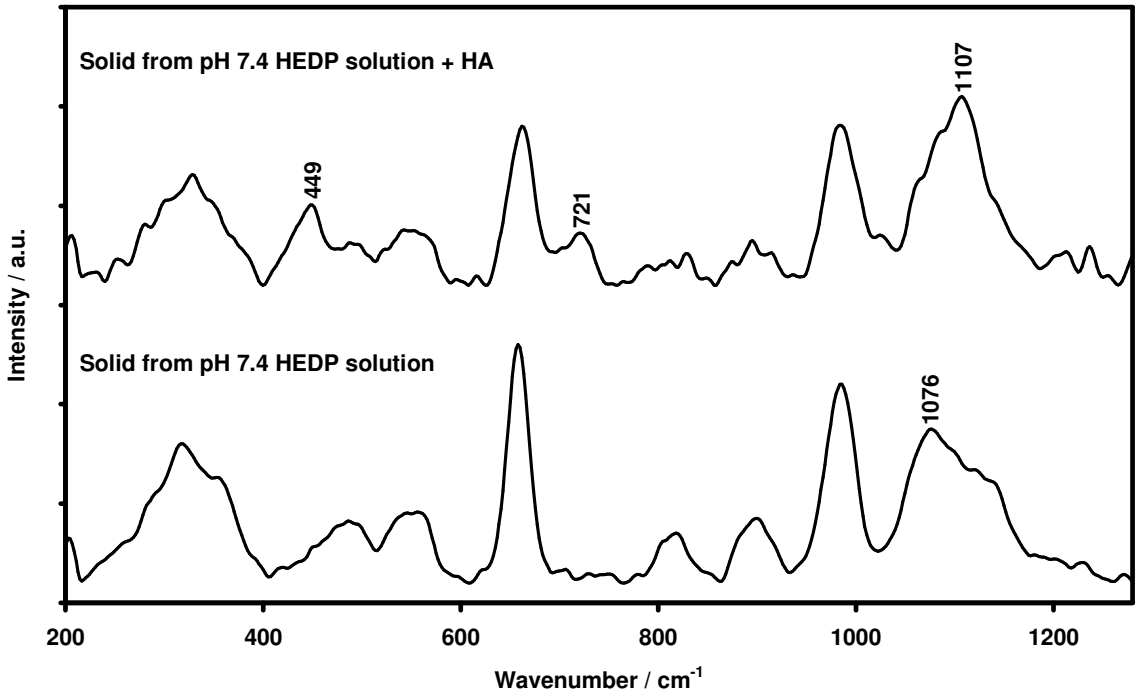

Figure 4-5. Raman spectra of solids obtained from solution before and after HEDP containing solution at pH 7.4 was exposed to HA

In the case of the solution at pH 7.4, the mechanism could not be an acid-leaching process. It is probably chemisorption of the HEDP onto the HA solid [12], and so affects the solution composition as indirectly observed in the Raman spectra of the solids obtained.

4.3 Conclusions

It is very difficult to study the solution/solid interface interaction as can be seen from the work presented in this chapter. This is especially true when trying to directly probe the solid-solution interface interaction directly using Raman spectroscopy. Still, Raman analyses of the solids obtained from the solutions successfully showed that the HEDP(aq) does interact with HA, even at pH 7.4. It would seem that after the HEDP has chemisorbed onto the HA surface at pH 7.4 the calcium is leached into solution and then exists in an equilibrium state between the solid and solution interface. This preliminary work shows that more research is required regarding spectral sampling to more efficiently study these weak interactions by means of Raman spectroscopy.

4.4 References

[1] G. Penel, C. Delfosse, M. Descamps, G. Leroy. *Bone* **2005**, *36*, 893.

[2] J.D. Pasteris, B. Wopenka, J.J. Freeman, K. Rogers, E. Valsami-Jones, J.A.M. Van der Houwen, M.J. Silva. *Biomaterials* **2004**, *25*, 229.

[3] J.H. Lin. *Bone* **1996**, *18*, 75.

[4] L. Van Haverbeke, H.O. Desseyn, M.A. Herman. *B. Soc. Chim. Belg.* **1972**, *81*, 547.

[5] M.V. Mikelsons, T.C. Pinkerton. *Appl. Radiat. Isotopes* **1987**, *38*, 569.

[6] L.A. Myund, E.A. Bus'ko, N.I. Smirnova, S.N. Terekhin, N.M. Dyatlova, K.A. Burkov. *Vestn. Lenin U. Fiz. Kh. Seriya 4* **1987**, *3*, 48.

[7] E.A. Bus'ko, L.A. Myund, S.N. Terekhin, K.A. Burkov, N.M. Dyatlova, N.A. Volkova. *Zh. Neorg. Khim.* **1988**, *33*, 603.

[8] L.A. Myund,E.A. Bus'ko, S.N. Terekhin, K.A. Burkov. *J. Appl. Spectrosc.* **1989**, *50*, 416.

[9] L.A. Myund, E.A. Bus'ko, S.N. Terekhin, K.A. Burkov. *Vestn. Lenin U. Fiz. Kh. Seriya 4* **1990**, *1*, 33.

[10] A.G. Matveeva, M.P. Pasechnik, P.V. Petrovskii, S.V. Matveev, S.A. Pisareva. *Russ. Chem. B* **2000**, *49*, 1045.

[11] J. Robinson, I. Cukrowski, H.M. Marques. *J. Mol. Struct.* **2006**, *825*, 134.

[12] G. H. Nancollas, R. Tang, R.J. Phipps, Z. Henneman, S. Gulde, W. Wu, A. Mangood, R.G.G. Russell, F.H. Ebetino. *Bone*, **2006**, *38*, 617.

[13] L.E. Hein, R.L. Grassi, E.J.A. Roldan, D. Gregori, M.E. Varela, E.P. Piccinni. *Medicina* **1997**, *57 (Supplement 1)*, 10.

[14] A. Aminzadeh. *Spectrochim Acta A* **1997**, *53*, 693.

[15] S.V. Dorozhkin, M. Epple. *Angew. Chem Int. Ed.* **2002**, *41*, 3130.

[16] M. Yoshioka, Y. Yoshida, S. Inoue, P. Lambrechts, G. Vanherle, Y. Nomura, M. Okazaki, H. Shintani, B. Van Meerbeek. *J. Biomed. Mater. Res.* **2002**, *59*, 56.

[17] J.R. Zeevaart, N.V. Jarvis, I. Cukrowski, G.E. Jackson. *S. Afr. J. Chem.* **1997**, *50*, 189.

[18] J.R. Zeevaart. *Metal-ion Speciation in Blood Plasma as a Tool in Predicting the in vivo Behaviour of Potential Bone-seeking Radiopharmaceuticals*, Delft University Press, Delft, **2001**, Chapter 9.

5 Conclusions

5.1 Summary

It has been shown in Chapters 3 and 4 how various techniques can be used to obtain different information regarding the interactions with HEDP in the solid state and in solution. These techniques also made it possible to study the various protonated forms of HEDP in solution, and their conformers and intra/intermolecular interactions in solution. Theoretical methods were used to interpret and rationalise the experimental data obtained. Also, the interaction of HEDP(aq) with hydroxyapatite as a model of bone was investigated, specifically using Raman spectroscopy. The following sections will explicitly state what each technique contributed to the understanding of the HEDP systems studied.

5.2 NMR spectroscopy

NMR spectroscopy can be a useful tool to study a bisphosphonate's structural and deprotonation processes if it is sufficiently soluble in the NMR solvent. ^{1}H and ^{31}P NMR are the more efficient techniques and specifically ^{31}P NMR can be used to estimate roughly the pK_a values for the polyprotic acid, provided the necessary sampling resolution is achieved, as observed in Table 3-3. Also, ^{23}Na showed that Na^+(aq) does not interfere with the various protonated forms of HEDP in solution, and therefore will not affect the data obtained with other techniques, such as solution Raman spectroscopy.

The solution NMR spectra of HEDP and $CaH_2L{\cdot}2H_2O$ are solvent-dependent, and comparison of the NMR spectra obtained in different solvents gives a better understanding of the compound's behaviour in aqueous medium, as evidenced in

Section 3.2.1. From the NMR data it was thus shown that CaH_2L does not dissociate to a large extent in solution.

5.3 X-ray diffraction methods

The determination of the solid-state structure of a compound is always of great assistance in understanding the chemistry of the compound. Determination of structures to obtain the atomic positions of the hydrogen atoms accurately is of the utmost importance in cases where the chemistry of the compound is dominated by hydrogen bond interactions, be it intra- or intermolecularly, as in the case of HEDP and practically all other bisphosphonate derivatives. Accurate determination of the crystal structure also assisted in generating theoretical vibrational spectra with more confidence for comparison with the experimental data, and thus assisted with assignment of the vibrational data.

The solving of crystal structures using powder diffraction methods is a tedious task, but highly favourable when no single crystal is available to solve the structure. The use of Rietveld refinement to solve the crystal structure of anhydrous HEDP acceptably from only a powder pattern, with no prior information regarding its structure, shows the power of the technique as well as the possible pitfalls if erroneous choices are made or if ambiguous choices arise due to inherent faults in the sampling methods. The solution of anhydrous HEDP's powder pattern would have been more difficult if a rigid-body approach had not been employed to obtain sound starting coordinates for the refinement of the independent atoms. This is because there are no heavy atoms present in this structure with which to determine accurately positions of high electron density; heavy atoms would have made the Rietveld refinement easier.

5.4 Vibrational spectroscopy

Section 3.5 shows that the use of vibrational spectroscopy, and specifically Raman spectroscopy, to monitor structural and chemical changes, or any other change that can influence chemical bonding in varied environments, is of great

value. This was well demonstrated in the solid-state Raman spectra of HEDP·H_2O and anhydrous HEDP in which the phase change that occurred in the crystal structure during the loss of hydration was observed with Raman spectroscopy; this was also done using powder X-ray diffraction.

The solution Raman spectra of HEDP allowed the discrete observation of the various protonated forms of HEDP in aqueous medium where NMR could not differentiate between discrete species. There is also strong evidence in the Raman spectra of hydrogen bond interactions in solution and this is supported by the theoretical modelling results of the various protonated conformers of HEDP. The trend of the discretely observed Raman bands was also seen to follow the chemical shift of the ^{31}P NMR signal. The solution Raman spectra of H_2L^{2-}, HL^{3-} and L^{4-} were confidently assigned with the aid of molecular modelling of the solution Raman spectra. H_4L and H_3L^- were problematic due to the strong hydrogen bonding interactions that occurred in solution and because the overlap of these species distribution ranges complicates the system even further.

Raman spectroscopy was also successfully employed to study HEDP(aq) which was found to interact similarly with bovine bone, HA and $CaHPO_4$. Thus HA can be substituted as a model of bone. Two calcium complexes formed on the solid surfaces: one was determined to be $CaH_2L·2H_2O$ and the unknown Ca-HEDP complex is postulated to be $CaHL^-$. This postulation is supported by the solution modelling of Ca-HEDP complexes in Section 3.5.2, as well as by Raman spectroscopic evidence. Also, pH and concentration dependence were observed to form each of these Ca complexes sequentially, which was explained from the modelled solution species distributions of Ca-HEDP complexes. An explanation for why CaH_2L was not determined previously is also given; this is due to the fact that the total proton concentration does not change during the formation of CaH_2L and glass electrode potentiometry would therefore not detect it.

Rigorous assignments of the Raman spectra were made for HEDP, HEDP·H_2O, $CaH_2L·2H_2O$ and the unknown Ca-HEDP complex, aided by empirical literature data and theoretically calculated vibrational spectra. This allowed the various compounds to be compared, the structural and chemical changes occurring at

the molecular level to be ascertained, and determination of which vibrational bands are most affected by these changes and can thus be used to monitor when these changes occur.

A better understanding of which techniques can be applied successfully to investigate HEDP (either solvated or as it interacts/reacts with solid interfaces) will result in a better understanding of these processes in general for other bisphosphonates as well. It was shown, albeit at an initial stage, that two different types of interaction of HEDP could be monitored indirectly in solution in an acidic (leaching) environment and at a pH value that mimics the human physiological pH of 7.4, which is slightly basic.

5.5 Modelling techniques

Molecular modelling was used extensively, either to determine conformeric structures or to aid in the assignment of experimental Raman spectra of compounds in solution or in the solid state, as discussed in the previous chapters.

Probable conformers that are present most of the time in solution for H_3L^-, H_2L^{2-}, HL^{3-} and L^{4-} (all of which have intramolecular hydrogen bonds) were determined and it was shown that H_4L could be present as many conformers, rather than as a single major conformer. Vibrational assignment of H_2L^{2-}, HL^{3-} and L^{4-} was also done using theoretically calculated Raman spectra.

It is also reasoned that in the case of H_2L^{2-}, the predominant conformer for the uncoordinated H_2L^{2-} is different from that preferred for the Ca^{2+} coordinated form. The insolubility of $CaH_2L{\cdot}2H_2O$ unfortunately did not allow experimental verification of these findings postulated from theoretical calculations.

MCR analysis of the solution Raman spectra proved invaluable in determining pure component spectra for all the various protonated forms of HEDP, but specifically for the problematic H_4L and H_3L^- species. In the case of HEDP, care

should be taken during the MCR analysis in implementing the unimodality constraint. Even though it is a valid assumption (and acceptable species distribution curves are obtained), the pure component spectra so obtained do not describe the system satisfactorily. The supposition that the strong hydrogen bonded species at low pH could be observed as a separate species was proved incorrect, but the hydrogen bonding manifests itself as anomalies in the species distribution diagram. The system can therefore be seen to be formally composed of five distinct species over the pH range, with strong hydrogen bonding interactions occurring at low pH values.

5.6 The holistic approach

In summary, each technique brings with it its own unique contribution to a fundamental understanding of the system, but each technique also has its limits. The novel possibility of using Raman spectroscopy to directly study the interaction of HEDP with HA was shown to be possible and in this way detect the formation of compounds at the solid-solution interface that cannot be detected otherwise. It is of course necessary to fully characterise all of these compounds and therefore Raman spectroscopy alone will not suffice. Using various techniques in conjunction with each other or in a supportive role, rather than as single, separate techniques, therefore gives a much better understanding of what happens at the molecular level, and what is observed with Raman spectroscopy.

5.7 Future work

The successful measurement of Raman spectra at low pH as shown in Chapter 4 shows that Raman is a very promising technique to probe interactions directly on a fundamental, molecular level at the solid-solution interface for bisphosphonates and HA. The unsuccessfulness of measuring Raman spectra at the solid-solution interface at pH 5.0 and 7.4 clearly indicates that more work is required to probe the interactions under these different conditions. This could be with reference to choice of instrument, another experimental setup under the laser objective, or an unknown problem not yet identified. Taking into consideration that this was a first

attempt to holistically attempt this, it is clear that the whole is greater than the sum of the parts for research into bisphosphonates, especially when trying to gain a fundamental understanding of what occurs at the solid-solution interface. It is therefore important to first understand these interactions with reference to simpler models (for example substituting HA for bone) before they are implemented or extended to more complex systems for final tailoring and designing of drugs for the treatment of degenerative bone diseases.

APPENDIX

Table A-1.1. Crystal data and structure refinement for HEDP·H_2O.

Identification code	HEDP·H_2O	
Empirical formula	$C_2 H_{10} O_8 P_2$	
Formula weight	224.04	
Temperature	293(2) K	
Wavelength	0.71073 Å	
Crystal system	Monoclinic	
Space group	$P2_1/c$	
Unit cell dimensions	a = 6.9878(7) Å	a = 90º
	b = 17.5810(18) Å	b = 108.451(2)º
	c = 7.1140(8) Å	g = 90º
Volume	829.05(15) $Å^3$	
Z	4	
Density (calculated)	1.795 Mg/m^3	
Absorption coefficient	0.535 mm^{-1}	
F(000)	464	
Crystal size	0.68 x 0.32 x 0.30 mm^3	
Theta range for data collection	3.07 to 26.60º.	
Index ranges	-7<=h<=8, -21<=k<=8, -8<=l<=8	
Reflections collected	4 313	
Independent reflections	1 571 [R(int) = 0.0292]	
Completeness to theta = 25.00º	99.4 %	
Absorption correction	Semi-empirical from equivalents	
Max. and min. transmission	0.852 and 0.746	
Refinement method	Full-matrix least-squares on F^2	
Data / restraints / parameters	1571 / 0 / 150	
Goodness-of-fit on F^2	1.094	
Final R indices [I>2sigma(I)]	R1 = 0.0317, wR2 = 0.0844	
R indices (all data)	R1 = 0.0319, wR2 = 0.0846	
Extinction coefficient	0.015(3)	
Largest diff. peak and hole	0.422 and -0.389 e.$Å^{-3}$	

Table A-1.2. Atomic coordinates (x 10^4) and equivalent isotropic displacement parameters (Å^{2}x 10^3) for HEDP·H_2O. U(eq) is defined as one-third of the trace of the orthogonalised U^{ij} tensor

	x	y	z	U(eq)
P(1)	1978(1)	5911(1)	5422(1)	21(1)
P(2)	3784(1)	6334(1)	2130(1)	22(1)
O(1)	2564(2)	5093(1)	5381(2)	28(1)
O(2)	-11(2)	6021(1)	5933(2)	31(1)
O(3)	3580(2)	6406(1)	6881(2)	29(1)
O(4)	4302(3)	5491(1)	1918(2)	34(1)
O(5)	3244(2)	6724(1)	163(2)	29(1)
O(6)	5505(2)	6730(1)	3730(2)	31(1)
O(7)	996(2)	7129(1)	3063(2)	27(1)
O(8)	7375(3)	7743(1)	2758(3)	36(1)
C(1)	1572(3)	6349(1)	2991(3)	21(1)
C(2)	-187(3)	5943(1)	1466(3)	30(1)

Table A-1.3. Bond lengths [Å] and angles [º] for HEDP·H_2O

LENGTHS:			
P(1)-O(1)	1.4980(13)	O(5)-P(2)-O(6)	113.12(8)
P(1)-O(3)	1.5337(14)	O(5)-P(2)-O(4)	110.22(8)
P(1)-O(2)	1.5559(14)	O(6)-P(2)-O(4)	110.73(9)
P(1)-C(1)	1.8309(18)	O(5)-P(2)-C(1)	108.47(8)
P(2)-O(5)	1.4952(13)	O(6)-P(2)-C(1)	106.92(8)
P(2)-O(6)	1.5361(14)	O(4)-P(2)-C(1)	107.12(8)
P(2)-O(4)	1.5445(15)	P(1)-O(2)-H(2)	112(2)
P(2)-C(1)	1.8342(19)	P(1)-O(3)-H(3)	113(3)
O(2)-H(2)	0.77(3)	P(2)-O(4)-H(4)	113(3)
O(3)-H(3)	0.77(4)	P(2)-O(6)-H(6)	115(2)
O(4)-H(4)	0.73(4)	C(1)-O(7)-H(7)	115.9(19)
O(6)-H(6)	1.04(4)	H(6)-O(8)-H(8A)	111(3)
O(7)-C(1)	1.435(2)	H(6)-O(8)-H(8B)	107(3)
O(7)-H(7)	0.79(3)	H(8A)-O(8)-H(8B)	113(3)
O(8)-H(6)	1.40(4)	O(7)-C(1)-C(2)	107.36(14)
O(8)-H(8A)	0.76(3)	O(7)-C(1)-P(1)	109.25(12)
O(8)-H(8B)	0.73(4)	C(2)-C(1)-P(1)	108.83(13)
C(1)-C(2)	1.534(2)	O(7)-C(1)-P(2)	107.47(11)
C(2)-H(2A)	0.98(3)	C(2)-C(1)-P(2)	109.19(13)
C(2)-H(2B)	1.01(3)	P(1)-C(1)-P(2)	114.50(9)
C(2)-H(2C)	0.93(3)	C(1)-C(2)-H(2A)	110.7(15)
		C(1)-C(2)-H(2B)	109.5(16)
ANGLES:		H(2A)-C(2)-H(2B)	108(2)
O(1)-P(1)-O(3)	114.35(8)	C(1)-C(2)-H(2C)	108.3(17)
O(1)-P(1)-O(2)	113.19(8)	H(2A)-C(2)-H(2C)	105(2)
O(3)-P(1)-O(2)	106.60(8)	H(2B)-C(2)-H(2C)	115(2)
O(1)-P(1)-C(1)	110.29(8)		
O(3)-P(1)-C(1)	105.21(8)		
O(2)-P(1)-C(1)	106.61(8)		

Table A-1.4. Anisotropic displacement parameters ($Å^2 x\ 10^3$)for $HEDP{\cdot}H_2O$. The anisotropic displacement factor exponent takes the form: $-2p^2[\ h^2a^{*2}U^{11} + ... + 2\ h\ k\ a^*\ b^*\ U^{12}]$

	U^{11}	U^{22}	U^{33}	U^{23}	U^{13}	U^{12}
P(1)	22(1)	21(1)	21(1)	0(1)	7(1)	-2(1)
P(2)	24(1)	24(1)	18(1)	1(1)	7(1)	3(1)
O(1)	28(1)	23(1)	33(1)	4(1)	7(1)	1(1)
O(2)	28(1)	31(1)	39(1)	-7(1)	17(1)	-5(1)
O(3)	30(1)	38(1)	22(1)	-6(1)	10(1)	-10(1)
O(4)	39(1)	30(1)	33(1)	-1(1)	9(1)	12(1)
O(5)	38(1)	30(1)	21(1)	3(1)	10(1)	5(1)
O(6)	26(1)	43(1)	24(1)	-1(1)	6(1)	-6(1)
O(7)	24(1)	20(1)	33(1)	-2(1)	5(1)	2(1)
O(8)	25(1)	39(1)	43(1)	5(1)	9(1)	1(1)
C(1)	22(1)	18(1)	21(1)	0(1)	5(1)	2(1)
C(2)	28(1)	30(1)	27(1)	-3(1)	0(1)	-4(1)

Table A-1.5. Hydrogen coordinates (x 10^4) and isotropic displacement parameters (Å^{2}x 10^3) for HEDP·H_2O

	x	y	z	U(eq)
H(2)	-740(50)	5683(18)	5580(50)	56(9)
H(2A)	-430(40)	6162(14)	150(40)	42(7)
H(2B)	-1460(40)	6008(15)	1840(40)	50(7)
H(2C)	190(40)	5440(16)	1360(40)	48(7)
H(3)	3390(60)	6450(20)	7880(60)	80(12)
H(4)	5120(60)	5350(20)	2760(50)	67(11)
H(6)	6230(60)	7160(20)	3210(50)	93(12)
H(7)	1780(40)	7388(15)	3830(40)	39(7)
H(8A)	8350(50)	7586(15)	2650(40)	42(8)
H(8B)	6730(50)	7930(20)	1860(50)	63(10)

Table A-1.6. Torsion angles [º] for HEDP·H_2O

O(1)-P(1)-C(1)-O(7)	179.52(11)
O(3)-P(1)-C(1)-O(7)	-56.70(13)
O(2)-P(1)-C(1)-O(7)	56.26(13)
O(1)-P(1)-C(1)-C(2)	62.57(14)
O(3)-P(1)-C(1)-C(2)	-173.64(13)
O(2)-P(1)-C(1)-C(2)	-60.68(14)
O(1)-P(1)-C(1)-P(2)	-59.91(11)
O(3)-P(1)-C(1)-P(2)	63.88(11)
O(2)-P(1)-C(1)-P(2)	176.84(9)
O(5)-P(2)-C(1)-O(7)	-57.17(13)
O(6)-P(2)-C(1)-O(7)	65.12(13)
O(4)-P(2)-C(1)-O(7)	-176.13(11)
O(5)-P(2)-C(1)-C(2)	58.98(14)
O(6)-P(2)-C(1)-C(2)	-178.72(12)
O(4)-P(2)-C(1)-C(2)	-59.98(14)
O(5)-P(2)-C(1)-P(1)	-178.73(8)
O(6)-P(2)-C(1)-P(1)	-56.43(11)
O(4)-P(2)-C(1)-P(1)	62.31(12)

Table A-1.7. Hydrogen bonds for HEDP·H_2O [Å and º]

D-H...A	d(D-H)	d(H...A)	d(D...A)	<(DHA)
O(2)-H(2)...O(1)#1	0.77(3)	1.84(3)	2.615(2)	177(3)
O(3)-H(3)...O(5)#2	0.77(4)	1.72(4)	2.4832(19)	169(4)
O(4)-H(4)...O(1)#3	0.73(4)	1.90(4)	2.623(2)	170(4)
O(6)-H(6)...O(8)	1.04(4)	1.40(4)	2.435(2)	173(3)
O(7)-H(7)...O(5)#4	0.79(3)	1.94(3)	2.699(2)	162(3)
O(8)-H(8A)...O(7)#5	0.76(3)	1.95(3)	2.696(2)	166(3)
O(8)-H(8B)...O(6)#6	0.73(4)	2.20(4)	2.899(2)	160(3)

Symmetry transformations used to generate equivalent atoms:

#1 -x,-y+1,-z+1 #2 x,y,z+1 #3 -x+1,-y+1,-z+1

#4 x,-y+3/2,z+1/2 #5 x+1,y,z #6 x,-y+3/2,z-1/2

Table A-2.1. Crystal data and structure refinement for $CaHEDP{\cdot}2H_2O$

Identification code	$CaHEDP{\cdot}2H_2O$	
Empirical formula	$C_2\ H_{10}\ Ca\ O_9\ P_2$	
Formula weight	280.12	
Temperature	293(2) K	
Wavelength	0.71073 Å	
Crystal system	Triclinic	
Space group	P$\bar{1}$	
Unit cell dimensions	a = 6.9499(6) Å	a = 92.7330(10)º
	b = 7.5961(6) Å	b = 106.3140(10)º
	c = 9.7000(8) Å	g = 112.4250(10)º
Volume	447.33(6) $Å^3$	
Z	2	
Density (calculated)	2.080 Mg/m^3	
Absorption coefficient	1.087 mm^{-1}	
F(000)	288	
Crystal size	0.30 x 0.22 x 0.18 mm^3	
Theta range for data collection	2.95 to 26.41º.	
Index ranges	-5<=h<=8, -9<=k<=4, -11<=l<=10	
Reflections collected	2 442	
Independent reflections	1622 [R(int) = 0.0200]	
Completeness to theta = 25.00º	97.7 %	
Absorption correction	Semi-empirical from equivalents	
Max. and min. transmission	0.822 and 0.707	
Refinement method	Full-matrix least-squares on F^2	
Data / restraints / parameters	1622 / 0 / 163	
Goodness-of-fit on F^2	1.115	
Final R indices [I>2sigma(I)]	R1 = 0.0339, wR2 = 0.0942	
R indices (all data)	R1 = 0.0344, wR2 = 0.0947	
Extinction coefficient	0	
Largest diff. peak and hole	0.841 and -0.537 e.$Å^{-3}$	

Table A-2.2. Atomic coordinates (x 10^4) and equivalent isotropic displacement parameters (Å^{2}x 10^3) for CaHEDP·2H_2O. U(eq) is defined as one-third of the trace of the orthogonalised U^{ij} tensor

	x	y	z	U(eq)
Ca(1)	4077(1)	7051(1)	-147(1)	14(1)
P(1)	-166(1)	7575(1)	1252(1)	13(1)
O(1)	1074(3)	7498(3)	230(2)	19(1)
O(2)	-2637(3)	6484(2)	654(2)	17(1)
O(3)	335(3)	9740(3)	1828(2)	20(1)
P(2)	3609(1)	7030(1)	3444(1)	16(1)
O(4)	4035(3)	6130(2)	2211(2)	18(1)
O(5)	4829(3)	9255(2)	3765(2)	21(1)
O(6)	4106(3)	6190(3)	4844(2)	22(1)
C(1)	677(4)	6522(3)	2864(3)	16(1)
C(2)	-40(5)	7133(4)	4086(3)	21(1)
O(7)	-531(3)	4433(2)	2392(2)	20(1)
O(8)	3569(4)	9773(3)	-1459(2)	19(1)
O(9)	5753(3)	7331(3)	-2133(2)	20(1)

Table A-2.3. Bond lengths [Å] and angles [º] for CaHEDP·2H_2O

LENGTHS:

Ca(1)-O(1)	2.3580(17)	O(7)-Ca(1)#2	2.5919(18)
Ca(1)-O(2)#1	2.4064(16)	O(7)-H(7)	0.82(4)
Ca(1)-O(4)	2.4277(18)	O(8)-Ca(1)#3	2.4743(19)
Ca(1)-O(2)#2	2.4498(17)	O(8)-H(8A)	0.66(4)
Ca(1)-O(8)#3	2.4743(19)	O(8)-H(8B)	0.72(4)
Ca(1)-O(9)	2.4956(19)	O(9)-H(9A)	0.82(4)
Ca(1)-O(8)	2.564(2)	O(9)-H(9B)	0.73(4)
Ca(1)-O(7)#2	2.5919(18)		
Ca(1)-P(1)#2	3.4061(7)	ANGLES:	
Ca(1)-Ca(1)#4	3.7906(9)	O(1)-Ca(1)-O(2)#1	152.91(6)
Ca(1)-Ca(1)#3	4.1334(9)	O(1)-Ca(1)-O(4)	75.61(6)
Ca(1)-H(9A)	2.70(4)	O(2)#1-Ca(1)-O(4)	77.87(6)
P(1)-O(1)	1.4974(17)	O(1)-Ca(1)-O(2)#2	101.40(6)
P(1)-O(2)	1.5103(17)	O(2)#1-Ca(1)-O(2)#2	77.38(6)
P(1)-O(3)	1.5828(18)	O(4)-Ca(1)-O(2)#2	76.37(6)
P(1)-C(1)	1.842(2)	O(1)-Ca(1)-O(8)#3	86.48(7)
P(1)-Ca(1)#2	3.4061(7)	O(2)#1-Ca(1)-O(8)#3	83.63(6)
O(2)-Ca(1)#5	2.4064(16)	O(4)-Ca(1)-O(8)#3	80.04(7)
O(2)-Ca(1)#2	2.4498(17)	O(2)#2-Ca(1)-O(8)#3	152.27(6)
O(3)-H(3)	0.79(4)	O(1)-Ca(1)-O(9)	136.47(7)
P(2)-O(4)	1.5042(17)	O(2)#1-Ca(1)-O(9)	70.40(7)
P(2)-O(6)	1.5353(18)	O(4)-Ca(1)-O(9)	147.81(7)
P(2)-O(5)	1.5432(18)	O(2)#2-Ca(1)-O(9)	91.28(6)
P(2)-C(1)	1.831(2)	O(8)#3-Ca(1)-O(9)	101.24(7)
O(6)-H(6)	0.8200	O(1)-Ca(1)-O(8)	71.29(7)
C(1)-O(7)	1.460(3)	O(2)#1-Ca(1)-O(8)	127.47(7)
C(1)-C(2)	1.524(3)	O(4)-Ca(1)-O(8)	135.91(7)
C(2)-H(2A)	0.92(4)	O(2)#2-Ca(1)-O(8)	137.96(6)
C(2)-H(2B)	0.93(4)	O(8)#3-Ca(1)-O(8)	69.77(8)
C(2)-H(2C)	0.89(4)	O(9)-Ca(1)-O(8)	71.60(7)

O(1)-Ca(1)-O(7)#2 66.70(6)
O(2)#1-Ca(1)-O(7)#2 133.89(6)
O(4)-Ca(1)-O(7)#2 120.31(6)
O(2)#2-Ca(1)-O(7)#2 68.27(6)
O(8)#3-Ca(1)-O(7)#2 137.91(6)
O(9)-Ca(1)-O(7)#2 80.35(7)
O(8)-Ca(1)-O(7)#2 71.09(6)
O(1)-Ca(1)-P(1)#2 80.17(5)
O(2)#1-Ca(1)-P(1)#2 100.70(4)
O(4)-Ca(1)-P(1)#2 80.21(4)
O(2)#2-Ca(1)-P(1)#2 23.35(4)
O(8)#3-Ca(1)-P(1)#2 158.38(6)
O(9)-Ca(1)-P(1)#2 100.15(5)
O(8)-Ca(1)-P(1)#2 120.68(5)
O(7)#2-Ca(1)-P(1)#2 49.84(4)
O(1)-Ca(1)-Ca(1)#4 133.87(5)
O(2)#1-Ca(1)-Ca(1)#4 39.10(4)
O(4)-Ca(1)-Ca(1)#4 73.40(4)
O(2)#2-Ca(1)-Ca(1)#4 38.28(4)
O(8)#3-Ca(1)-Ca(1)#4 120.10(5)
O(9)-Ca(1)-Ca(1)#4 78.55(5)
O(8)-Ca(1)-Ca(1)#4 150.02(6)
O(7)#2-Ca(1)-Ca(1)#4 101.59(4)
P(1)#2-Ca(1)-Ca(1)#4 61.608(16)
O(1)-Ca(1)-Ca(1)#3 76.36(5)
O(2)#1-Ca(1)-Ca(1)#3 108.11(4)
O(4)-Ca(1)-Ca(1)#3 110.00(4)
O(2)#2-Ca(1)-Ca(1)#3 172.13(5)
O(8)#3-Ca(1)-Ca(1)#3 35.60(5)
O(9)-Ca(1)-Ca(1)#3 85.46(5)
O(8)-Ca(1)-Ca(1)#3 34.17(4)
O(7)#2-Ca(1)-Ca(1)#3 104.07(4)
P(1)#2-Ca(1)-Ca(1)#3 150.81(2)
Ca(1)#4-Ca(1)-Ca(1)#3 146.88(2)
O(1)-Ca(1)-H(9A) 148.2(9)
O(2)#1-Ca(1)-H(9A) 58.5(9)
O(4)-Ca(1)-H(9A) 132.4(9)
O(2)#2-Ca(1)-H(9A) 76.5(9)
O(8)#3-Ca(1)-H(9A) 110.3(8)
O(9)-Ca(1)-H(9A) 17.5(9)
O(8)-Ca(1)-H(9A) 88.9(9)
O(7)#2-Ca(1)-H(9A) 83.7(8)
P(1)#2-Ca(1)-H(9A) 89.6(8)
Ca(1)#4-Ca(1)-H(9A) 61.1(9)
Ca(1)#3-Ca(1)-H(9A) 101.3(9)
O(1)-P(1)-O(2) 116.26(10)
O(1)-P(1)-O(3) 110.84(11)
O(2)-P(1)-O(3) 107.13(10)
O(1)-P(1)-C(1) 110.61(10)
O(2)-P(1)-C(1) 104.59(10)
O(3)-P(1)-C(1) 106.85(10)
O(1)-P(1)-Ca(1)#2 97.26(7)
O(2)-P(1)-Ca(1)#2 40.00(6)
O(3)-P(1)-Ca(1)#2 145.53(7)
C(1)-P(1)-Ca(1)#2 80.00(8)
P(1)-O(1)-Ca(1) 147.91(10)
P(1)-O(2)-Ca(1)#5 140.64(10)
P(1)-O(2)-Ca(1)#2 116.65(9)
Ca(1)#5-O(2)-Ca(1)#2 102.62(6)
P(1)-O(3)-H(3) 113(3)
O(4)-P(2)-O(6) 113.28(10)
O(4)-P(2)-O(5) 112.30(10)
O(6)-P(2)-O(5) 110.56(10)
O(4)-P(2)-C(1) 107.60(11)
O(6)-P(2)-C(1) 107.14(11)
O(5)-P(2)-C(1) 105.47(10)
P(2)-O(4)-Ca(1) 130.26(10)
P(2)-O(6)-H(6) 109.5

O(7)-C(1)-C(2)	108.30(19)	C(1)-O(7)-Ca(1)#2	121.59(14)
O(7)-C(1)-P(2)	106.92(16)	C(1)-O(7)-H(7)	110(2)
C(2)-C(1)-P(2)	113.00(17)	Ca(1)#2-O(7)-H(7)	92(2)
O(7)-C(1)-P(1)	105.19(15)	Ca(1)#3-O(8)-Ca(1)	110.23(8)
C(2)-C(1)-P(1)	110.16(17)	Ca(1)#3-O(8)-H(8A)	104(3)
P(2)-C(1)-P(1)	112.81(12)	Ca(1)-O(8)-H(8A)	121(3)
C(1)-C(2)-H(2A)	108(2)	Ca(1)#3-O(8)-H(8B)	104(3)
C(1)-C(2)-H(2B)	111(2)	Ca(1)-O(8)-H(8B)	110(3)
H(2A)-C(2)-H(2B)	107(3)	H(8A)-O(8)-H(8B)	105(4)
C(1)-C(2)-H(2C)	111(2)	Ca(1)-O(9)-H(9A)	96(3)
H(2A)-C(2)-H(2C)	109(3)	Ca(1)-O(9)-H(9B)	116(3)
H(2B)-C(2)-H(2C)	111(3)	H(9A)-O(9)-H(9B)	105(4)

Symmetry transformations used to generate equivalent atoms:

#1 x+1,y,z #2 -x,-y+1,-z #3 -x+1,-y+2,-z #4 -x+1,-y+1,-z #5 x-1,y,z

Table A-2.4. Anisotropic displacement parameters ($Å^2 x\ 10^3$)for $CaHEDP{\cdot}2H_2O$. The anisotropic displacement factor exponent takes the form: $-2p^2[\ h^2a^{*2}U^{11} + ... + 2\ h\ k\ a^*\ b^*\ U^{12}]$

	U^{11}	U^{22}	U^{33}	U^{23}	U^{13}	U^{12}
Ca(1)	14(1)	14(1)	16(1)	2(1)	6(1)	6(1)
P(1)	11(1)	14(1)	14(1)	3(1)	5(1)	6(1)
O(1)	18(1)	26(1)	19(1)	7(1)	9(1)	12(1)
O(2)	12(1)	18(1)	19(1)	2(1)	4(1)	5(1)
O(3)	17(1)	14(1)	29(1)	2(1)	8(1)	6(1)
P(2)	14(1)	18(1)	15(1)	1(1)	4(1)	7(1)
O(4)	20(1)	19(1)	17(1)	3(1)	6(1)	12(1)
O(5)	22(1)	18(1)	20(1)	1(1)	8(1)	5(1)
O(6)	29(1)	29(1)	18(1)	7(1)	9(1)	19(1)
C(1)	16(1)	15(1)	17(1)	3(1)	6(1)	5(1)
C(2)	23(1)	27(1)	19(1)	5(1)	11(1)	13(1)
O(7)	19(1)	14(1)	24(1)	2(1)	6(1)	4(1)
O(8)	18(1)	19(1)	22(1)	5(1)	9(1)	8(1)
O(9)	24(1)	18(1)	18(1)	2(1)	5(1)	11(1)

Table A-2.5. Hydrogen coordinates (x 10^4) and isotropic displacement parameters (Å^{2}x 10^3) for CaHEDP·2H_2O

	x	y	z	U(eq)
H(3)	1490(70)	10490(60)	1840(40)	39(10)
H(6)	4677	5449	4739	34
H(2A)	690(60)	8450(60)	4350(40)	37(9)
H(2B)	-1540(60)	6860(50)	3760(40)	30(8)
H(2C)	300(60)	6580(50)	4850(40)	34(9)
H(7)	140(60)	4000(50)	2000(40)	24(8)
H(8A)	3760(60)	9890(60)	-2090(50)	33(12)
H(8B)	2470(70)	9700(50)	-1590(40)	33(11)
H(9A)	6010(60)	6370(60)	-2050(40)	40(10)
H(9B)	5000(60)	7130(50)	-2880(50)	31(10)

Table A-2.6. Torsion angles [º] for CaHEDP·2H_2O

O(2)-P(1)-O(1)-Ca(1)	-133.98(19)
O(3)-P(1)-O(1)-Ca(1)	103.4(2)
C(1)-P(1)-O(1)-Ca(1)	-14.9(2)
Ca(1)#2-P(1)-O(1)-Ca(1)	-96.94(19)
O(2)#1-Ca(1)-O(1)-P(1)	-2.3(3)
O(4)-Ca(1)-O(1)-P(1)	9.68(19)
O(2)#2-Ca(1)-O(1)-P(1)	82.2(2)
O(8)#3-Ca(1)-O(1)-P(1)	-70.9(2)
O(9)-Ca(1)-O(1)-P(1)	-173.57(17)
O(8)-Ca(1)-O(1)-P(1)	-140.7(2)
O(7)#2-Ca(1)-O(1)-P(1)	142.4(2)
P(1)#2-Ca(1)-O(1)-P(1)	92.0(2)
Ca(1)#4-Ca(1)-O(1)-P(1)	58.7(2)
Ca(1)#3-Ca(1)-O(1)-P(1)	-105.5(2)
O(1)-P(1)-O(2)-Ca(1)#5	-107.44(16)
O(3)-P(1)-O(2)-Ca(1)#5	17.11(18)
C(1)-P(1)-O(2)-Ca(1)#5	130.29(15)
Ca(1)#2-P(1)-O(2)-Ca(1)#5	-175.8(2)
O(1)-P(1)-O(2)-Ca(1)#2	68.36(13)
O(3)-P(1)-O(2)-Ca(1)#2	-167.09(10)
C(1)-P(1)-O(2)-Ca(1)#2	-53.91(12)
O(6)-P(2)-O(4)-Ca(1)	-170.67(11)
O(5)-P(2)-O(4)-Ca(1)	-44.54(16)
C(1)-P(2)-O(4)-Ca(1)	71.09(15)
O(1)-Ca(1)-O(4)-P(2)	-40.26(12)
O(2)#1-Ca(1)-O(4)-P(2)	134.19(14)
O(2)#2-Ca(1)-O(4)-P(2)	-146.06(14)
O(8)#3-Ca(1)-O(4)-P(2)	48.63(13)
O(9)-Ca(1)-O(4)-P(2)	143.94(12)
O(8)-Ca(1)-O(4)-P(2)	1.94(18)
O(7)#2-Ca(1)-O(4)-P(2)	-91.72(14)

P(1)#2-Ca(1)-O(4)-P(2)	-122.53(13)
Ca(1)#4-Ca(1)-O(4)-P(2)	174.35(14)
Ca(1)#3-Ca(1)-O(4)-P(2)	29.11(14)
O(4)-P(2)-C(1)-O(7)	53.61(17)
O(6)-P(2)-C(1)-O(7)	-68.52(17)
O(5)-P(2)-C(1)-O(7)	173.67(14)
O(4)-P(2)-C(1)-C(2)	172.67(17)
O(6)-P(2)-C(1)-C(2)	50.5(2)
O(5)-P(2)-C(1)-C(2)	-67.27(19)
O(4)-P(2)-C(1)-P(1)	-61.54(15)
O(6)-P(2)-C(1)-P(1)	176.33(11)
O(5)-P(2)-C(1)-P(1)	58.51(14)
O(1)-P(1)-C(1)-O(7)	-80.41(17)
O(2)-P(1)-C(1)-O(7)	45.48(17)
O(3)-P(1)-C(1)-O(7)	158.86(15)
Ca(1)#2-P(1)-C(1)-O(7)	13.65(13)
O(1)-P(1)-C(1)-C(2)	163.08(17)
O(2)-P(1)-C(1)-C(2)	-71.03(18)
O(3)-P(1)-C(1)-C(2)	42.3(2)
Ca(1)#2-P(1)-C(1)-C(2)	-102.86(17)
O(1)-P(1)-C(1)-P(2)	35.78(16)
O(2)-P(1)-C(1)-P(2)	161.67(12)
O(3)-P(1)-C(1)-P(2)	-84.95(14)
Ca(1)#2-P(1)-C(1)-P(2)	129.84(12)
C(2)-C(1)-O(7)-Ca(1)#2	96.8(2)
P(2)-C(1)-O(7)-Ca(1)#2	-141.17(11)
P(1)-C(1)-O(7)-Ca(1)#2	-21.0(2)
O(1)-Ca(1)-O(8)-Ca(1)#3	93.19(10)
O(2)#1-Ca(1)-O(8)-Ca(1)#3	-64.44(12)
O(4)-Ca(1)-O(8)-Ca(1)#3	49.80(14)
O(2)#2-Ca(1)-O(8)-Ca(1)#3	179.53(7)
O(8)#3-Ca(1)-O(8)-Ca(1)#3	0.0
O(9)-Ca(1)-O(8)-Ca(1)#3	-109.98(10)
O(7)#2-Ca(1)-O(8)-Ca(1)#3	164.20(11)

P(1)#2-Ca(1)-O(8)-Ca(1)#3 158.96(6)

Ca(1)#4-Ca(1)-O(8)-Ca(1)#3 -115.52(9)

Symmetry transformations used to generate equivalent atoms:

#1 x+1,y,z #2 -x,-y+1,-z #3 -x+1,-y+2,-z

#4 -x+1,-y+1,-z #5 x-1,y,z

Table A-2.7. Hydrogen bonds for CaHEDP·2H_2O [Å and º]

D-H...A	d(D-H)	d(H...A)	d(D...A)	<(DHA)
O(3)-H(3)...O(9)#3	0.79(4)	1.93(4)	2.702(3)	168(4)
O(6)-H(6)...O(6)#6	0.82	1.76	2.542(3)	159.4
O(7)-H(7)...O(1)#2	0.82(4)	2.17(3)	2.728(3)	126(3)
O(7)-H(7)...O(4)	0.82(4)	2.51(3)	2.996(3)	119(3)
O(8)-H(8A)...O(5)#3	0.66(4)	2.13(5)	2.778(3)	166(4)
O(8)-H(8B)...O(3)#7	0.72(4)	2.10(5)	2.803(3)	165(4)
O(9)-H(9A)...O(4)#4	0.82(4)	1.89(4)	2.687(3)	166(4)
O(9)-H(9B)...O(6)#8	0.73(4)	2.13(4)	2.788(3)	151(4)

Symmetry transformations used to generate equivalent atoms:

#1 x+1,y,z #2 -x,-y+1,-z #3 -x+1,-y+2,-z

#4 -x+1,-y+1,-z #5 x-1,y,z #6 -x+1,-y+1,-z+1

#7 -x,-y+2,-z #8 x,y,z-1